Applications of Non-periodic Metasurface for Magnetic Resonance Imaging.

The University Of Sheffield.

Tingzhao Yang

Department of Electronic and Electrical Engineering

The University of Sheffield

This dissertation is submitted for the degrees of

Doctor of Philosophy

June 2020

Acknowledgement

I would like to acknowledge my supervisor Prof. Kenneth Lee Ford for his responsible supervision and clear guidance during my PhD research. Many thanks for his kind encouragement and useful suggestions when I met difficulties.

I would like to appreciate my college Ismail Masoud Issa for his tremendous assistance and help at the beginning of this project.

I would like to express my gratitude to Prof. James Wild, Dr. Madhwesha Rao and Dr. Adam Maunder for their great support to the tests in the MRI scanner. Their detailed responses in the MRI area help me a lot in the development of this project.

Last but not the least, my gratitude also extends to my family and friends who have been supporting and encouraging me all the time.

Publication

T. Yang, K. L. Ford, M. Rao, and J. Wild, "A Single Unit Cell Metasurface for Magnetic Resonance Imaging Applications," *2018 12th Int. Congr. Artif. Mater. Nov. Wave Phenomena, METAMATERIALS 2018,* pp. 131–133, 2018, doi: 10.1109/MetaMaterials.2018.8534181. (Chapter 3)

T. Yang, K. L. Ford, M. Rao, and J. Wild, "A Metasurface for Multi-Nuclear Magnetic Resonance Imaging Applications at 1.5T," in *13th European Conference on Antennas and Propagation, EuCAP 2019*, 2019. (Chapter 4)

Abstract

Within the innovation of MRI systems, high image quality and less imaging time become the major researching target. Metamaterials have shown a big potential to provide new method to improve the transceiver performance of the MRI system, without changing radio frequency (RF) coil structure or increasing the static field strength of the system. However, most of these designs are based on periodic structures, which will have extra power losses caused by extra lumped elements, effects to the homogeneity due to the surface currents between each unit cell, or increment in E-field which is proportional to the specific absorption rate (SAR) as the metamaterial focus the field. This thesis proposed a metasurface with a non-periodic structure to enhance the magnetic flux density B_1^+ and signal to noise ratio (SNR) for 1.5T MRI system, when it was placed between the RF coil and the dielectric phantom. In order to obtain the best design, numerical simulations were tested in CST studio. S-parameter, magnetic field, magnetic flux density and E-field were calculated to define the benefits from the metasurface. During the simulation, it was found that the field of MRI transceiver system was improved, due to the metasurface worked as a second source instead of focusing the field. As a result, E-field was not increased obviously compared with RF coil only case. Then, the optimal design was manufactured by PCB etching technique and tested in 1.5T MRI scanner. From the SNR results obtained from the scanner, the SNR on the phantom surface was improved by 133%, and the enhancement covered the whole penetration depth. Compared with previous researches of the field of view, this non-periodic metasurface has much smaller and flexible dimension. From the SNR results in 2D, the SNR was decayed uniformly inside the dielectric phantom, because the metasurface is non-periodic. This will further increase the sensitivity of RF coil. During the measurement, it was found the non-periodic metasurface could provide an extra frequency band, by the coupling between the metasurface and RF coil. Therefore, the dual-band property of the metasurface was investigated to achieve the multi-nuclei image. After simulation and measurement, a new metasurface in non-periodic structure was proposed to provide two resonances at 60.08MHz and 63.85MHz

for the 19F nuclei and 1H nuclei imaging in 1.5T MRI system. From the SNR results obtained from 1.5T MRI scanner, the SNR was enhanced by 37.9% at 60.08MHz and 32.7% at 63MHz, when comparing with RF coil only case. From the methods people used to achieve multi-nuclei imaging, there is no research could image two frequency bands without reducing the RF performance of the transceiver system. Furthermore, this is the first time to achieve multi-nuclei imaging by using non-periodic metamaterial. Its flexible and simple structure open a new and advanced researching area.

Abbreviations

AMC	Artificial magnetic conductor
CLRs	Capacitively loaded rings
DNG	Double negative material
EBG	Electromagnetic band gap
FID	Free induction decay
FOV	Field of view
FSS	Frequency selective surface
HDC	High dielectric constant
HIS	High impedance surface
LHM	Left hand material
MI	Magneto inductive
MRI	Magnetic resonance image
NMR	Nuclear magnetic resonance
PEC	Perfect electrical conductor
PMC	Perfect magnetic conductor

RF	Radio frequency
RCS	Radar cross section
SAR	Specific absorption rate
SNR	Signal to noise ratio
SRRs	Split-rings resonator
ROI	Region of interest
VNA	Vector Network Analyzer

List of symbols

ϕ	Magnetic momentum
$\wp$	Angular momentum
γ	Gyromagnetic ratio
^{1}H	Hydrogen nucleus
^{19}F	Fluorine nucleus
H_0	Static magnetic field
H_1	External magnetic field
B_0	Static magnetic flux density
B_1	External magnetic flux density
B_1^+	Radio frequency magnetic flux density positively rotated
B_1^-	Radio frequency magnetic flux density negatively rotated
M	Magnetization
M_0	Net magnetization
ω	Angular frequency
ω_0	Larmor angular frequency
I_C	Spin quantum number
U	Number of nuclei
τ	Time constant
k	Boltzmann constant
ρ	Proton density
α	Flip angle
α_g	global Flip angle
T1	Spin- lattice relaxation time
T2	Spin-spin relaxation time
G	Gradient function amplitude
G_{SS}	Gradient amplitude of slice selection function

G_P	Gradient amplitude of phase encoding
G_f	Gradient amplitude of frequency encoding
μ	Relative permeability
μ_0	Free space medium permeability
ε	Relative permittivity
ε_0	Free space permittivity
φ	Magnetic flux
I	Electrical current
E-field	Electrical field
S_1	Rectangular coil width
S_2	Rectangular coil length
L	Coil inductance
C_t	Tuning capacitor
C_T	Total capacitance on RF coil
C_m	Matching capacitor
Q	Quality factor
ζ	MRI received signal
V	Sample volume
j	Imaginary number (root(-1) number
PL	Dissipated power
S(r)	Image signal intensity
c	Free space light speed
λ	Free space wavelength
n	refractive index
D	Digit length
L	The length of strip line
N	The number of strip lines
w_d	The width of strip lines
g_d	The gap between each strip line
J_c	Conductive current density
Y_0	Free space admittance
σ	Electrical conductivity
ε_{eff}	Effective medium permittivity
K(k)	Complete elliptic integral
P_{absNM}	Absorbed power in the whole system without metasurface
P_{absM}	Absorbed power in the whole system with metasurface
$P_{abs\ coil}$	Absorbed power in the RF coil
$P_{abs\ ph}$	Absorbed power in the dielectric phantom
$P_{abs\ meta}$	Absorbed power in the metasurface
β	Free space propagation constant

B_{1^-nor}	Normalized negatively rotated magnetic flux density
η	The percentage improvement in transmission efficiency of RF surface coil
Ψ	Receiver sensitivity in 2D
$\triangle\Psi$	The percentage improvement in receiver sensitivity of RF surface coil
S_{11}	Forward reflection coefficient
S_{21}	Forward transmission coefficient

Table of contents

List of Figures

List of Tables

Chapter 1

Introduction and Background

1.1 Introduction

Magnetic resonance imaging (MRI) has been widely used in medical imaging due to its advantages of non-invasive procedure and high accuracy. The imaging process of MRI is based on nuclear magnetic resonance (NMR), which does not involve ionizing radiation. At present, people have increasingly higher demands for imaging quality and imaging speed, and they even pursue for multi-nuclei imaging. Therefore, the optimization of MRI systems has become a hot research issue. The imaging quality of MRI systems depends on the spatial resolution, image contrast and signal to noise ratio (SNR). SNR is characterized to the magnetic field strength of an MRI system, the proton density of imaged area or coil type. The magnetic field strength of an MRI systems is determined by two factors, i.e. the static field strength H_0 generated by the permanent magnet, and the external magnetic field H_1 generated by the radio frequency (RF) pulse from the RF coil. SNR can be improved by increasing H_0, which means using high-field-strength systems, such as 4T or 7T MRI. High-field-strength MRI systems can obtain better image quality in a higher imaging speed compared with low-

field-strength MRI systems. However, high-field-strength MRI systems increase the E-field while increasing the SNR, thus causing some health risks as more thermal energy is absorbed by the patient's body. Therefore, most of MRI systems used in hospitals have low field strength, with the proportion of 1.5T systems exceeding 70%. As a result, improving the SNR of MRI systems by increasing B_1 in low-field-strength MRI systems is more beneficial.

^{1}H is the major nuclei adopted by MRI systems, because of its high ratio in human body. However, ^{1}H is not the best nuclei for all imaging tasks. Many studies have reported that ^{1}H detection is not the only way to obtain the information of human body. For example, human metabolism can be examined by ^{31}P using high energy phosphates [1][2]. The information on the balance of glucose and glycogen can be provided by ^{13}C [3][4][5]. The detection of tumorous tissues or cartilage can be achieved by ^{23}Na [6][7][8]. If several nuclei are required to be imaged in one MRI process, people usually choose to image each nucleus independently to ensure the accuracy of images, but imaging speed will be decreased and costs will be increased, which may occupy many medical resources. Therefore, multi-nuclei imaging in one MRI procedure has become a key issue needed to be solved in the development of MRI systems.

1.1.1 Problem description

The research on high-field-strength MRI systems such as 7T MRI systems has achieved many improvements in image quality and imaging speed by increasing the SNR through increasing static field strength. However, high-field-strength MRI systems also bring a problem, that is, the increment in human tissue temperature due to the higher specific absorption rate (SAR). This is the reason why our research focuses on 1.5T MRI systems. Changing coil type is an efficient way to increase the SNR of MRI systems, such as using birdcage volume RF coils. However, birdcage volume RF coils are not suitable for all imaging tasks, such as cervical spine imaging and thoracic imaging.

Besides, the cost of using birdcage volume RF coils is much higher than that of using other coil types. Therefore, people are interested in increasing the SNR of MRI systems without increasing the static magnetic field or changing the coil structures. Luckily, previous research has shown the great potentials of metasurface in improving the performance of MRI systems by its flexible electromagnetic properties. However, most of the existing researches are based on high-field-strength MRI systems, because their periodic structures are limited by the resonant frequencies. High resonant frequencies and high field strength lead to increase the dimensions of metasurface in further. Therefore, there is still a lot of room for improvement in the low field strength MRI systems.

Some approaches have shown their effectiveness in achieving multi-band imaging, like adding extra RF loops or micro-electromechanical systems (MEMS) switches. Most of the research cannot keep the value of SNR at focused resonances, because of the mutual coupling between RF loops, or the extra elements in transceiver systems. The application of metamaterials in multi-nuclei MRI systems is still a challenge, because of the difficulty in combining multi-band RF transceivers with the periodic structure of metamaterial. Moreover, the periodic structures of metamaterial are very complex and have the difficulty in being designed for multi-band imaging at low-field-strength.

1.1.2 Objectives

In this thesis, a 1.5T MRI transceiver system is optimized by applying a metasurface to enhance magnetic flux density B_1 and achieve dual band nuclei imaging. The nuclei researched in this thesis are ^{19}F and ^{1}H, with resonant frequencies of 60.08MHz and 63.85MHz in 1.5T MRI, respectively.

The main objectives of this research include:

1) A non-periodic metasurface will be placed between the RF transceiver coil and the dielectric phantom to enhance the magnetic flux density B_1, and increase the SNR of

1.5T MRI. The interdigital capacitance approach will be used to miniaturize the dimension of metasurface.

2) The metasurface in non-periodic structure will be considered to achieve the multi-nuclei imaging. The factors influence the frequency of extra resonances, and the transceiver performance should be investigated.

1.1.3 Areas of novelty and originality

This thesis proposes a novel design of non-periodic metasurface to enhance the magnetic flux density to increase SNR, and generate an extra frequency band to achieve dual-nuclei imaging in 1.5T MRI systems. The areas of novelty of this thesis is summarized as follows.

1. The non-periodic metasurface is used to optimize the single frequency band in a 1.5T MRI system. At present, most of the metasurfaces used in MRI system optimization were developed based on periodic structures, such as magneto inductive lens, capacitive loaded rings and high impedance surface. However, the miniaturization of these designs is a big problem due to the low frequency band. High-field-strength MRI has larger resonant frequency to make the miniaturization of non-periodic structure become much easier. By contrast, low-field-strength MRI systems have received relatively less attention. The non-periodic metasurface used in this thesis will solve this problem, because it has flexible structure and its dimension only controls the capacitance of the metasurface. Then, lower SAR is obtained compared with periodic metasurface, as the non-periodic structure does not enhance B_1 by focusing the field. Finally, the even distribution of field is achieved by the non-periodic structure while it is a difficult thing for periodic structures, which is beneficial for imaging.

2. The non-periodic metasurface is used to generate an extra frequency for dual-band nuclei imaging, by the coupling between RF coil and the metasurface. In this case, dual loop RF coil is used to adjust the two resonances, which has a single RF one the outer

coil. According to the previous research on dual-band nuclei imaging, the RF performance in these researches can not be the same as the RF performance when using single RF coils separately. For example, extra trap circuit used to reduce the coupling between two RF feds coil will cause extra power loss, or the additional resonators will produce noise to reduce the overall SNR. These problems can be solved by using single RF fed coil, so that the performance of RF coils will not be influenced, even get some improvements at focused bands. Then, compared with the research which only applied metamaterials in the MRI system [9], the non-periodic metasurface used in this research has much simpler structure, and will not be limited by the field strength of MRI.

1.1.4 Thesis overview

Chapter 1.2 introduces the background of the research and demonstrates all the parameter used. The fundamentals of MRI are introduced to explain the working principle of MRI systems. The key parameters influence the imaging quality are also elaborated. Then, the methodology of 'surface impedance' which used to predict the parameters of the metasurface in simulation will also be described.

Chapter 2 presents the literature review, which is a complete overview on the research area and related topics in this field to show the novelty and improvement of this project. This chapter consists of two parts. The first part introduces some representative research which applied metamaterials to optimize MRI systems at single band. Many metamaterials in different types have been developed to enhance the SNR of MRI systems. The second part focuses on the researches focused of multi-nuclei imaging. This field has been extensively investigated, but rare research used metamaterials to achieve multi-nuclei imaging, and there was no research using metamaterials to achieve multi-nuclei imaging in low-field-strength MRI systems.

Chapter 3 describes a method for designing a non-periodic metasurface for enhancing single frequency band in 1.5TMRI. The use of an inter-digitated capacitive surface

combined with a rectangular RF transceiver coil is adopted to improve B_1 at 63.85MHz for hydrogen imaging in a 1.5T MRI system. Simulation results show how the metasurface can significantly improve the B_1, with the non-periodic metasurface placed between the RF coil and the dielectric phantom. The measurement results from both RF bench and the 1.5T MRI system are presented in this section. The factors of S-parameter, flip angle and SNR are also investigated for performance evaluation.

Chapter 4 presents the use of the developed non-periodic metasurface to achieve multi-nuclei imaging in a simulated 1.5T MRI system, and why it generates extra resonances will be discovered by adjusting different parameters In this case, the imaged nuclei are ^{19}F and ^{1}H, with their resonant frequencies being 60.08MHz and 63.85MHz, respectively, for the field strength of 1.5T. The rectangular RF coil is replaced by single fed dual loop RF coil. The S-parameter is calculated when the distance between each component to prove the extra band is provided by the coupling between the RF coil and the metasurface. B_1 is measured to evaluate the performance of the transceiver system. Two metasurfaces are designed to obtain two frequency bands at 60.08MHz and 63.85MHz. In addition, this research presents the use of non-periodic metasurface to enhance the SNR of low-field-strength MRI systems for the first time.

Chapter 5 presents the whole measurement procedure and the results obtained with the metasurface of l=97.1 mm, g_d=0.8 mm, and w_d=1.8mm. Two different dielectric phantoms are measured in this case. One is the dual-layer phantom, which has the same hydrogen layer as the model in simulation, to verify the simulation results. The other phantom type is the embedded structure. The fluorine phantom is a plastic bag full with dry fluorine gas and put into the hydrogen phantom, which is a container full with CuSO4 squid. This phantom is more similar to the human body.

Chapter 6 gives a conclusion and future work regarding the achievements of each chapter. Two tables are used to show the difference and improvements compared with previously-proposed models. The performances of single and dual band imaging are also compared, so as to highlight the novelty of proposed design.

1.2 MRI system overview

Comparing with other imaging techniques, MRI systems have many advantages that can be used in most organ imaging. High resolution and contrast, the contents of hydrogen nuclei are different in fat, carbohydrates and protein etc. MRI systems can image white matter and grey matter in the spinal cord, and nerve with lesion much evident than computed tomography (CT). MRI can achieve tomography for any surface. The linear gradient fields involve three mutual orthogonal gradient field, slice selection gradient field, phase encoding gradient field and frequency encoding gradient field. Therefore, MRI can complete tomography for any surface in the imaged object.

In MRI systems, the RF (radio frequency) pulse emitted by the RF coil is used to excite hydrogen nuclei in the static magnetic field generated by the permanent magnet. Then, the free induction decay (FID) signal generated by excited hydrogen nuclei will be rebuilt as MR signal which involves space encoding information by applying three gradient fields orthogonal to each other, and MR signal will be detected by RF coil to create images. In short, the MRI technique is based on the nuclear magnetic resonance (NMR) phenomenon that the nuclear spin alignment in the static magnetic field was excited by RF pulse, which is non-invasive instead of relying on harmful ionizing radiation, such as x-rays. According to these advantages, MRI systems become the cornerstone technique of diagnostic medicine, biology and neuroscience. How to improve MRI system become necessary and imperative.

1.2.1 MRI system and the function of each component

The cross-section of the MRI system is shown in Fig. 1.1 The details of each component and their function will be analyzed in the following parts.

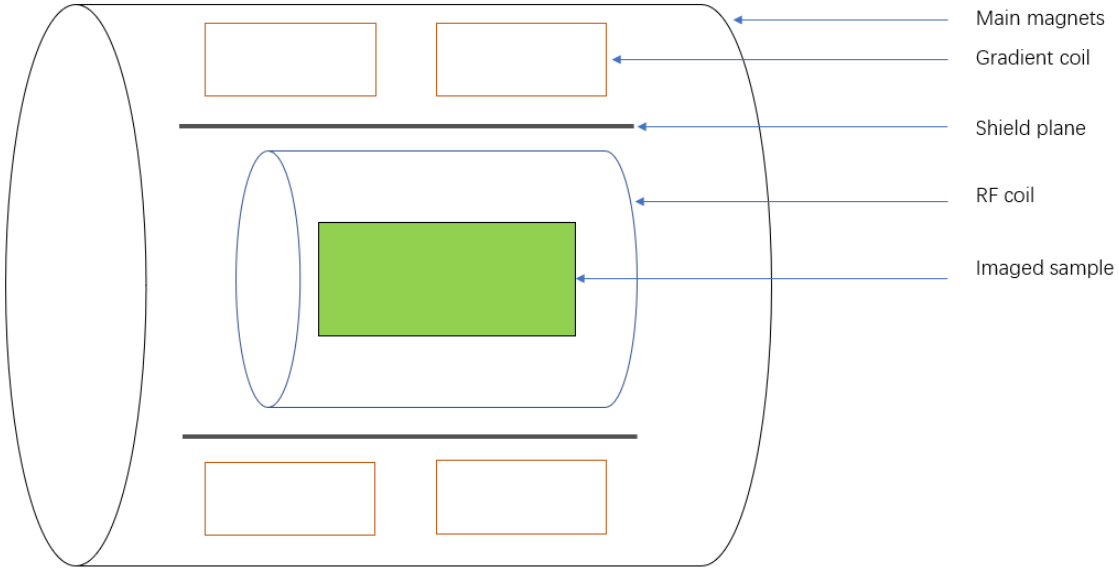

Fig. 1.1 Schematic diagram of MRI system

1.2.1.1 The MRI static magnetic field

The static magnetic field is generated by the main magnets on the outset size of the MRI system.[10] The static magnetic field is strong, homogeneous and stable. Its strong field strength aligns the randomly-orientated magnetic moment of nucleus parallel or antiparallel to the main static field, which will be discussed in later parts in more details. The homogeneity of the static field reduces the phase coherent phenomenon, and the stability will be needed to avoid artefacts into MRI images. [11]

There are three kinds of magnets used in the MRI systems. They are permanent magnets, resistive magnets and superconducting magnets. [12] MRI systems with the type of permanent magnet are stacked with magnetic bricks made of ferromagnetic materials. The advantages are relatively low costs and maintenance costs. There is no additional equipment required, such as electrical energy or cooling devices. The field strength of permanent magnet MRI systems are always lower than 0.7T, and has acceptable image quality for many health examinations. The disadvantages of this MRI system are the low imaging quality and poor uniformity due to the limited SNR from low field

strength.[13]

The magnets in resistive magnet MRI systems is composed of several groups of cylindrical coils wounded by aluminum or copper wires. The magnetic field can be generated when the power is supplied at normal temperature. This system can be switched off, which is in terms of safety. A larger number of metal wires will form as resistance and consume a lot of electrical power, and the resistance generates a lot of heat. [14] Therefore, a larger amount of circulating water is required to cool system, and requires high maintenance costs. In the practical applications, the field strength of resistive magnet MRI systems is low, which based on 0.2T to 0.4T. The uniformity of the magnetic field is greatly affected by the external environment, such as temperature. The sales of this type of MRI system is limited.

The heating problem can be solved by minimizing the resistance of the conductor by using the superconducting magnets. One of the most commonly used superconducting coils is wounded by the cooper wire coated with niobium-titanium alloy, which has low resistance (up to zero) at low temperature provided by helium liquid.[15] The superconducting MRI systems consist of superconductive RF coil, helium liquid, vacuum space, nitrogen liquid, vacuum space and circulating water in the order from inside to outside. When the superconductive coil is at the ultra-low temperature (-263° to -269°) provided by the helium liquid, the resistance of the niobium-titanium alloy is significantly reduced, a the RF coil non longer consumes electrical power, and superconductivity occurs. Since the conductor resistance is very small under this situation, so higher current can pass through the coil and generated extremely high magnetic field. [16] At present, superconducting MRI system is widely used in clinic, the most common are 1.5T and 3T. The disadvantages are the high manufacturing costs and maintenance costs, because nitrogen liquid needs to be replenished regularly. MRI systems with permanent magnets and superconducting magnets are the most commonly used in medical imaging up to date, the photo of each type is shown in Fig. 1.2 (a) and (b).

(a) (b)

Fig. 1.2 MRI system photos, (a) with permanent magnets, (b) with superconducting magnets

1.2.1.2 Gradient coils

The gradient coil is one of the most important parts of the MRI systems. The images provided by MRI systems comes from the free induction decay (FID) signal, which will be discussed in detail in the later section. The FID signal has a very short duration, so it can not be used to acquire image directly. As a result, MRI systems need a method to differentiate FID signal spatially to obtain the images of the imaged sample at specified positions. [17] Gradient coils in the MRI systems can generate three mutually orthogonal and controllable gradient pulses (Gx, Gy, Gz) to provide another magnetic field overlap with the main magnetic field and spatially encode MR signals to complete the spatial location, so determining the location and the depth of the required image. [18]When the gradient magnetic field is applied to the main magnetic field, the field strength will be distributed linearly with the position. Thus, the position of the image can be defined by the field strength at a specified location. For example, we define Br is the flux density at the position r of the required image, and gradient amplitude at this position is Gr, and the original flux density B_0. When $Br=B_0$, $r=0$. When $r \neq 0$, the relationship between them can be defined by:

$$B_r = (B_0 + rG_r) \qquad (1.1)$$

Therefore, the strength of the gradient field can be adjusted, when the amount of current passing through the gradient coils is controlled. [12]

1.2.1.3 The MRI radio frequency (RF) system & RF coil

The function of the RF system in MRI systems is to provide an RF pulse and external magnetic field. Then, a magnetic flux density B_1 is produced, and the net magnetization vector of the imaged nuclei from longitudinal direction is flipped to transverse direction by a flip angle.[19] The B_1 is defined to be always perpendicular to the static magnetic field at the Larmor frequency of the imaged nuclei. The nuclei receive the energy provided by the RF pulse and be resonance, when the RF transmit coil is switched on. This process call excitation. After the RF transmit coil is switched off, the energy released during the relation of the nuclei will generate MR signal, and be captured by the receive coil. The transceiver coils used to transmit or receive signal is used in MRI systems at the same time. If the RF coil is placed closer to the imaged sample, the MR signal will be stronger to increase the SNR. Therefore, different shapes and types of RF coils are required for different imaging tasks to obtain the maximum SNR and best image quality. [20]

There are two common RF coil types used in MRI system nowadays, they are volume coil and surface coil. A spatially uniform magnetic field over the whole imaged sample can be generated by the volume coil in terms of 'birdcage'. The birdcage coil is usually used to image brain, knee and abdominal. [21] The surface RF coil is often used to image parts at the surface of the body, such as artery or cervical spine. Surface RF coil has higher sensitivity than volume coil. [18] Fig. 1.3 and Fig. 1.4 shown the photos and the simplified diagram of birdcage RF coil for brain imaging, and the surface RF coil

for cervical spine imaging. [22][23]

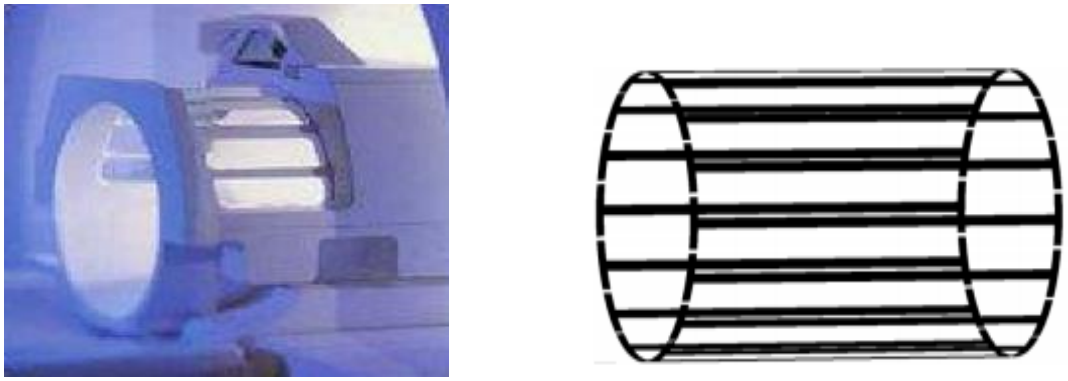

(a) (b)

Fig. 1.3 Birdcage volume coil, (a) practical photo (b) schematic diagram

(a) (b)

Fig. 1.4 Surface coil, (a) practical photo (b) schematic diagram

1.2.2 Physical basis and theory of MRI system

1.2.2.1 Nuclear magnetic resonance

MRI is an advanced and non-invasive medical imaging approach, which is used to yield the specified nucleus in biological sample based on the nuclear magnetic resonance phenomenon (NMR), which was indicated by Bloch [24] and Purcell in 1946. [25] NMR is a physical process describe the spin energy level of the nuclei has a non-zero magnetic moment, will undergo Zeeman splitting, resonates and absorbs RF energy at

the specified frequency under the action of an external magnetic field.

The whole human body is consisting of atoms. Different atoms could construct different elements. For example, human body consists of approximate 68% water and 23% fat, hydrogen (^{1}H) is the highest-content atom found in molecules of water and fat. [26] As a result, hydrogen is the most abundant atom in the human body, and is the most commonly imaged atom used in imaging. The most commonly element used in MRI is hydrogen (proton) (^{1}H). In 1.5T MRI system, hydrogen nuclei will resonant at 63.85MHz. In the Table.1, there are some nucleus commonly used in MRI and their processional frequency in 1T MRI system.

Nucleus	Spin	Processional frequency (MHz/T)
Proton	1/2	42.58
Helium	1/2	32.43
Fluorine	1/2	40.06
Sodium	3/2	11.26
Phosphorus	1/2	17.24

Table. 1.1 Features of nucleus is in high abundance in human body

1.2.2.2 Magnetic moments and nuclei spins

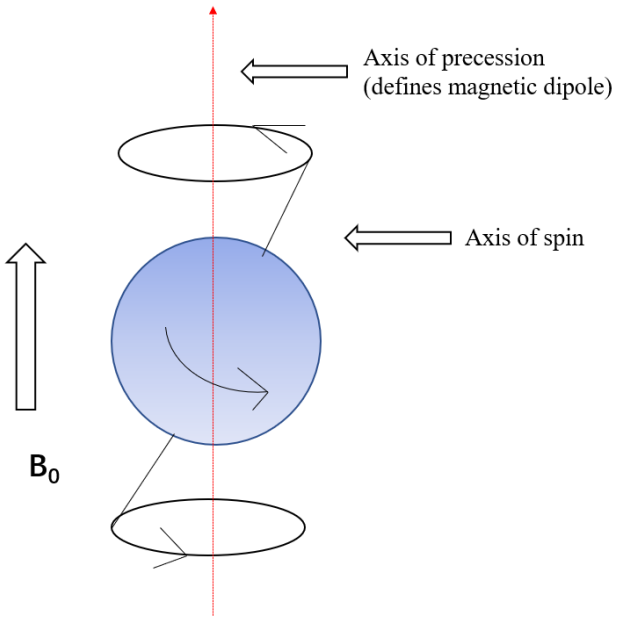

Fig. 1.5 Precession

The atom consists of a central nucleus and orbiting electrons. The nucleus consists of protons which have positive charge, and neutrons which has no charge. The electrons have negative charge and negligible mass. The atomic number is equaled to the sum of protons in the nucleus, and the mass number is the sum of the protons and neutrons in the nucleus. When nuclei have an even mass number, the number of protons equals the number of neutrons, half spin in one direction and half in the other, and nucleus has no net spin. When nuclei have an odd mass number, the number of protons does not equal to the number of neutrons, spin direction not equal or opposite. Thus, nucleus has net spin or angular momentum. These are called MRI active nuclei. [27] When applying a magnetic field at their resonant frequencies, MR active nuclei align their axis of rotation to the direction of the static magnetic field with their tendency, because they have spin angular momentum, and have an electrical charge. In absence of applied magnetic field, the magnetic moments are randomly orientated. The magnetic moment of the nuclei will occur deflection, and has an angle between the directions of the static magnetic field. At this time, nucleus will not only spin along its own axis, but also rotated along the direction of the static magnetic field. This called Larmor precession. This procession

showed in Fig. 1.5. The value of the processional frequency/resonant frequency per tesla of the imaged nuclei can be defined by the Larmor equation, which is stated by:

$$\omega_0 = B_0 \times \lambda \qquad (1.2)$$

Where ω_0 is the processional frequency, and B_0 is the magnetic field strength of the magnet. λ is the gyromagnetic ratio, which expresses the relationship between the angular momentum and the magnetic moment of each MR active nucleus.[28]

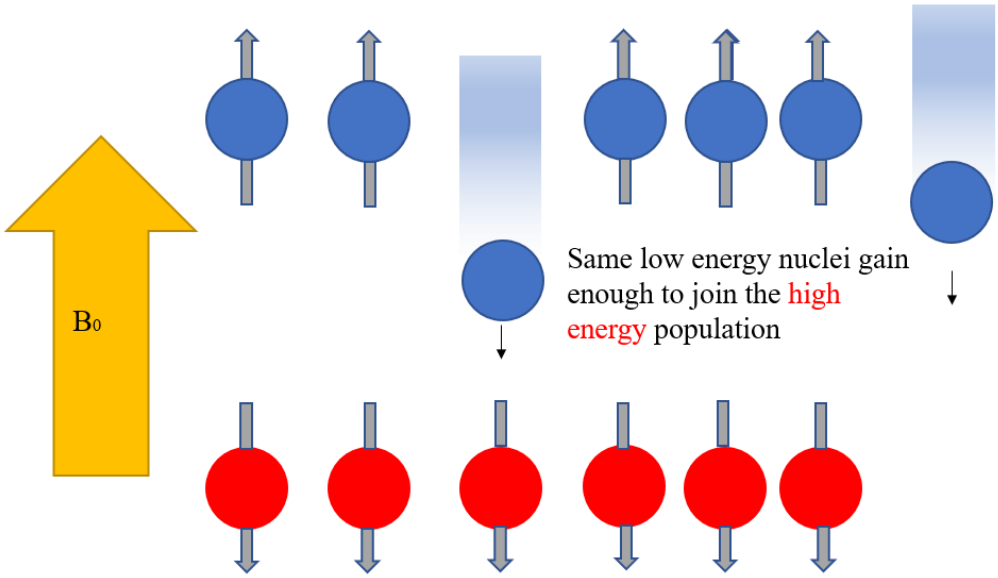

Fig. 1.6 Energy transfer during excitation

It will be much easier to use quantum theory to understand how the magnetic field to influence the motion of nuclei. From the Fig. 1.6, low energy spin-up nuclei are parallel with the magnetic field, and high energy spin-down nuclei are anti-parallel with the magnetic field. In thermal equilibrium, there are more low-energy nuclei than high-energy nuclei, thus the magnetic moments of nuclei aligned parallel to the static magnetic field cancel out the magnetic field of fewer nuclei aligned anti-parallel. [29] This small excess in this direction produce a net magnetic moment. This magnetic

vector called net magnetization vector (NMV) and responses to the difference between spin-up and spin-down nuclei. The magnetization vector influenced by static magnetic field wrote as M_0, which parallel to the static field along z-axis.

The effects from static magnetic field strength of MRI system on SNR could also be explored from a micro perspective. When field strength increases, the energy gap between high-energy and low-energy nuclei will also be increased. As a result, fewer nuclei have enough energy to align with the direction opposite to main static field. Then, the number of spin-up nuclei increases and spin-down nuclei decreases. The NMV therefore increases in the higher field strength, and there will be more magnetization to image the patient. High field strength could provide better signal but will cause some safety risks. Thus, the low field strength MRI is much suitable for most imaging tasks. [30]

1.2.2.3 Radiofrequency pulses and rotation frame of magnetization

In MRI systems, the receiving coil only could receive the signal when the coherent magnetization cut across the coil, and the longitudinal magnetization vector of nucleus could not occur only oscillating in the static field. Thus, another external magnetic field which perpendicular to the static magnetic field generated by RF pulse from the RF coil. Before discussing the next part, the theory of resonance should be discussed. [31] When an object exposed to an external perturbation oscillation which has a similar natural frequency as its own natural frequency, the nucleus could obtain energy from this force. When there was an external strong magnetic field with the same resonant frequency as the atomic nuclei used to image applied into a static magnetic field, the atomic nuclei which have same resonant frequency will resonance, and this call excited. The nucleus gains energy from the external force when it is exposed to the external perturbation has an oscillation similar to its resonant frequency, this phenomenon is called resonance. As a result, more low-energy nuclei absorbed energy from the RF pulse to become high-energy nuclei. As NMV reflects the balance between the low and high-energy

population, so NMV will no longer parallel to static field and there is an angle between NMV and the static field. This angle called flip angle, and its magnitude depend on the amplitude and duration of RF pulse, which is defined as:

$$\alpha = \gamma B_1 \tau_{B_1} \qquad (1.3)$$

In MRI system, 90° flip angle usually required which used to move NMV move through 90° to the static field, and have new magnetization vector M_1. Then, the longitudinal magnetization vector M_z of NMV along to the static field (along z-axis, longitudinal plane) will be rotated 90° to M_{xy} (along *xy*-axis, transverse plane). When the original magnetization M_0 of NMV influenced by the external magnetic field H_1 provided by 90° RF pulse, longitudinal magnetization M_z was kept decreasing to 0°, and transverse magnetization M_{xy} was kept increasing to equal to the magnitude of M_0. This rotation progress shown in Fig. 1.7.

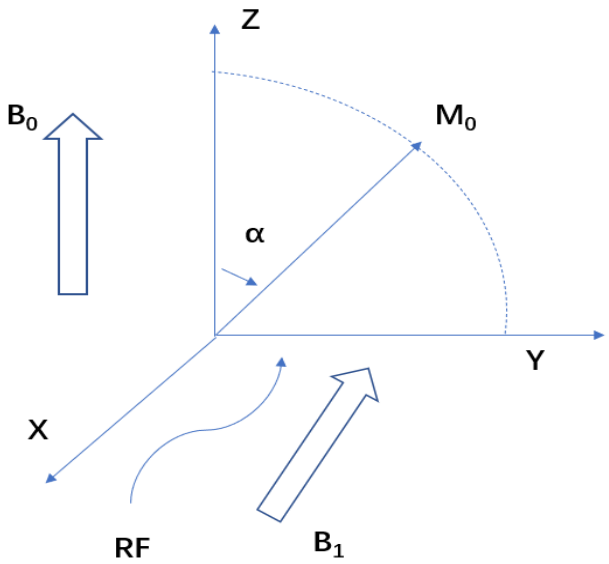

Fig. 1.7 Rotation of longitudinal magnetization during B1 excitation

1.2.2.4 Free induction decay (FID)

When the RF pulse is switched off, some spin-down nuclei will release energy and return to spin-up nuclei. Therefore, the magnetization vector M_1 returned from the M_{xy} to M_z. This is called relaxation process. Besides, after RF pulse removed, the time constant for the amount of longitudinal magnetization M_z recovered from 0 to 63% called T1 recovery time. The time constant for the amount of transverse magnetization Mxy decayed to 37% called T2 decay time. However, static magnetic field H_0 could not be absolutely homogeneous, so in some cases, decay time constant is T2* instead of T2.

$$T2^* = \frac{1}{\frac{1}{T2} + \gamma \triangle B0} \qquad (1.4)$$

where △B0 is magnetic field difference between hydrogen nuclei.

If one receiving coil was placed on the x-y plane, and transverse magnetization M_{xy} will cut receiving coil, because M_{xy} decayed from M_0 to 0. The procedure of M_{xy} decayed to 0 called free induction decay (FID), which shown in Fig. 1.8.

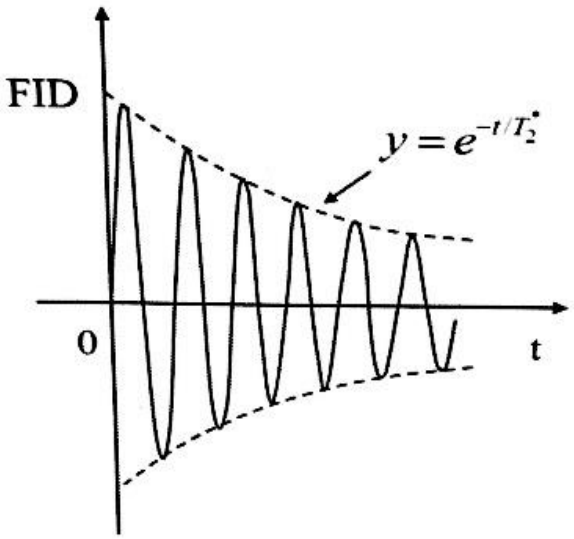

Fig. 1.8 Diagram of FID signal

According to Faraday's law of electromagnetic induction, there will be current induced on the receiving coil because M_{xy} cuts coil, so creating induced voltage and FID signal.[32] FID signal will be used to generate the image after the spatial differentiated encoded by the gradient pluse. The FID signal is proportional to the rate of time-varying magnetic flux, which generated by bulk magnetization precession:

$$FID = \frac{-d\varphi}{dt} \qquad (1.5)$$

Where φ is the magnetic flux density provided by the RF coil.

Thus, gradient coil was required to further process the FID field. The MR signal could be completed the spatial location by three mutually orthogonal and controllable gradient pulses (Gx,Gy,Gz) provided by the gradient coil. [33] After RF pulse was applied to FID signal was created, and gradient pulse Gz was applied simultaneously to finish slice selection. [34] Then, RF pulse was switched off, out-of-phase gradient pulse Gy was applied to make the precession frequency of nuclei changed. The phase of each nuclei become different, as frequencies are different along the gradient. Consequently, the speed of FID signal decreased was accelerated. Finally, one 180° gradient pulse Gz with the same amplitude but the opposite direction was applied. At this time, the phase difference between each nucleus does not change, but the direction become opposite. Therefore, the nuclei with higher procession speed will behind the nuclei with lower procession speed. After a period, nuclei with higher procession speed will catch up the nuclei with lower precession speed, and phase difference between all nuclei will be cancelled. Next, the transverse magnetization will be assembled, and the MR signal achieve maximum value. The slice selection gradient Gx was applied to complete the spatial encoding of MR signal. Finally, receiving coil received the MR signal with spatial encoding, and then use this information to finish the MR image creation.

1.2.3 Key parameters in the MRI systems

1.2.3.1 Parameters of MR image quality

The image quality of the MRI system depends on several parameters, such as spatial resolution, contrast to noise resolution, signal to noise ratio and scan time. The spatial resolution is mainly depended on the uniformity of the static field and encode samples in the MRI systems, and the field of view (FOV), slice thickness, and k-space matrix size or bandwidth per pixels are included in the matrix of spatial resolution. The contrast resolution is in terms of the differences in adjacent areas in signal intensities from the imaged sample. The scanning time is the time period to receive and decode the MR signal. The last and the most important factor is the signal to noise ratio (SNR), which gives the ratio of the MR signal received from the imaged sample to the background noise. They will be discussed in details in this case, especially the SNR which is one of the most important parameters focused in this dissertation.

1.2.3.2 MRI spatial resolution

The spatial resolution in the MRI system depends on a specific imaging sequence, and it is deferent in three spatial dimensions. When keeping all of other parameters in constant, the spatial resolution can be enhanced by increasing the number of phases encode samples or frequency encode samples. [35] Increasing the number of phases encode samples or frequency encode samples will make the k-space matrix size increase, so extra data storage memory is required. When the voxel size controlled by spatial resolution decreased, the SNR can be increased. [36]

1.2.3.3 The MRI image contrast

The MR signal is influenced by the density of the imaged nuclei at the specified part, and the image signal is generated by a map if the signal intensity at the focused area.

[37] For example, the density of ^{1}H in our body is different in each part, so the image contrast which depends on the ^{1}H density will be different. During imaging the tumor in our body, the tumor will be imaged much clear than other organs, due to the higher image contrast given by the higher ^{1}H density in the tumor and differences in relaxation times. [38] Both the amplitude and timing of the RF pulse can adjust the image contrast, which excites the imaged nuclei.

1.2.3.4 Scanning time

Scanning time and image quality are two major parameters used to indicate the performance of one MRI system. [39] Parallel magnetic resonance imaging (pMRI) is an effective method to accelerate the speed of catching data, but this method based on changing RF coil array, and will cause aliased images. In further, MRI requires multi-slice, multi-sequence, and multi-phase selection, so changings in coil arrays are limited. One of the most famous structure is the 'NMR phased array' published by Roemer, which helps to acquire and combine data simultaneously and subsequently. [40] The other effective way is increasing static magnetic field strength to enhance FID signal directly, so MR signal gets enhancement and imaging speed obtains significant improvement. However, the high magnetic field strength will bring some safety risks to the human body, which embodied in the value of specific absorption rate (SAR) increased. As a result, high magnetic field strength MRI such as 7T MRI is still in the development stage, and low magnetic field strength MRI like 1.5T and 3T MRI are more often used.

1.2.3.5 Signal to noise ratio

Signal to noise ratio (SNR) is one of the most important parameters to the transceiving performance of an MRI system, and proportional to the image quality. It is normalized

to the rate of power of signal and power of background noise. There is something different from the SNR in MRI systems to communication systems.

The SNR in MRI system could be expressed by the formula:

$$\mathrm{SNR} \propto f^2 \frac{|\sin(VB_{1c}^{+}\gamma\tau)B_{1c}^{-}|}{\sqrt{P_{abs}}} \qquad (1.6)$$

Where B_{1c}^{+} is B_1^{+} of the centre voxel, so does B_{1c}^{-}. B_1^{+} and B_1^{-} are the positively rotating frame and negatively rotating frame flux density of the B1 field (RF magnetic field) respectively. τ is the duration of the RF pulse, and γ is the gyromagnetic ratio of H1. P_{abs} is the power absorbed by the entire body, and is related to specified absorption rate (SAR). Here, SNR can be defined to be proportional to B1-/$\sqrt{P_{abs}}$. [41]

In MRI system, B_1 consists of two parts B_1^{+} and B_1^{-}. If Z-axis is defined as the direction of the static magnetic field, B_1^{+} is the positively rotating frame of reference and transmitting field pattern, which is defined as

$$B_1^{+} = \frac{B_x + jB_y}{2} \qquad (1.7)$$

B1- is the negatively rotating frame of reference and receiving field pattern, which is defined as

$$B_1^{-} = \frac{(B_x - jB_y)^*}{2} \qquad (1.8)$$

As shown above, SNR is proportional to the product of the RF transmit field (B_1^{+}) and the complex conjugate of the receive sensitivity (B_1^{-}). [42]

The relationship between the signal induced in coil S by processing nuclear magnetic moment M is proportional and the strength of rotating the RF magnetic field B_1 can be

defined as:

$$S = \frac{d}{dt}(B_1 \times M) \qquad (1.9)[41]$$

In the experimental methods, the two regions method is also used to measure the SNR of the MRI system. The signal statics in two different locations (ROI) are selected, one in the high-intensity region from the imaged sample to determine image intensity S(r), the other one in the low-intensity region from the image background to determine the noise intensity and give standard deviation σ_{st}. Then, the SNR of the MRI system can be calculated as:

$$SNR = \frac{S(r)}{\sigma_{st}} \qquad (1.10)$$

1.2.3.6 Specific absorption rate

Although the MRI system is safe for patients, the biologic effects from RF field should not be ignored during designing. One of the most significant safety problems needed to think about is tissue heating caused by RF absorption.

Specific absorption rate (SAR) is defined as the rate responses to the energy absorbed by the human body when exposed to the electromagnetic field at the radio frequency. [43] SAR is a standard to judge if the design is harmless to the human body or not. In software simulation, the SAR is investigated inside the homogeneous dielectric phantom, and units are W/kg. Therefore, SAR should be tested in each case, and it was an important parameter to decide if the design could be used in human body MRI, and be defined as:

$$SAR = \frac{1}{V}\int_{Sample} \frac{\sigma(r)|E(r)|^2}{\rho\ (r)} dr \qquad (1.11)\ [44]$$

Where σ is the sample electrical conductivity, E is the RMS electric field, ρ is the

sample density, and V is the volume of the sample.

Eliminating the whole-body SAR testing, there is partial body SAR testing which is defined as the average SAR value over the 10g arbitrary human tissue. This partial calculation sometimes will provide more precise results, because different locations in human tissue have different ingredient and sensitivity to the magnetic field. This is the reason why different tissue has different SAR limits.

1.2.3.7 Impedance matching

In order to optimize the radiation performance, impedance match is a useful way to 'offset' the imaginary part of the impedance and maximum power transmission.[45] According to the formula

$$\Gamma = \frac{Z_L - Z_S}{Z_L + Z_S} \qquad (1.12)$$

where Z_L is load impedance, Z_S is the impedance toward the source which is 50Ω. When reflection coefficient Γ equals to zero, means no energy reflect. Thus, ZL should be equalled to Zs as much as possible. The imaginary part of load impedance could be cancelled by connecting extra capacitors. Good impedance matching could maximize the power transfer or minimize signal reflection from the load.

In this case, one additional variable capacitor C_{match} was used to change load impedance Z_L to match impedance.

Chapter 2

Literature review

2.1 Introduction

This chapter consisting of two parts.

The first part will introduce the theory and the background of the metamaterial, which is the most important approach used to achieve targets in this research. Then, the working principle of different types of the metamaterial will be discussed with their applications in the single band optimization work in the different parts of MRI systems. The second part presents some current methods used to achieve multi-nuclei imaging in MRI systems. These methods were not all based on using metamaterials, because the researches of metamaterials in multi-nuclei MRI is very few.

2.2 Metamaterial

2.2.1 Literature review of metamaterials in MRI for single band optimization

Metamaterial is a big family whose dielectric properties controlled by its structure or materials. Metamaterials are man-made composite materials which do not exist in nature. Therefore, metamaterials could be given specified property that can not be achieved by natural material under special application requirement. By adjusting the structure and materials, metamaterials could have any value of effective permittivity or permeability. Another important feature of metamaterial is the negative refraction index (n=-1). [46]

The metasurface can be defined as a two-dimensional textured structure, which can be created by printing the metal with special texture or material on the dielectric substrate. The most popular and basic of the metasurface are defined as the patch arrays and aperture elements which acts as a capacitively or inductively surface respectively. These structures are also known as frequency selective surface (FSS).[47][48] The top view and equivalent circuitry of each metasurface are shown in Fig. 2.1. One of the most important properties of FSS is the filter design. The metasurface in patch arrays always work as a band-stop filter, and the metasurface in aperture elements will be defined as a band-pass filter. For example, the band-stop property can be used to limit the use of mobile phones in a special place like in hospital departments, and the FSS will be printed on the wall and the windows of the buildings. Frequency selective surface has been studied for many applications in the different technical area, such as daily microwave, military industry and antenna transceiver systems. [49] For example, FSS can be designed as the isolative material for reducing the radar cross-section (RCS) of antennas at the out-of-band frequencies. FSS can also be used in the radar absorbing material (RAM) to absorb the electromagnetic wave in some technology, such as the reconnaissance aircraft.

In the following sections, metamaterials in some typical structures will be illustrated with their applications in MRI systems.

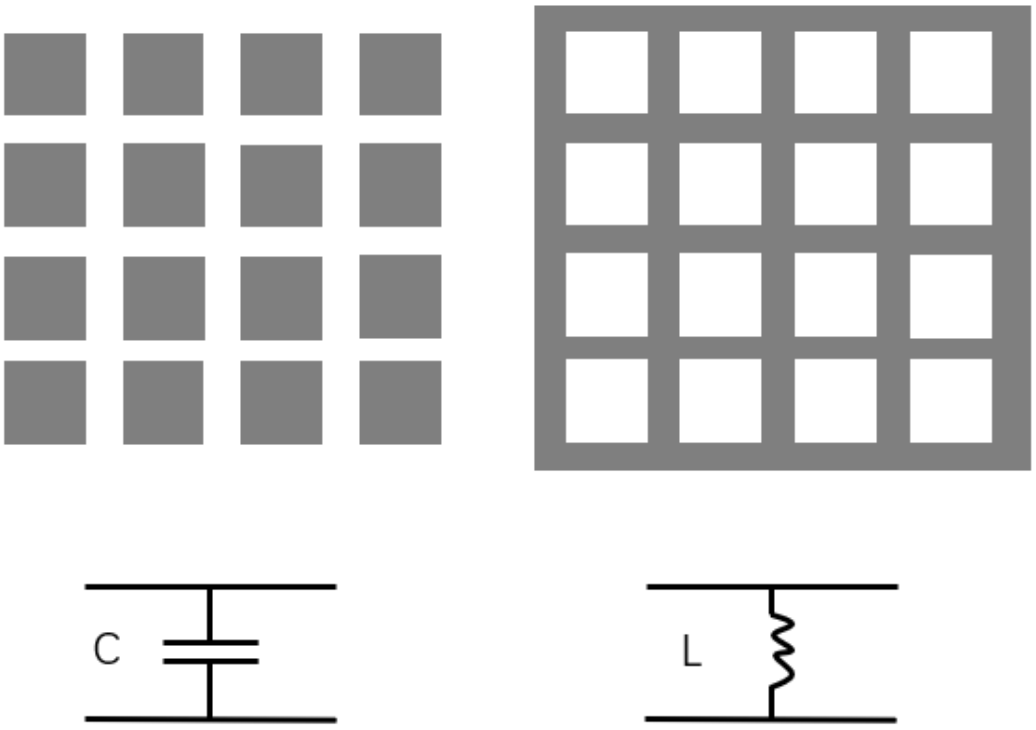

(a) (b)

Fig. 2.1 FSS in patch or aperture structure, (a) capacitive patch array, (b) inductive mesh array

2.2.1.1 Negative permittivity (Double negative property)

Negative permittivity and permeability are one of the most important characteristics of metamaterials. In electromagnetic radiation, the electric and magnetic component are independent essentially. In MRI systems, the electric field will influence the SAR, and the magnetic is responses to SNR in MRI systems. [50] Therefore, the value of permittivity and permeability of the metamaterial are depended on the role it plays in the MRI system. Pendry proposed a dielectric media model: arranging periodic metallic wires in a periodic array, which could achieve negative permittivity. Permittivity of metallic wire array could be written as:

$$\varepsilon_{eff} = 1 - \frac{w_p^2 - w_0^2}{w^2 - w_0^2 + iw\Gamma} \qquad (2.1)$$

Where w_p is plasma frequency, Γ is loss parameter, w_0 is the resonant frequency, depending on the geometry parameter of material. Permittivity of metallic wire array could be negative. When $w_0<w<w_p$, the permittivity of the metallic wires array is negative.

2.2.1.2 Negative permeability

In order to achieve negative permeability, the most common structure used is split-rings resonator (SRRs). [51]

The permeability of this structure could be calculated by:

$$\mu_{eff} = \frac{B_{eff}}{\mu_0 H_{eff}} = 1 - \frac{\pi r^2/a^2}{1 + i2\rho(\mu_0 wr)} \qquad (2.2)$$

According to this formula, it is clear that the μ_{eff} is less than one, but still greater than zero. In order to make μ_{eff} less than zero, it is necessary to add capacitors in this closed inductive circuit to cause resonance. Thus, Pendry designed split-rings resonator to achieve negative permeability. [52]

SRRs consists of two concentric metallic rings when an external magnetic field is perpendicular to SRRs, there will be current induced on SRRs, so creating inductance and the top view is shown in Fig. 2.2. Then, capacitance generated by the gap on each ring. Consequently, LC resonance corresponds to the dimension and shape of SRRs is generated. The reason why cut gaps on both the outer circle and the inner circle is to achieve resonance at the frequency is much greater than the wavelength of the dimension of SRRs. In addition, the gap on inner and outer ring respectively has the opposite direction could increase the capacitance and reduce resonant frequency.

Then, the permeability of periodic SRRs array could be calculated by:

$$\mu = 1 - \frac{fw^2}{w^2 - w0^2 + i\gamma w} \quad (2.3)$$

Where f could be calculated by $f = \frac{\pi r^2}{a^2}$ which is the rate of the area of SRRs over the unit cell, f could define the frequency bandwidth, γ is loss parameter, a is the area of unit cell. It's clear that when $w_0 < w < w_m$, μ_{eff} could have a negative value.

Capacitively-loaded metallic rings (CLRs) is one of the types of metamaterial lenses. CLRs created by adding lumped capacitor into the gap in SRR, [53] and this capacitor is non-magnetic for MRI. The top view of CLRs is shown in Fig. 2.2. Adding this capacitor is an efficient way to miniaturize the dimension of the metasurface in periodic structure. CLRs with negative permeability can focus the RF magnetic field, CLRs with zero permeability can reject the RF flux and CLRs with high permeability worked as RF flux guide.

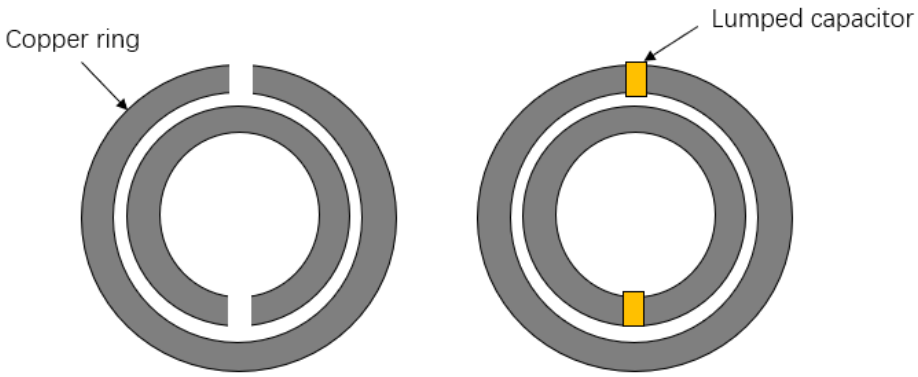

(a) (b)

Fig. 2.2 Negative permeability metamaterials. (a)split-rings resonator, (b)capacitively-loaded rings

In the research[54], the structure of metamaterial lens was CLRs constructed into three-dimensional cuboid, and it was placed between phantom and coils to enhance the axial magnetic field intensity in the near-field region of RF coils to increase SNR. This paper pointed out for near-field application both of electrostatic or magneto static limits still applied, thus double negative parameters were unnecessary. Final metamaterial lens design was arranged into 6x6 array, each unit cell connected by a 33pF capacitor, and

the total size was 57mmx57mmx10.5mm. This structure showed negative permeability around 290MHz to 300MHz. After placing the lens 3mm away from RF coil, there were about 5A/m and 4dB enhancement in cross-sectional h-field and S21 at 298MHz for 7T MRI separately. This 3D structure and the position of elements were shown in Fig. 2.3.

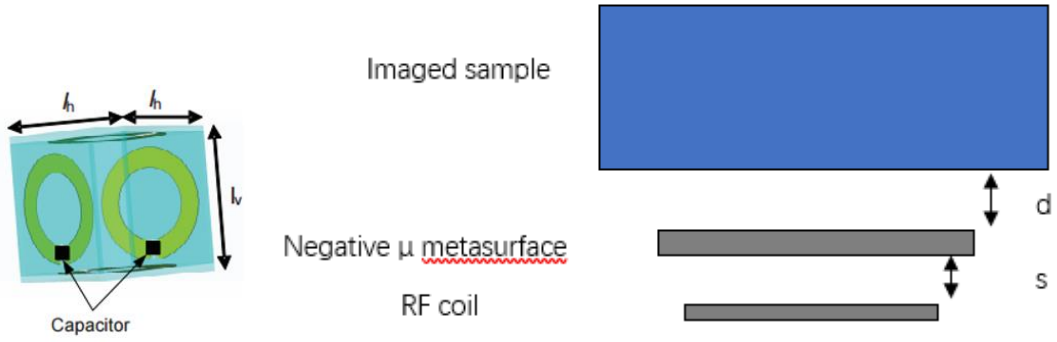

(a) (b)

Fig. 2.3 Metamaterial lens. (a)unit cell in 3-D dimensional. (b)cross section

The paper published by Manuel in 2009 proposed a CLRs structure could improve both of B_1^- field and SNR in 1.5T MRI system. [55][56] The metasurface in three-dimensional cuboid CLRs was placed after the imaged phantom, and there is another reflector made by a 2D array of CLRs which constitutes a high permeability layer. This paper indicated CLRs could provide more improvement in long-distance transmission. When the distance between coil and lens less than 1cm, the improvement in SNR would drop dramatically after 2cm. When the distance between coil and lens greater than 6cm, the improvement in SNR would keep higher than the model in absent of lens. However, the sensitivity of the surface coil would decay within distance increasing. In order to reduce this decay, this research backing the lens with another metamaterial slab to become a 'magnetic wall' which was a medium with a large value of permeability to work as a reflector. In this case, the configuration of a lens and another metamaterial slab was moved from between coil and imaging object to the back of the object. The results showed the SNR could be enhanced by 22% by placing this reflector behind of imaging object. This structure was similar to HIS which have an in-phase reflection, so the magnetic field in the region of interest could be increased.

Another typical metasurface structure consists of CLRs is the magneto-inductive lens (MI lens), which consists of a pair of inductively-coupled parallel arrays of CLRs. From the research[57], MI lens was used to change the noise correlation coefficient from positive to negative. In this paper, the coplanar configuration of CLRs was placed between the coil and phantom to provide negative noise correlation and negative mutual inductance. Noise correlations defined by electric coupling between elements, and it between two coils in the array was described as a reaction in the tissue between the electric field and eddy current responses to the electric field generated by another coil. From the formula 2.4:

$$\mathrm{SNR} = \frac{\sqrt{\frac{p_1^2}{R_{11}} + \frac{p_2^2}{R_{22}} - \frac{k_e^2}{R_{12}} p_1\ p_2^* - \frac{k_e^2}{R_{12}} p_1^* p_2}}{1 - k_e^2} \qquad (2.4)$$

Where $k_e = \frac{R_{12}}{\sqrt{R_{11} R_{22}}}$ is the electrical coupling coefficient, which defines the electric analog of the magnetic coupling in magnetically coupled circuits. [58] It was clear that the SNR will be increased when R_{12} becomes negative. In further, the negative values of noise correlation will improve g-factor in coil arrays. G-factor is geometry factor due to the noise propagation and depends on encoding capability of receiving coil. In the latest paper published by the same author, this MI lens could improve the SNR by 130% at the phantom surface, and the improved penetration depth was 40mm in 3T MRI system.

In [59], both μ=-1 lens and MI lens were used to increase the image acceleration in parallel Magnetic Resonance imaging (pMRI). The SNR in accelerated images after imaging reconstruction (SNRacc) and the SNR of the full acquisition would be reduced by the reduction in acceleration factor R and coil geometry g-factor. The relationship between them could be described by:

$$\frac{SNR_{full}}{SNR_{acce}} = g\sqrt{R} \qquad (2.5)$$

From the results, the operation frequency of the MI lens was depended on the frequency between the resonant frequencies of two CLRs plane, this property was similar to negative permittivity structure. Then, μ=-1 lens provides 3D isotropy with cubic lattice form; the MI lens was anisotropic because it only interacts with the field perpendicular to the structure. In MRI system, this anisotropic property could be ignored, because the mainly axial B1 field provided by MR coil is perpendicular to the lens. After testing, MI lens could give better SNR because of lower ohmic losses due to less unnecessary rings used.

The key mechanism for focusing with a metamaterial lens is the amplification inside the lens of these evanescent harmonics by means of the excitation of surface waves in the slab, so that lens transfer harmonics to the other side of the lens. The other important property of CLRs is localise the field of view (FOV) of MRI coil. This can be explained by the main lobe of the magnetic field produced by a coil is represented by low spatial harmonics; side lobes are represented by high spatial harmonics. Metamaterial lens can transfer harmonics constitute the main lobe of the magnetic field of coil but not side lobe. Thus, MI lens localize the FOV of the coil and remove the main source of noise correlation between adjacent coils response to the side lobes.

2.2.1.3 Metamaterial as radio frequency flux guide

The RF magnetic flux density from regions of interest (ROI) was transmitted or received by the RF coil or array coils in the MRI systems. Therefore, RF flux guides can be used to guide the magnetic flux from the ROI to the RF coil, so that optimizing this procedure. [60] The Swiss roll manufactured by wounding insulated metallic sheet around a cylinder shown in Fig. 2.4(a). The swiss roll device is characterized by a magnetic field guide [61], which is used to focuses the magnetic field by its negative

permeability. The capacitance of the swiss roll device is controlled by the permittivity and thickness of dielectric, and the inductance is determined by the number of conductor layers. Then, the resonant frequency of the Swiss roll can be calculated by equation 2.6:

$$\omega_0 = \sqrt{\frac{d_s}{2\pi^2 \varepsilon r_s^3 (N_s - 1)}} \qquad (2.6)$$

Where d_s is the insulator thickness between conducting sheets, N_s is the number of turns with a radius of r_s. In [60], the Swiss roll device was used to guide the RF flux from an object to a remote receiver coil with little flux leakage and distortion, when the 200mm Swiss roll was placed vertically between the imaged object and the RF coil. The μ was the peak value in the real part at the resonant frequency 21.3MHz, and the S21 at resonant frequency got obvious improvement. This result proves the Swill roll acts as a flux guiding medium. In [62], the μ of the Swiss roll was set as 35 at 21.3MHz to transfer an input magnetic field pattern to the output face without loss of intensity and with a spatial resolution equal to the roll diameter in 0.5T MRI system. From the measurement results, this device behaves as a near-field imaging equipment consisting of an array of magnetic wires. The cross section of this system shown in Fig. 2.4(b).

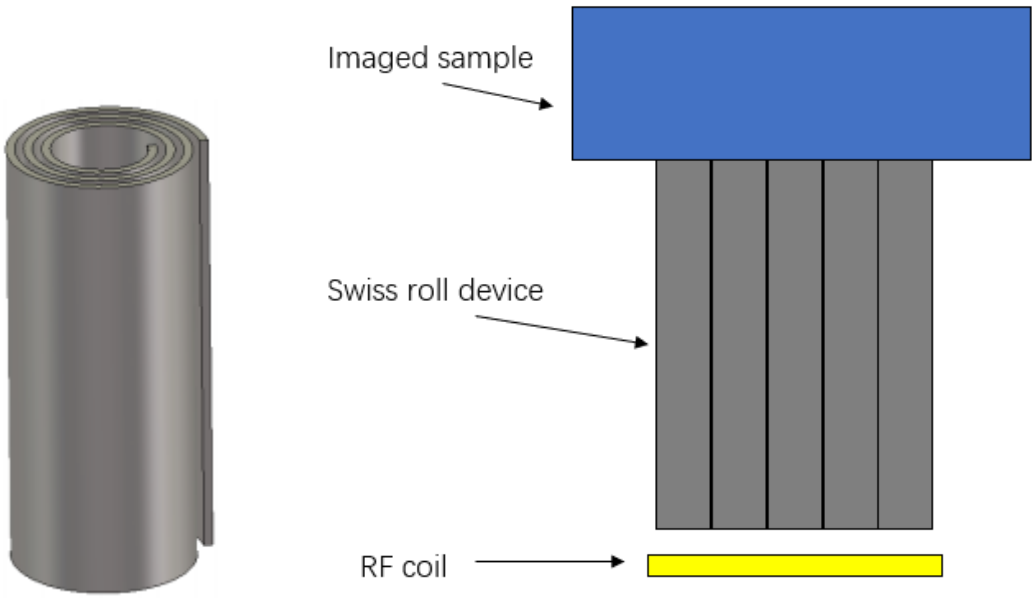

Fig. 2.4 Metamaterial in Swiss roll. (a)unit cell in 3-D dimensional. (b)cross section

The Swiss roll metamaterial device can be transferred to the wire medium, and each cylinder becomes metal wire. This changing makes the equivalent capacitance of the whole device be decreased, and the resonant frequency of the device will be increase with the same dimension. Thus, this structure could be used in a higher field strength MRI system. There is no obvious increment in SNR, because the main target of this research is to transfer magnetic field without any spreading, due to the concept of the magnetic ‘wire’. However, the real material still has losses, and they allowed the image to spread and reduce the resolution. The similar design of wire medium was pointed out in [63], the wire medium was used to transfer the EM fields in MRI system and increase the transmission coefficient at the resonant frequency of the device.

2.2.1.4 High impedance surface (HIS)

The other important property of metamaterial is high impedance surface (HIS). The structure of HIS usually consists of one top patch, one substrate and one ground plane. This property was investigated by Sievenpiper in [64], by the structure of the Artificial

Magnetic Conductor (AMC). AMC is in periodic structure consisting of lots of unit cells, and has very high impedance at its resonant frequency. HIS is usually designed by the FSS in patch array grounded by PEC. The across-section and equivalent circuitry were shown in Fig. 2.5. The top patch was inductive and the gap between each patch was capacitive.

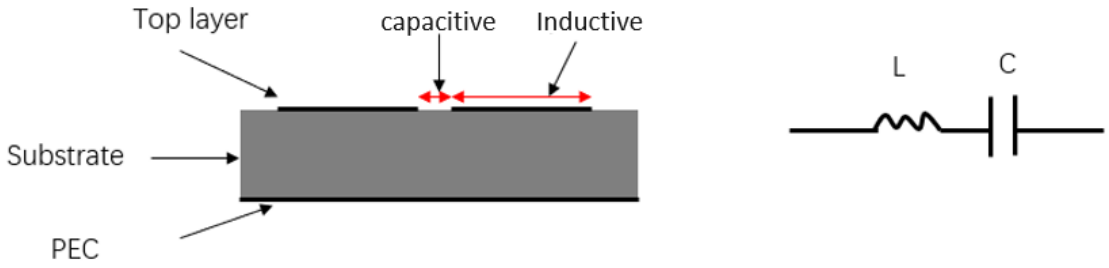

(a) (b)

Fig. 2.5 (a) Cross section of HIS. (b) Equivalent circuit for HIS without via

The impedance of each structure could be given by:

$$Z = \frac{XC \times XL}{XC + XL} \qquad (2.7)$$

$$Z = \frac{jwc}{1 - w^2 LC} \qquad (2.8)$$

It should be noticed that, in both part:

When $w^2LC > 1$, impedance became negative and capacitive.

When $w^2LC < 1$, impedance became positive and inductive.

When $w^2LC = 1$, impedance became infinite for with via part, and became zero for no via part.

These rules could also be described by Fig. 2.6:

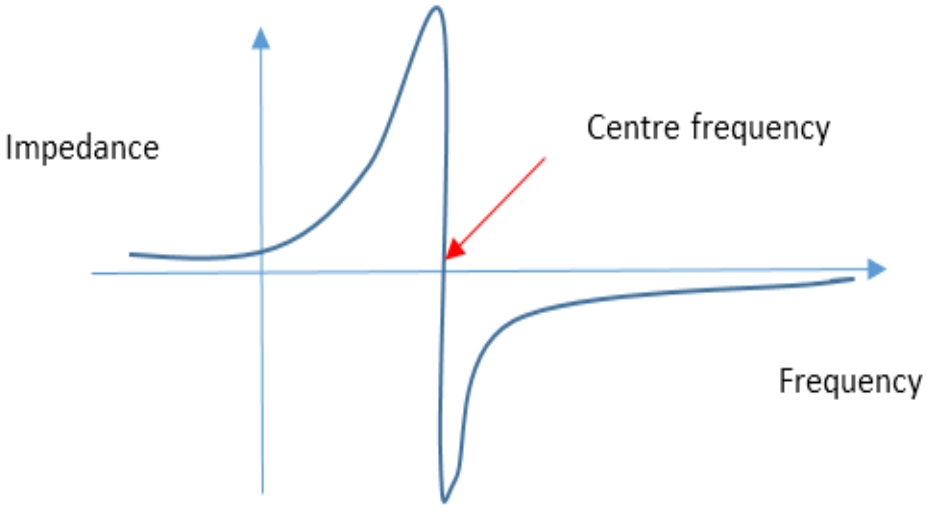

Fig. 2.6 Impedance of HIS along frequency range

Then, the incident plane wave will be reflected by the phase of 180° when the perfect electric conductor (PEC) is present, and reflected by the phase of 0° when the perfect magnetic conductor (PMC) is present. PMC does not exist in nature, but its properties can be achieved using HIS at the resonant frequency.[65] Fig. 2.7 gives the incident wave is reflected by the PEC or HIS respectively. HIS reflects the incident wave in-phase instead of out-of-phase. Therefore, the destructive interference from the reflected wave to the incident wave can be altered into constructive interference, and the field will be improved. The property of zero-degree reflection at the resonant frequency of the HIS can also be studied in the Fig. 2.8.

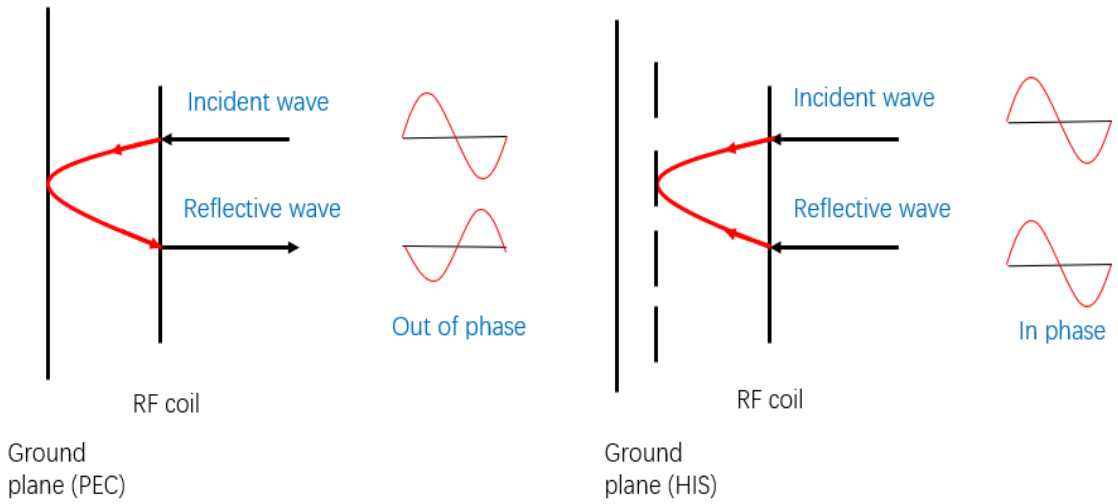

(a) (b)

Fig. 2.7 The reflective character of field source. (a)out-phase reflected field with PEC (b)in-phase reflected field with HIS

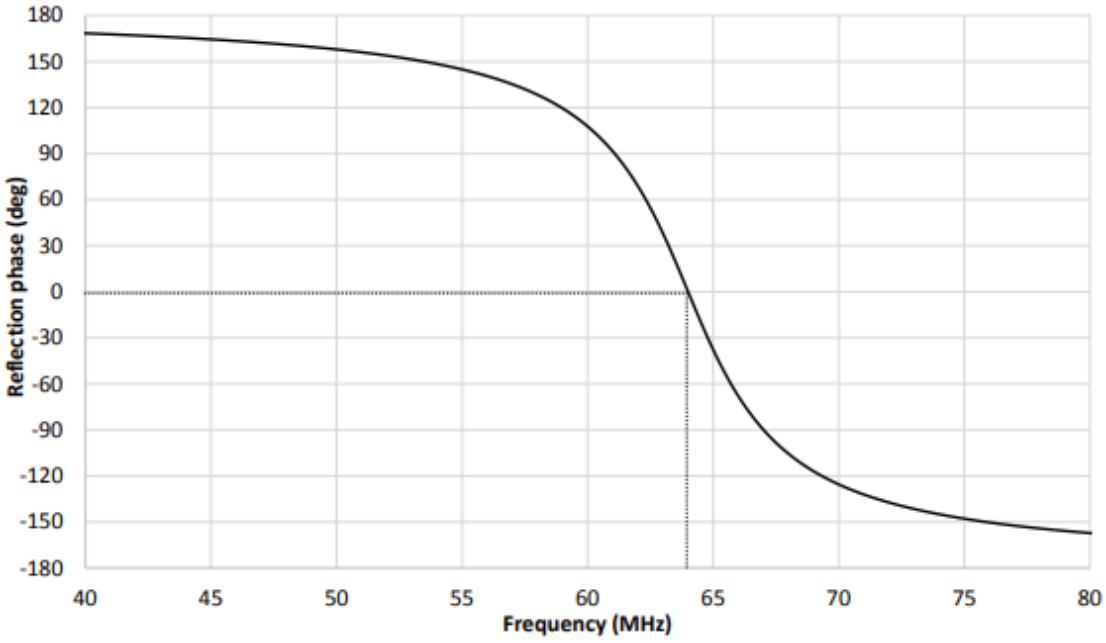

Fig. 2.8 The numerical reflection phase of the HIS

High impedance property could also be used in MRI system. RF coil was always placed inside of RF shield. RF shield was an important part which shields the resonators from other conducting objects. For instances, when the RF field created by RF pulse will cause serious interference in MR signal receiving, the receiver may recognize the RF

signal as MR signal to receive and encode. As a result, it was necessary to shield RF signal from RF coil, and a good shield system will make large benefits in the entire MRI system. There were some researchers have shown the HIS organized by metamaterial usually has better performance than the PEC shield plane, when they work as a ground plane or shield plane in MRI systems. In [66], one HIS was established by an arrangement of capacitive unit cells and placed parallel to the PEC ground plane. The placement of each component shown in Fig. 2.9. In this case, HIS was built to work as PMC (perfect magnetic conductor), which has 0° reflection phase. The resonant frequency of unit cells was tuned to 63.85MHz, and the dimension of unit cells was miniaturized by adding lumped elements between each unit cell. The magnetic field was improved by 42% compared with the RF coil only case. In [67], the relationship between the dimension of entire HIS and enhancement in the magnetic field was investigated. This paper showed the improvement in magnetic field increases with HIS area. The HIS to a capacitive layer firstly, then the required capacitive layer was created by designing unit cells arrangement. This method was quite useful to simplify the simulation procedure, and would be used in this research. The metal sheet works as the reflector to shield RF signal is usually manufactured by copper, iron or another benign conductor in the MRI system, due to the weak penetration of RF magnetic field in high permeability media. However, this normal metal could not remain its good shielding performance in high field strength, and the signal wave reflected by shield plane is out-of-phase, and cause destructive effects on RF signal transmitted by the coil. In the simulation, the shield plane of MRI system always chose by PEC (perfect electric conductor), which has infinite permeability and 180° reflection phase for an incident plane wave. From the results, the magnetic field inside of the dielectric phantom was increased 18%-32% depending on the different size of HIS, compared to the RF coil only case.

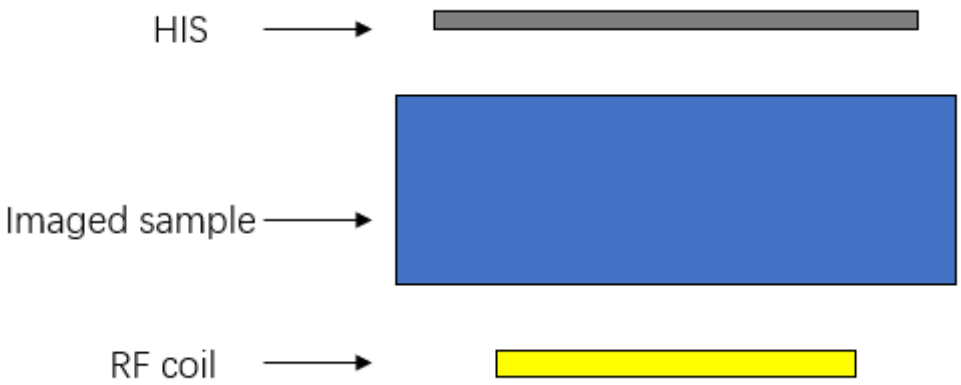

Fig. 2.9 The application of HIS in MRI system

The other HIS structure is defined electromagnetic band gap (EBG), which has a via connecting top patch and ground plane. This structure miniaturizes the dimension of the unit cell, so the period of EBG unit cell is much smaller than its wavelength. [68] The gap between each top patch becomes capacitive, because charges assemble at the edge of the patch, and voltage will be created in the gap. Then, current flow through the top patch and via to ground plane, so they will be inductive. Finally, one of the unit cells of HIS could be described by an equivalent parallel LC circuit in Fig. 2.10.

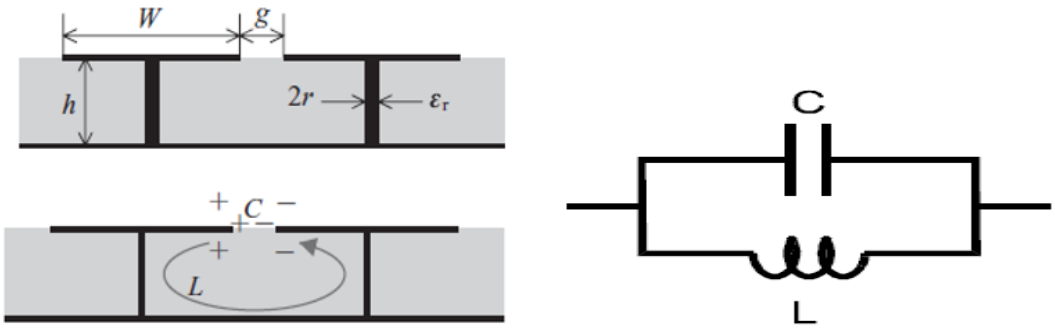

(a) (b)

Fig. 2.10 (a) Cross-section of EBG. (b) The equivalent circuit for EBG without via

Then, the impedance of the parallel LC circuit can be calculated by:

$$Z = \frac{XC \times XL}{XC + XL} \qquad (2.9)$$

$$Z = \frac{jwc}{1 - w^2 LC} \qquad (2.10)$$

EBG structure could also be used in MRI systems optimization. In the paper published by Gameel Saleh [69], a multilayer four-leaf-clover-shaped EBG structure was presented behind strip line coil operating at 300MHz in 7T MRI systems. The anti-phase currents were suppressed by the EBG in its in-phase band gap reflection coefficient. Thus, magnetic flux density inside the phantom was increased. The magnetic field was increased by 57% by adding this EBG structure. However, the magnetic field was only enhanced in the narrow stop band gap. This research has pointed out for 200MHz, which is beyond the resonant frequency of EBG, the stop band gap would not work, and energy could propagate through EBG to cause extra effects. The other disadvantage of EBG structure was its dimension was much smaller than its wavelength, so it was very hard for EBG to work at low frequency. This constrains limit EBG structure would not be suitable for low field strength MRI system like 1.5T or 3T. The other application of EBG structure was decoupling of elements of MRI body coil array. This approach was published by Tatyna A in 2015 [70]. Two dipole antennas mimicked body coil array in MRI system, and EBG for mutual suppression coupling was placed between two dipole antennas. From the results, the isolation of the matched dipoles was improved by -6dB when two antennas with a separation of 80mm. This research was still completed in 7T MRI system.

2.2.1.5 Hybrid metasurfaces

In the previous section, the negative permittivity of the metamaterial has been discussed, and high permittivity can also be achieved by metamaterial. There were some researchers have discovered that, the SNR and the SAR for different imaging tasks in 3T MRI system can be increased and decreased separately by using high permittivity metamaterial. [71][72] In these cases, the high permittivity pads were used to improve the RF shimming and focus the RF magnetic field to enhance the image homogeneity in MRI systems. In the [73], the dielectric pads with high permittivity increased the SNR by improving the magnetic field. The RF excitation power can be reduced by 50% through adding high permittivity pads, and the SNR was increased up to 40%, and the SAR was reduced by 27%. After that, the dielectric pads with relative permittivity equal can be generated by a mixture of distilled water with Barium Titanate powder.[74] The high permittivity pad can reduce the electric field by 13%, which leads to reducing the SAR by 14% average the entire ROI.

There is a new type of metasurface is published to improve the scanner sensitivity by metallic wires array resonators. In the research published in 2014 [75], the author realized a metasurface as an array of 14x2 wires, and the length of each wire was 25.5cm. The length of wires was obtained by the formula:

$$f = \frac{C}{\sqrt{\varepsilon \cdot L}} \qquad (2.11)$$

Where f is the resonant frequency of wires, c is light speed, ε was the dielectric constant of background media and L is the length of wires. This wires array metasurface was 2D structure. From the results, there was 25% increment achieved in SNR, reduction in the scanning time and improvement in image resolution in 1.5T MRI system.

Another novel hybrid metasurface for MRI applications was shown in [76]. In this case, the metasurface was designed as an array of nonmagnetic metallic wires with high permittivity dielectric blocks at the edges. The SNR and image quality were enhanced

by using this metasurface in 1.5T MRI compared with birdcage body coil only. The other novelty shown in this research is the resonant frequency of the metasurface can be adjusted by changing the effective permittivity of blocks near the edges. This author proposed another compact hybrid metasurface to enhance the SNR in 7T.[77] In this case, the structure of metasurface based on the array consisted of long strips (17.5cm) and 3x3 short strips (3cm). The full structure size was 17.5x17.5x0.9cm³, CaTiO3 substrate had a relative permittivity of 110. After testing, this metasurface enhanced both $B1^+$ and $B1^-$ at 298MHz by 70% compared with no surface, so image SNR was improved by a factor proportional to $B1^-$. The improvement in SNR provided higher imaging resolution and reduced scanning times.

In the MRI system, the magnitude of the RF field inside of the imaged sample will be influenced by many factors, such as electrical properties, imaged position and geometry of the sample. In the [78][79], the dielectric pads were attributed to the interference of a secondary field, which was generated by the induced currents in the pads. Then, the high dielectric constant also decreases the wavelength of the RF field wave. [80] A more recent study in this area was given by authors in [81], the high dielectric constant material with a high permittivity of 1200 was incorporated with an RF volume coil at 7T, to enhance both transmit field B1+ and reception field B1-. From the experiment, the RF transmission power was reduced, and the detection sensitivity was increased.

2.2.2 Summary

This section provided a background literature review for the area of using metamaterial to optimize the MRI system for a single band. From this section, there were three main types of metamaterials indicated to improve the MRI systems. They are negative permeability metamaterial, high impedance surface and high-permittivity dielectric pads. Negative permeability metamaterial has many structures, such as μ=-1 metasurface, magneto inductive lens and Swiss roll device. They have shown good performance to localize the field, enhance the magnetic field or guide flux to improve

the SNR in MRI systems, when the metasurface was placed between the RF coil and the imaged sample. HIS works as a perfect magnetic conductor to reflect the incident wave in in-phase to enhance the SNR when the perfect electric conductor in the shield plane was placed by HIS. Thus, HIS was always placed behind the imaged sample. Dielectric pads were usually used to enhance the SNR by improving the magnetic flux density, and they were used to optimize the volume RF coil in MRI systems, such as birdcage coil, due to the big size.

These were the developments of metamaterials used in single band MRI systems recently. All of them shown a good performance to optimize the MRI systems, especially in high field strength. However, there were some limitations and disadvantages from these designs, and would be solved in this project.

1. All the metamaterials used in MRI optimization are based on the periodic structure, which brings some inconvenience in the practical applications. Firstly, the resonant frequency of the periodic metamaterial is most depended on its dimension. Therefore, the large size of the structure will be a difficult problem. Adding lumped elements was one of the most popular methods people used to miniaturize the size of metamaterials, such as CLRs, but the extra power losses in lumped elements and noise caused by the coupling between lumped elements and RF elements will be traded off. Secondly, most of these designs were used in high field strength MRI system, because the higher field strength MRI systems will require higher resonant frequency, and the stresses in the dimension of the periodic structure can be relieved. Thirdly, it has been shown in some researches, the periodic structure will also make the RF field become periodic, so the susceptivity of the RF coil will be decreased, and there might be some distortion in the images sometimes.

2. Although most of these designs provided considerable improvement in SNR at the surface of the imaged sample, the SNR of within metamaterials had high decay speed. The enhanced SNR will only last a short penetration depth, which was always less than 35mm. It was not favorable for MRI applications, because the enhanced penetration depth should be as long as possible to solve different imaging tasks.

2.3. Multi-nuclei imaging

Within the development of MRI systems, hydrogen has been unable to meet the imaging needs of some body parts, so there is an increasing numbering of nuclei are used to imaging human tissue in MRI. However, if there is more than one nucleus required to be imaged from one patient, it will be expensive and wasting time by imaging nuclei one by one. Therefore, multi-nuclei imaging is a necessary difficulty needed to be overcome in the development of MRI systems.

2.3.1 Literature review of the multi-nuclei MRI systems.

2.3.1.1 Dual-band volume coil in coupled-resonator model

For example, Lingzhi HU [82] pointed out coupled-resonator model was a way to build dual band RF coil. The matching work for multiple RF coils model is a critical challenge, because different resonant frequency required different matching impedance. In this research, there was a secondary inductor and capacitor (LC) resonator with a coupling capacitor (matching capacitor) in series to both ^{19}F and ^{1}H volume coils in 4.7T MRI systems. Impedance matching at both frequencies is achieved by incorporating suitable a number of variable capacitors, which shown in Fig. 2.11. This birdcage coil based on the coupled resonator approach also shown the B_1 field was homogeneity at both resonant frequencies, so the susceptibility effect on the image will be minimized. Then, because the size of the inductor on the additional resonator was much smaller than the RF coil and placed on the distant of the coil, the uncontrolled mutual inductive coupling between two resonators can be decreased, and the effects from the coupling to the quality factor Q can be reduced too. However, the method of using the coupled resonator model to manufacture a dual-frequency MR coil is only suitable for two close resonant frequency. For big separate frequencies, the frequency-dependent inductance of the RF coil will be very different at two resonant frequencies, and it was hard to

implement loop inductor has such different frequency-dependent inductance as the sample coil. As a result, the equivalent circuitry and secondary resonator will be hindered. From this research, a dual band RF volume coil base on coupled resonator model was proposed to image ^{19}F and ^{1}H at 188MHz and 200MHz in 4.7T MRI system respectively, with good homogeneous B_1 field. However, the entire performance was not as expected. The SNR was lost from 50% in ^{1}H imaging, and 25% in ^{19}F imaging compared with the single-band RF coil. Furthermore, although this RF coil structure could be used for both ^{19}F and ^{1}H imaging, these two nuclei required to be imaged in separate imaging tasks.

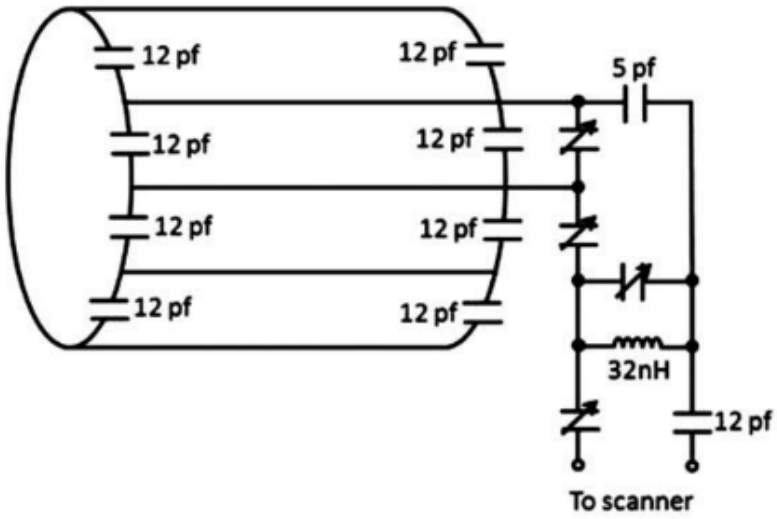

Fig. 2.11 Diagram schematic of Dual-band volume coil in coupled resonator model

2.3.1.2 Dual-band surface coil with trap circuitry

Another example was based on dual-band surface coil optimization. [83] In this case, the dual-band imaging was achieved by combining two RF loops together. The frequency bands focused were 170.267MHz for H1 and 45MHz in 4T MRI of rat brain. The biggest problem of this composite structure was the coupling between the two coils. Coupling was not only existed between coils, but also existed between electrical components, such as tuning capacitors and matching capacitors. Coupling influenced

the entire RF performance and produced frequency shifts in both RF loops. Thus, coupling was a tricky case need to be considered during using the multi-coil combination. In this case, the trap circuit (LC circuit) was inserted in the smaller coil to eliminate mutual coupling between two loops. Fig. 2.12 shown the double-tuned RF coil prototype [83], which consisting of two square RF loop and a trap circuit. Although trap circuit showed a good performance to solve the coupling in this co-planar and small structure, there were extra signal losses in the trap inductance, which reduced the RF homogeneity and sensitivity of Na channel by 28%.

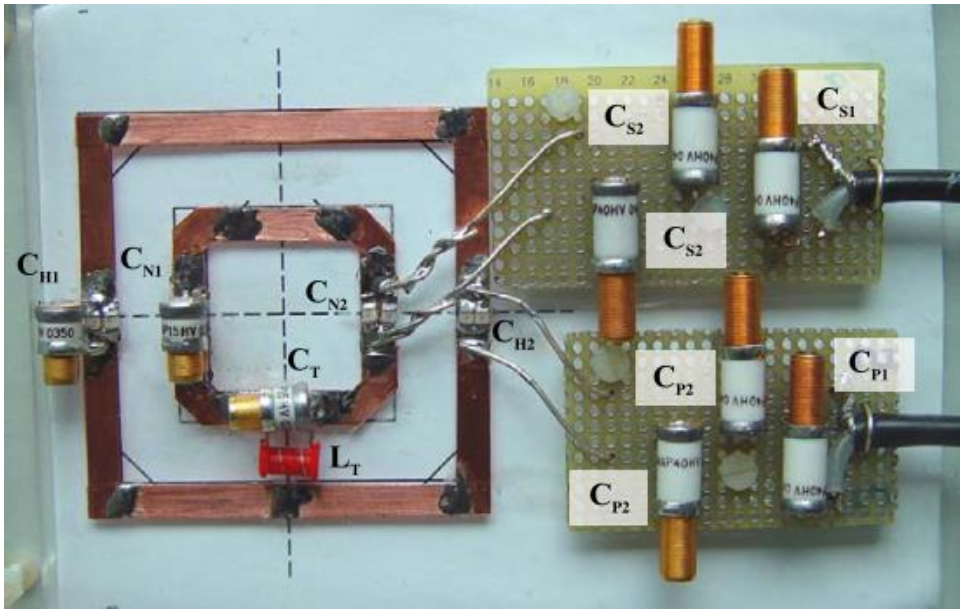

Fig. 2.12 Photo of dual band surface coil with trap circuitry [83]

2.3.1.3 Multi-nuclei MRI with (micro-electromechanical systems) MEMs switches and PIN diode

There was a research that showed positive results for small frequency difference nuclei imaging in low field strength MRI systems. [84] In this session, both of MEMS switches and PIN diodes were considered to design switched dual tuned RF volume coils to image ^{19}F and ^{1}H in 1.5T MRI system. The frequency bands focused in this case were 60.08MHz for ^{19}F imaging, and 63.85MHz for ^{1}H imaging. This session based on

designing a dual band coil to allow detection of inhaled $^{19}F^{3}C^{8}F$ and ^{1}H signals from the lungs in the same scan case. The MEMS method used an array of beam-type structures worked as relays actuated by the DC voltage between beam and gate. The beams make contact with a central conductor to provide a connection between RF one and RF two, and actuate the switch. The representative side view of the MEMS structure is shown in Fig. 2.13 From the measurement results, there was no measurable difference in the power loss comes from the MEMS or PIN diode switching, compared with the well-tuned coil. There was a 4.5% difference in the mean transmit efficiency measured between MEMS, PIN diode switching and coil only. Both of MEMS and PIN diode switches could only image one RF nuclei at one time, so the results should be overlaid after finishing both ^{1}H and ^{19}F imaging.

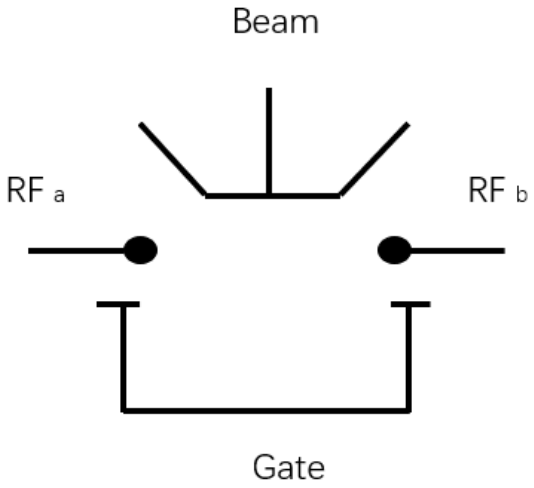

Figure 2.13 Circuit schematic of MEMS switches

2.3.1.4 Metamaterials in multi-nuclei imaging

There is one research shown the application of metamaterials in multi-nuclei imaging. In this paper,[85] one novel dual-nuclei RF coil inspired by wire metamaterial structures was proposed. The coil does not require tuning or matching, because the resonant frequency was totally dominated by the metamaterial in periodic arrays. The excitation was provided by an external non-resonant circular loop feed connected to a single coax cable. This coil was placed on two mutual orthogonal periodic structures

comprising several coupled thin metal strips. These two-wire metamaterial-inspired resonators are referred to as the long-wire resonator (with strips parallel to z-direction which along B_0 field), and short-wire resonator (with transverse strips respect to B_0 field). The whole RF transceiver system was shown in Fig. 2.14. The wire length of the long-wire resonator and short-wire resonator were 434mm and 72mm respectively, and resonated at 300.1MHz and 282.6MHz for ^{1}H and ^{19}F nuclei imaging in 7.05T. The adjacent strips of the short-wire resonator connected by copper patches; this is also a way to miniaturize the dimension of the periodic structure. This capacitive load caused extra input impedance and intrinsic noise. It should be noticed that, the overlap between two periodic structures will create inductive coupling, and cause distortion during imaging in both frequency band. Although both nucleus can be imaged simultaneously in this case, the SNR result of each nuclei is worse than the well-tuned coil. In addition, this report indicated the decays of SNR are different in different nuclei imaging. For instance, the SNR decays with the depth in the phantom for ^{1}H much faster than ^{19}F. Adjusting the positions with respect to a common small loop could be used to match impedance.

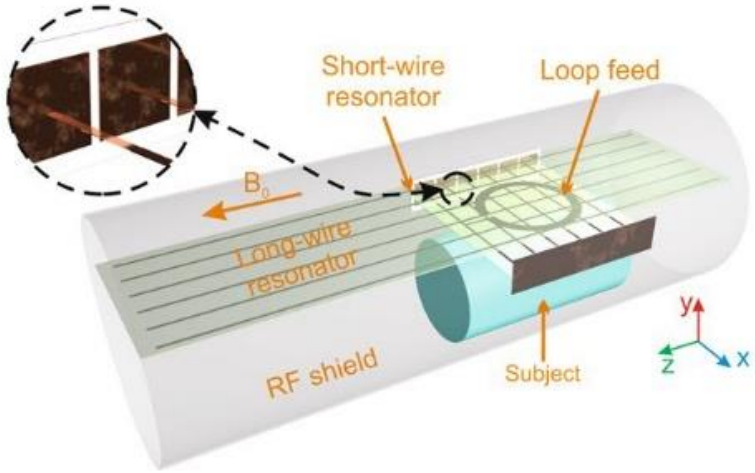

Fig. 2.14 The MRI transceiver system with two periodic metasurface

2.3.2 Summary

In this section, some methods used to achieve dual band nuclei imaging were introduced. They were based on changing coil structure, adding extra lumped elements and circuitry, or switch devices. However, most of them did not show a good RF performance compared with the well-tuned coil at the resonant frequency, even decreasing the SNR up to 50%. For example, the extra power loss from the additional lumped elements, extra noises from the mutual coupling between the RF coil and additional circuitry or device.

Then, from the rare researches achieved multi-nuclei imaging by using metamaterials. The multi-nuclei imaging was achieved by using single RF fed, but the dimension of the periodic structure in the specified field strength was an issue. From the research [60], the length of the long-wire resonator was even three times longer than the imaged sample, which is quite inconvenient in practical MRI imaging and hard to be applied in low field strength MRI system. Then, the mutual coupling between two resonant structure caused extra noise to influence the susceptivity of the RF coil, so obtained unsatisfactory SNR results. The B_1^- homogenous field become periodic, and the susceptivity of the RF coil was decreased.

In this thesis, one metasurface in non-periodic structure will be proposed to image ^{19}F and ^{1}H in 1.5T MRI by a single RF fed. The gap and improvement of this project to previous researches can be defined as:

1. The RF coil used in this case was dual-loop single fed coil. There was no mutual coupling between two loops, because there was a single RF fed at the outer coil. Thus, there is no trap circuit required to decoupling two loops, and avoid the power loss from the additional lumped elements.

2. The metasurface was in non-periodic structure, the dimension of the metasurface only controls the equivalent capacitance. Therefore, the dimension of the metasurface used in this case was very flexible and small (103mm x103 mm), which was low costs and easy to be used in practical MRI.

3. From the measurement results, the non-periodic structure can image both ^{19}F and ^{1}H

simultaneously with a single RF fed in 1.5T MRI system. The RF performance at each resonant frequency will not be reduced, and get obvious improvement. The uniformity of the field was not influenced by the non-periodic metasurface, because the metasurface used in this case only had one unit cell, so the surface current will not flow in the gap between each unit cell in periodic metasurface, and the uniform B_1^- field can be preserved.

Chapter 3

A non-periodic Metasurface for 1.5 T MRI applications

3.1 Introduction

The working efficiency and image quality of a magnetic resonance imaging (MRI) system are measured by signal to noise ratio (SNR) which is characterized by magnetic flux density B_1. Improving the radio frequency (RF) magnetic field is the most efficient method to increase SNR without the need to change coil type, or increase the intensity of static electromagnetic field. Recently, researchers have gradually discovered the potential of some metamaterials in optimizing MRI systems, such as magneto inductive lens, high impedance surface or resonator arrays. These designs are all in periodic structure, which has a large number of unit cells and fixed dimensions according to the resonant frequency. Most of the existing metamaterials have very limited penetration depth, as indicated in [86]. The reason is that, the periodic structure is always based on larger dimension (usually 3 times than the RF transceiver coil used in that case). Then, the lumped elements used to miniaturize or tune the periodic structure cause extra

energy losses, such as capacitively loaded rings (CLRs). Therefore, the enhancement in SNR by these designs is usually achieved for the surface of an imaged object, and the enhancement will reduce very fast inside the object and cover limited penetration depth (usually less than 25 mm). On the other hand, most of these optimization work is based on high field strength, such as 4T or 7T MRI systems. High field strength MRI systems can achieve high imaging speed and good imaging quality as they directly increase the strength of static magnetic field. However, high field strength is not suitable for imaging some sensitive organs, such as brains. As a result, 75% of the existing clinic MRI scanners adopt the field strength of 1.5T.

This chapter will introduce a non-periodic structure metasurface consisting of a single capacitive layer to enhance the magnetic flux density at the resonant frequency of 63.85MHz for 1.5T MRI. The proposed metasurface was simulated in CST Microwave Studio, and then tested in an RF bench. The magnetic field was measured within a dielectric phantom with various design parameters. The initial dimension and capacitance of the metasurface were obtained from the introduction by using the surface impedance method. The metasurface significantly improved the flux density B_1 inside the dielectric phantom, which further improved the SNR for 1.5T MRI systems. The specified absorption rate (SAR) describing the energy absorbed by human tissues was not increased, because the non-periodic structure did not enhance the B_1 by focusing the field as most periodic structure did. This property is a significant achievement in the MRI optimization work, as it improves the MRI system without increasing the risks in human health. Furthermore, the enhancement provided by the metasurface covers the whole penetration depth.

All the simulation work was done in CST Microwave Studio, and the simulation results are discussed in Section 3.5. The magnetic flux density (B_1), electric field (E-field) and specific absorption rate (SAR) were monitored and measured by the monitoring tool in the CST. The most suitable design of metasurface from the simulation was manufactured. Then, RF surface coils and the metasurface were tested in an RF bench, in order to examine the transmission performance of the RF surface coils by Q-factor.

In the RF bench, the RF coils were matched with a dielectric phantom full of saline, and tuned to 63.85MHz either with the metasurface being present or not. The experimental results from the bench are shown in Section 3.6. Next, the RF coils were matched with a new dielectric phantom full of copper sulphate solution, whose electromagnetic parameters were more correlated to human body. Finally, the proposed system in the RF laboratory was tested by a 1.5T MRI scanner, and the testing results are analysed in Section 3.7.

3.2 MRI configuration

The simulation was conducted in CST Microwave Studio, a commercial and full-field software package with finite integral (FI) technique. The simulation used the frequency domain solver. For all simulations, both manual and adaptive meshing techniques were adopted to ensure the convergence of the solution. The RF surface coil was fed by a 1 W signal source with a frequency of 63.85 MHz. Fig. 3.1 gives the CST simulation geometry including an RF coil, a metasurface and a dielectric phantom.

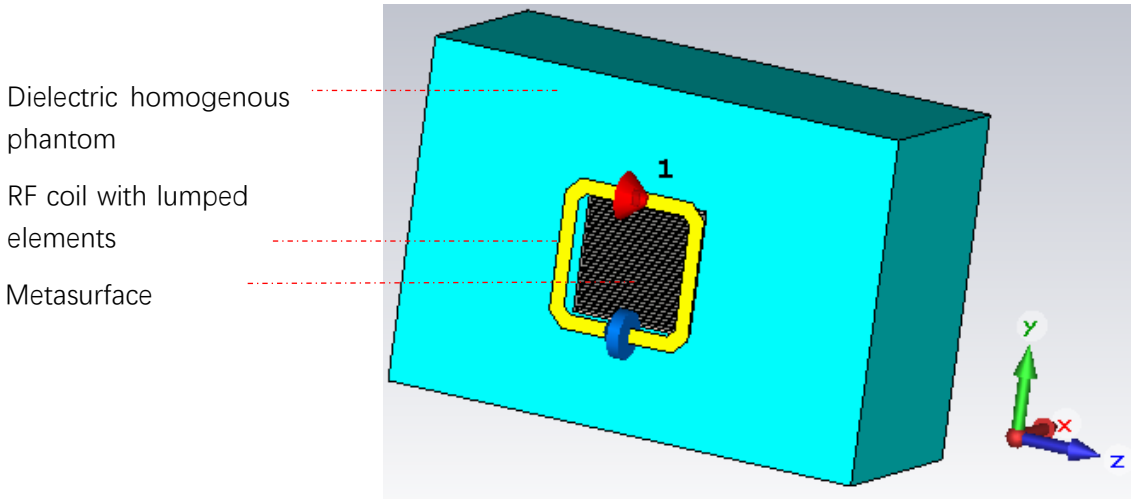

Fig. 3.1 CST simulation geometry

Fig. 3.2(a) and Fig. 3.2(b) give the cross section of the MRI model used in simulation

with the metasurface being absent and present, respectively. The parameters of the homogenous dielectric phantom were set as dimension of $x \times y \times z$ =14 cm×23 cm×33.5 cm, ε_r= 65, σ= 0.4 S/m and density of 1 kg/m³ to simulate a human body is. In the coordinates system, the RF coil was centred at the origin (x=0, y=0 and z=0). The coordinates of the dielectric phantom were obtained as follows, x-axis of 25-165 mm, y-axis of -112.5-112.5 mm, and z-axis of -167.5-167.5 mm. The space between the dielectric phantom and capacitive impedance surface (CIS) was set as S. The distance between RF coil and CIS was set as D. When the capacitive layer was absent, the distance between RF coil and dielectric phantom was set as H, the sum of D and S. In addition, a receiving probe was placed 10 mm inside the dielectric phantom to measure the transmission coefficient S_{21}. The thickness of the receiving probe was set to be electrically small, and it would be removed for other tests except S_{21} measurement, in order to avoid the any electromagnetic effect on the probe. Further, two red dash lines were drawn, i.e. the measure line along x-axis to measure the tested parameter such as magnetic field across the dielectric phantom respectively (x=25-165 mm, y=z=0 mm), and the measure line along y-axis to measure the tested parameter along the dielectric phantom surface (y=-100-100 mm, x=25 mm, z=0).

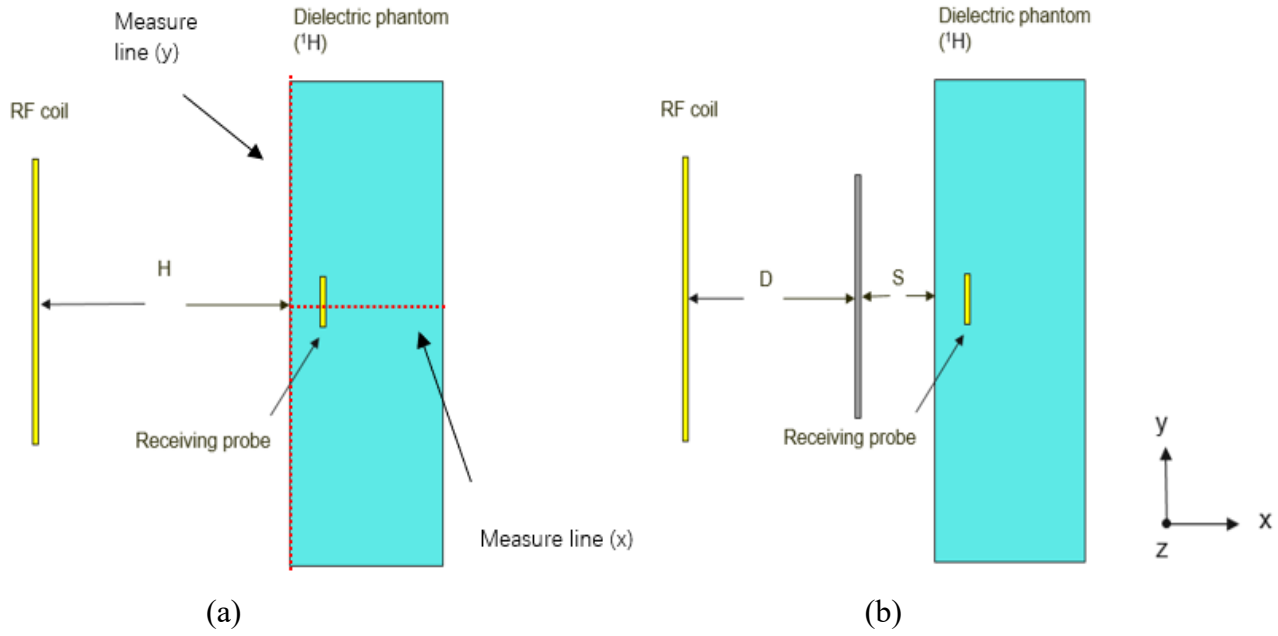

(a) (b)

Fig. 3.2 Cross section of the MRI system. (a) RF coil only. (b)With metasurface

3.3 RF coil design and characterisation

The rectangular RF coil was adopted and worked as a transceiver, and it had larger inductance than the circular coil in similar size. The rectangular coil is manufactured in an easier way by copper taper. In the simulation, the material of the RF coil was defined as copper (ANNEALED), and the size is shown in Fig. 3.3.

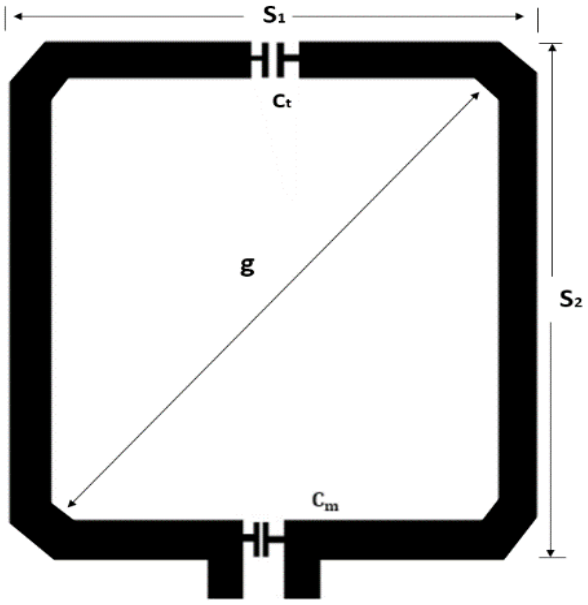

Fig. 3.3 Schematic of RF coil

As shown in Fig. 3.3, S_1 is the width of the rectangular coil (100mm), S_2 is the length (100mm), g is the diagonal (141.4mm), c is the width of the corner (6mm), and b is the thickness of the coil (0.03mm). In addition, there are two 5mm gaps at the top and bottom of the coil to load the tuning capacitor and matching capacitor, respectively. The tuning capacitor Ct was used to tune the resonance of the coil into focused frequency band, and the matching capacitor was used to match the impedance to 50 Ω to ensure the best radiation performance.

$$\mathrm{L} = 0.921\left[(\mathrm{S1}+\mathrm{S2})\log 10\frac{2s1\cdot s2}{b+c} - S1log10(S1+g) - \mathrm{S2}\log 10(\mathrm{S2}+\mathrm{g})\right] + 0.4[2\mathrm{g} - \frac{S1+S2}{2} + 0.447(\mathrm{b}+\mathrm{c})] \qquad (3.1)$$

The inductance of the RF coil can be calculated by Eq. (3.1). The equivalent inductance of the RF coil was calculated to be 283.2nH. The value of the tuning capacitor can be predicted by $\omega_0 CL = 1$, where the resonant frequency is 63.85MHz for 1.5T MRI system. Then, the tuning capacitor was initially set as 21.9pF.

3.4 Surface impedance setting

The parameters of the metasurface that produces the higher enhancement in 1.5T MRI are predicted by using surface impedance method firstly.

This layer set as a large surface to cover the whole phantom firstly, which was a square with length of 400mm and 0.8mm thickness. The impedance of the layer was set as no resistance, and reactance set as XΩ at 63.85MHz by changing impedance setting in 'surface impedance' in CST. It should be noticed that, the reactance of a structure should be variable with frequency according to the formula:

$$X = -\frac{1}{2\pi f c} \qquad (3.2)$$

When the value of X was chosen at the 63.85MHz, the fixed value of capacitance c can be calculated. Then, substituting the fixed value of c and a full frequency range (0MHz to 100MHz) into the formula 3.2, there was a reactance list which has corresponding X for each other frequency can be obtained, and this list was loaded in reactance of capacitive layer surface impedance. In this section, the magnitude of the magnetic field will be used to compare the enhancement from the metasurface to the MRI system, which is proportional to the flux density $|B_1|$ and SNR. In this part, the magnetic field monitor is set to measure the magnetic field along x-axis, from the phantom forward surface (x=25mm, y=0, z=0) to the back surface of the phantom (x=165mm) by a measuring line. The RF coil was fed by 1W, 50Ω source. When measuring the magnetic

field, the resonant frequency of all cases was tuned into 63.85MHz, and the impedance was matched.

The dimension of the metasurface was set as 160mm×160mm (ensure covering the whole RF coil) and the distance between coil and the dielectric phantom is 25mm. Then,the relationship between the reactance of the capacitive layer and the magnitude of the magnetic field was investigated, in order to predict the capacitance value of the metasurface which provides higher improvements in magnetic field inside of the phantom.

The Fig. 3.4 indicated the S_{21} results after frequency tuning and impedance matching, when the reactance of the metasurface was adjusted from -5Ω to -20Ω. When X=-5Ω, there was an obvious distortion in the system, this might cause uneven imaging or other safety problem. When X=-10Ω, the S21 was increased about -2.6dB compared with RF coil only case.

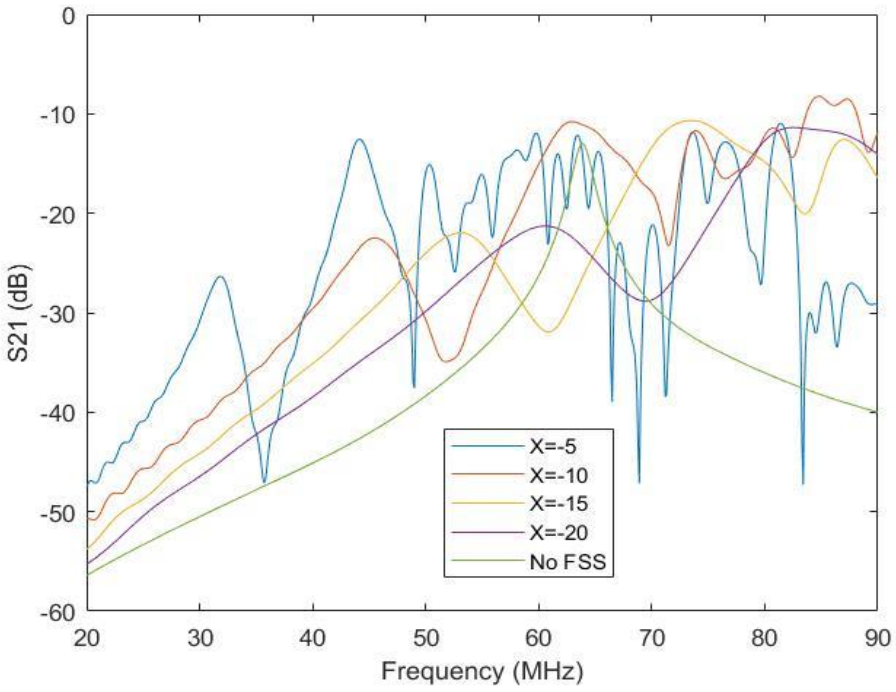

Fig. 3.4 S21 when the reactance of layer adjusted

Fig. 3.5 shown the magnetic field results along x-axis when the reactance of the metasurface was adjusted from -5Ω to -20Ω. It could be found that, lower reactance could provide a stronger magnetic field, because the highest magnetic field in each

figure was X=-5Ω. However, as discussed in the last part, lower reactance made low tolerance and unstable system. Then, lower reactance also increased the difficulty of layer design and practical manufacturing, because of large capacitance requirement. Thus, the capacitive layer with the surface impedance of -10Ω and in the dimension of 160mm×160mm is the predicted metasurface used in the design.

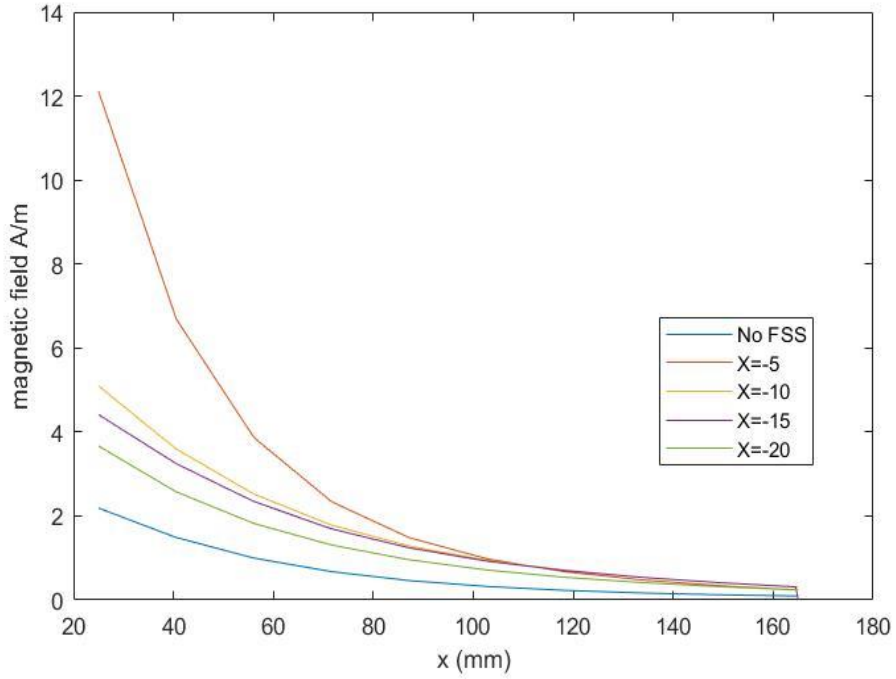

Fig. 3.5 Magnetic field along x-axis when the reactance of metasurface was adjusted

3.5 Metasurface design

Fig. 3.6(a) shows the cross section of the capacitive layer used in this case, and Fig. 3.6(b) presents the top surface of the layer. The CIS consists of two layers printed on the top and bottom surface of a 0.8mm thick FR4 substrate (ε_r=4.3), and the bottom layer is an orthogonal copy of the top layer to formulate the dual polarization. The type of the CIS adopted the interdigital surface which had high capacitance density and was beneficial for the miniaturization of the element [87]. The dimension of the CIS could be described by the size of metasurface D, the length of digits L, the width of digits w_d,

the gap between each digits g_d, and the number of digits N. The digits were assumed to be copper with thickness of 32μm. The RF currents were allowed to follow the additional horizontal strip line on the top and bottom.

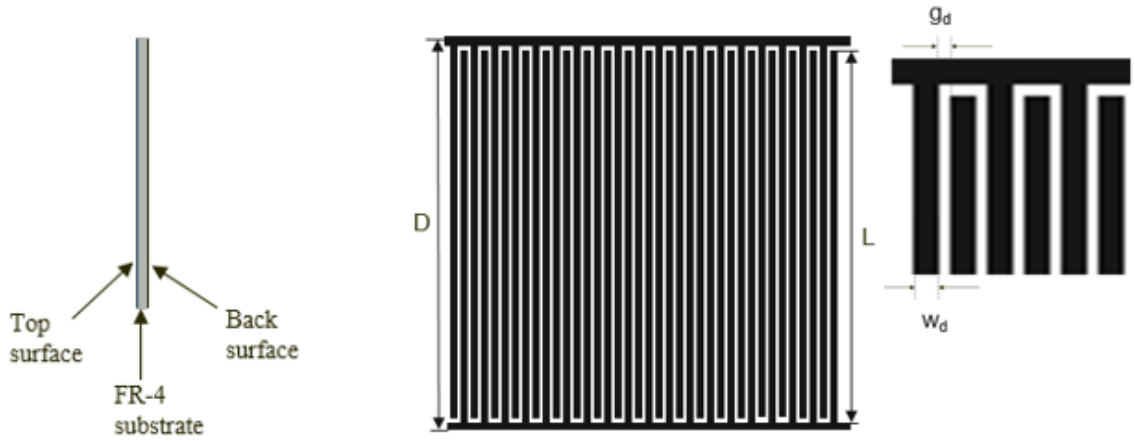

(a) (b)

Fig. 3.6 (a) The cross section of the metasurface, (b) The front view of the metasurface

The capacitive layer structure proposed in chapter 1 had a predicted reactance of -15 Ω by using 'surface impedance' method. Then the parameters of the interdigital element can be estimated by:

$$C = \frac{\varepsilon_{eff}(N-1)D}{18\pi} \cdot \frac{K(k)}{K\prime(k)} \tag{3.3}$$

$$\frac{K(k)}{K'(k)} = \begin{cases} \frac{1}{\pi}\ln\left[\frac{2\left(1+\sqrt{k}\right)}{1-\sqrt{k}}\right] & 0.707 \le k \le 1 \\ \frac{\pi}{\ln\left[\frac{2\left(1+\sqrt{k'}\right)}{1-\sqrt{k'}}\right]} & 0 \le k \le 0.7 \end{cases} \tag{3.4}$$

$$k = \tan^2\left(\frac{a\pi}{4b}\right),\ a = \frac{wd}{2},\ b = \frac{wd+gd}{2},\ k' = \sqrt{1-k^2}.$$

where K(k) is the complete elliptic integral and K'(k) is its complement, D is the dimension of the metasurface, N is the number of strip lines, ε_{eff} depends on the material of substrate used in unit cell design, w_d is width of strip line, and g_d is the gap between each strip line. In this case, the substrate material as adopted the FR-4 with permittivity of 4.3. Thus, $\varepsilon_{eff} = \frac{\varepsilon_{r+1}}{2} = 2.65$.

As discussed before, only one capacitive layer was used in this case. The dimension of the capacitive layer was set as 100mm×100mm. For example, when the length of the strip line *l* was set as 100mm, the gap between each strip line g_d was set as 0.8mm, and the width of the strip line w_d was set as 1.5 mm. Then, the dimension of the metasurface D should be the sum of the length of the strip line, the gap between each strip line and the width of the strip line, i.e. 100+1.5×2+0.8=103.8mm.

Then, in order to make the unit cell a regular square, the number of strip lines should satisfy:

$$N = \frac{D}{(w_d+g_d)} = \frac{103.8}{1.5+0.2} \approx 46 \qquad (3.6)$$

Finally, the equivalent capacitance of the metasurface with w_d=1.5 mm, *l*=100 mm, and g_d=0.8mm was calculated to be 183.8pF.

It should be noted that, these equations are based on the assumption that the thickness of the substrate approaches to infinite. However, in fact, the thickness of the substrate was 0.8mm in this case, leading to an error in the estimated capacitance of the metasurface. However, the estimate value could also provide a changing trend of the capacitance when adjusting the geometrical parameters of the metasurface. Using the same approach, the w_d, g_d and *l* were changed sequentially when other parameters were kept constant, so different metasurfaces were designed and their equivalent capacitances were also calculated. Fig. 3.7, Fig. 3.8 and Fig. 3.9 show the equivalent

capacitance of the metasurface with the change of w_d, g_d and l, respectively. Both Fig. 3.7 and Fig. 3.8 show a declining trend in the capacitance when w_d or g_d is increased. When l is increased, the capacitance of the metasurface has an exponential increment, as shown in Fig. 3.9. The material of the strip lines was set as copper, and the material of the substrate was set as FR-4, with a thickness of 0.8mm.

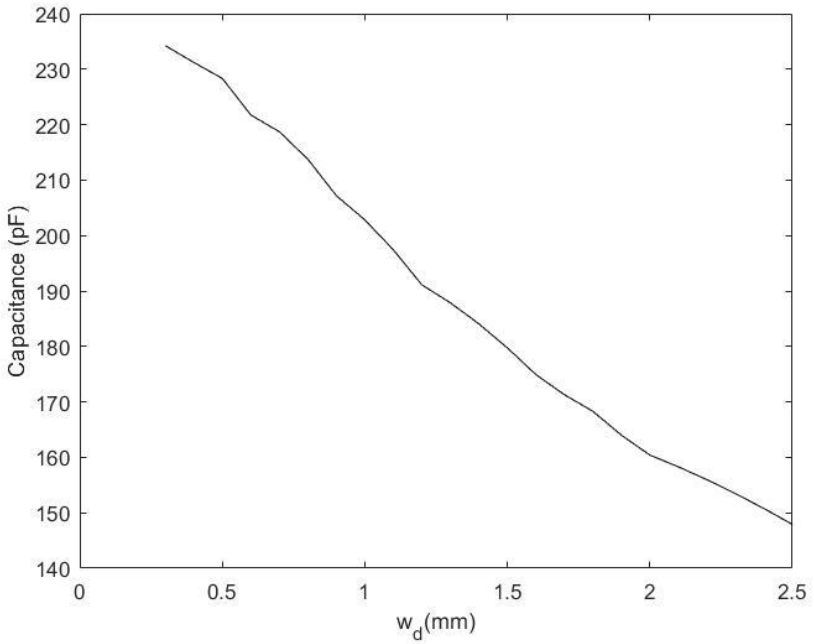

Fig. 3.7 The estimated capacitance of the metasurface when changing w_d

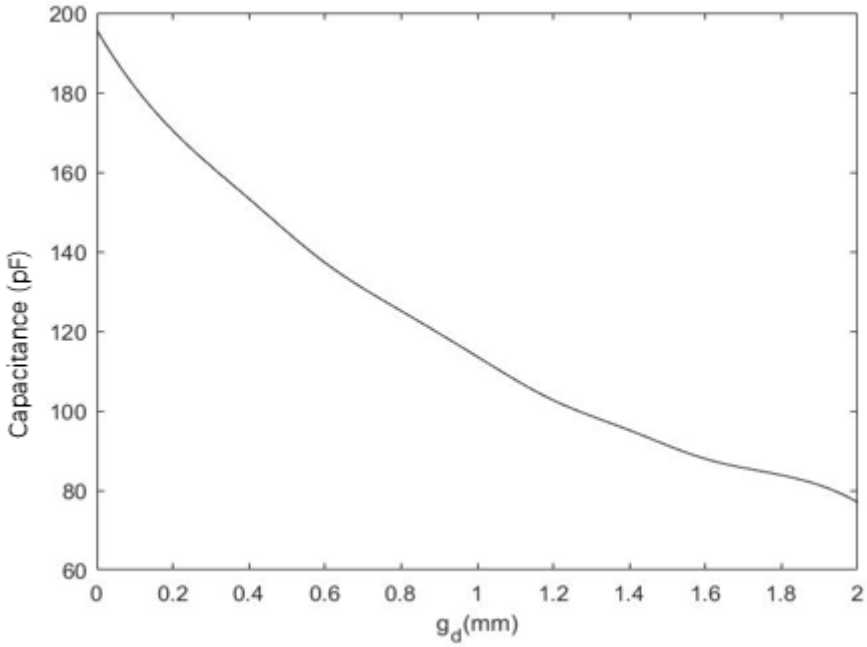

Fig. 3.8 The estimated capacitance of the metasurface when changing g_d

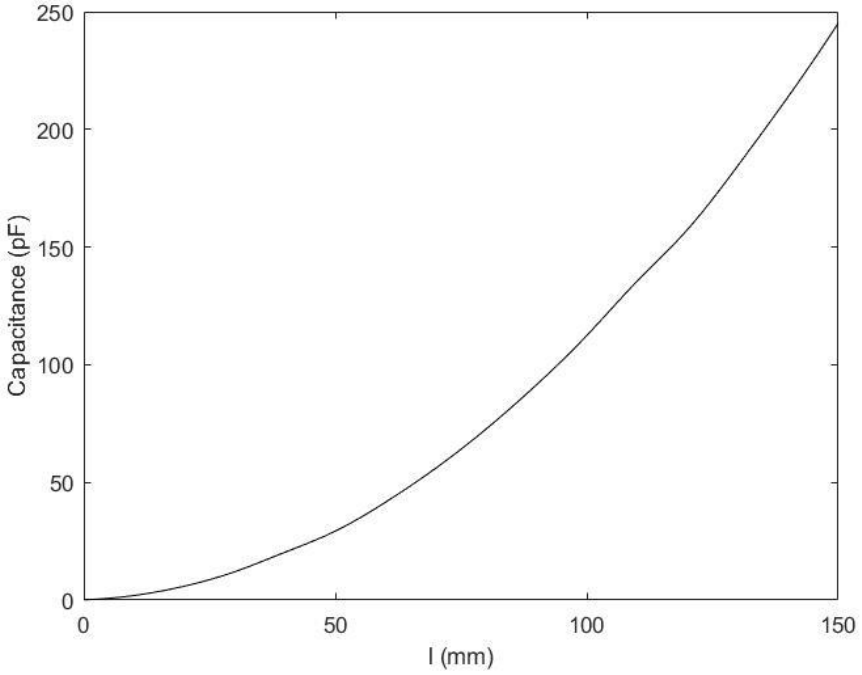

Fig. 3.9 The estimated capacitance of the metasurface when changing l

3.6 Simulation results of the RF transceiver system

3.6.1 Magnetic flux density B_1^+

In order to determine the properties of the metasurfaces designed from the last case, the MRI scenario combined with different metasurfaces was tested in CST. In this case, the positive magnetic flux density was measured firstly. The magnitude of the positive magnetic flux density $|B_1^+|$ inside the dielectric phantom was monitored along the x-axis when y=z=0, with D=20mm, S=5mm and a 1W 50Ω source. In this subsection, the $|B_1^+|$ across the dielectric phantom is demonstrated with w_d, g_d and l changing independently. The results of $|B_1^+|$ corresponded to the transmission efficiency of the MRI system, and the 2D $|B_1^+|$ field was also be monitored in this case.

It was found in Section 3.4 that when the capacitance of the metasurface was 166 pF (reactance=-15 Ω), the maximum B_1^+ could be achieved. The estimated capacitance of

the metasurface had been investigated in Section 3.5. From Fig. 3.7, at w_d=2.1mm, the capacitance of the metasurface was about 162.8pF. So, this metasurface with w_d=2.1mm, g_d=0.8mm, and l=100mm was firstly tested in CST. Besides, three other metasurfaces with different w_d were also tested to show the effects of w_d on $|B_1^+|$. Table. 3.1 shows the estimated capacitance of the metasurfaces tested in the simulation with different w_d. From Fig. 3.10, when w_d=1.8 mm, the $|B_1^+|$ obtained the highest value at the dielectric phantom surface, and the enhancement provided by the metasurface covered a penetration depth of about 50 mm. The metasurface design with w_d=2.1 mm, g_d=0.8 mm, l=100 mm had the similar capacitance as expected, which however did not improve the $|B_1^+|$ as expected. Therefore, it could be deduced that there was no obvious relationship between w_d and $|B_1^+|$, but oversize w_d would reduce the performance of the metasurface.

w_d (mm)	N	Capacitance (pF)
1.5	45	183.8
1.8	40	172.6
2.1	36	162.8
2.4	33	155.5

Table 3.1 The estimated capacitance of the metasurface when changing w_d.

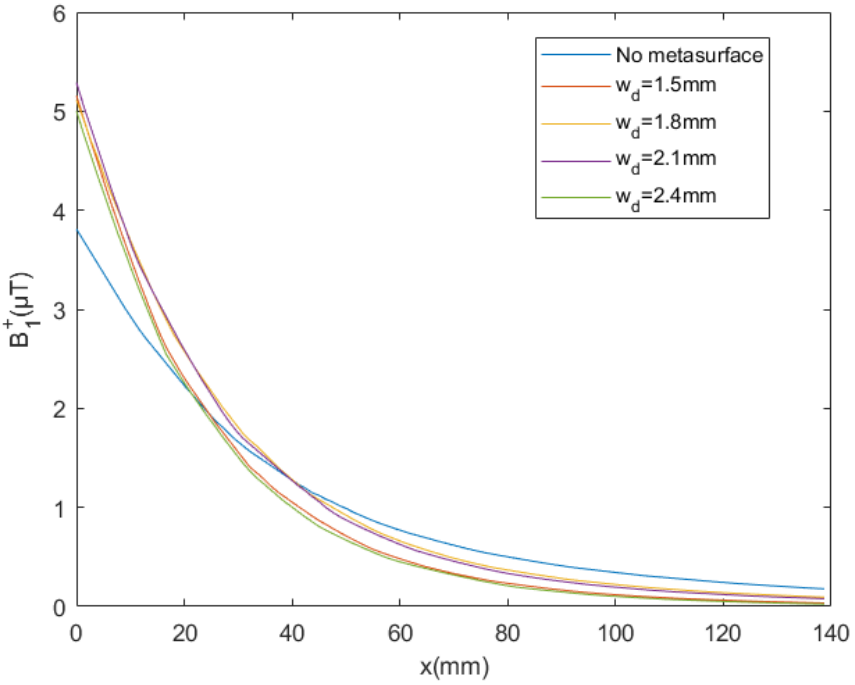

Fig. 3.10 The magnitude of magnetic flux density |B1+| inside the dielectric phantom along the x-axis when changing w_d.

The optimal design of w_d=1.8 mm, g_d=0.8 mm, l=100 mm from the last case was selected to perform further optimization. Table 3.2 shows the estimated capacitance of the metasurfaces tested in this case, where only g_d was adjusted, and w_d=1.8 mm, l=100 mm. Fig. 3.11 illustrates the positive magnetic flux density $|B_1^+|$ when g_d was adjusted. In this case, $|B_1^+|$ showed more regular changes when changing g_d. When g_d=0.2 mm, the metasurface had the highest capacitance of 170.4 pF, while the lowest enhancement in $|B_1^+|$ was obtained.

g_d (mm)	N	Capacitance (pF)
0.2	51	170.4
0.5	45	145
0.8	40	125
1.1	36	109.6

Table 3.2 The estimated capacitance of the metasurface when changing g_d.

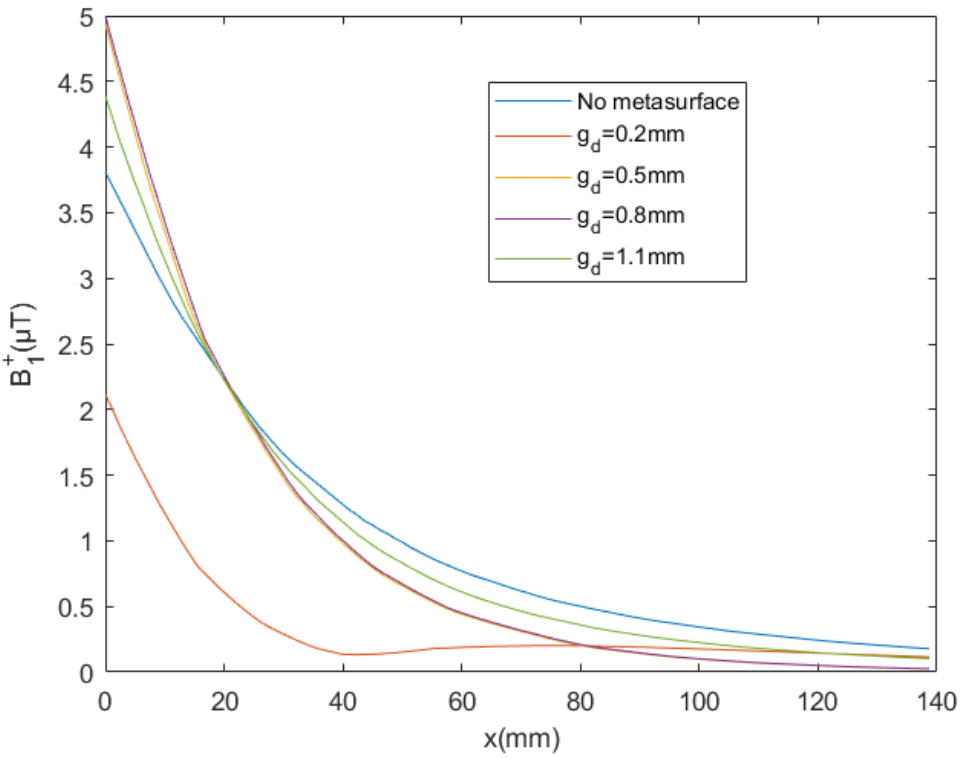

Fig. 3.11 The magnitude of magnetic flux density |B1+| inside the dielectric phantom along the x-axis when changing g_d.

The optimal design of w_d=1.8 mm, g_d=0.8 mm, and l=100 mm from the last case was selected to investigate the relationship between l and $|B_1^+|$. Table 3.3 shows the metasurface designs tested in this case, where only l was adjusted, and w_d=1.8 mm, g_d=0.8 mm. Fig. 3.12 illustrates the positive magnetic flux density $|B_1^+|$ when l was adjusted. In this case, the results of $|B_1^+|$ showed that smaller metasurface would increase the penetration depth, as reflected by the gradient of each value of $|B_1^+|$. It was found that when l=80 mm, $|B_1^+|$ was improved by 89% at the dielectric phantom surface, and the whole penetration depth was enhanced.

l (mm)	N	Capacitance (pF)
60	24	41.6
80	32	72.69
100	40	112.4
120	47	157.381

Table 3.3 The estimated capacitance of the metasurface when changing *l*.

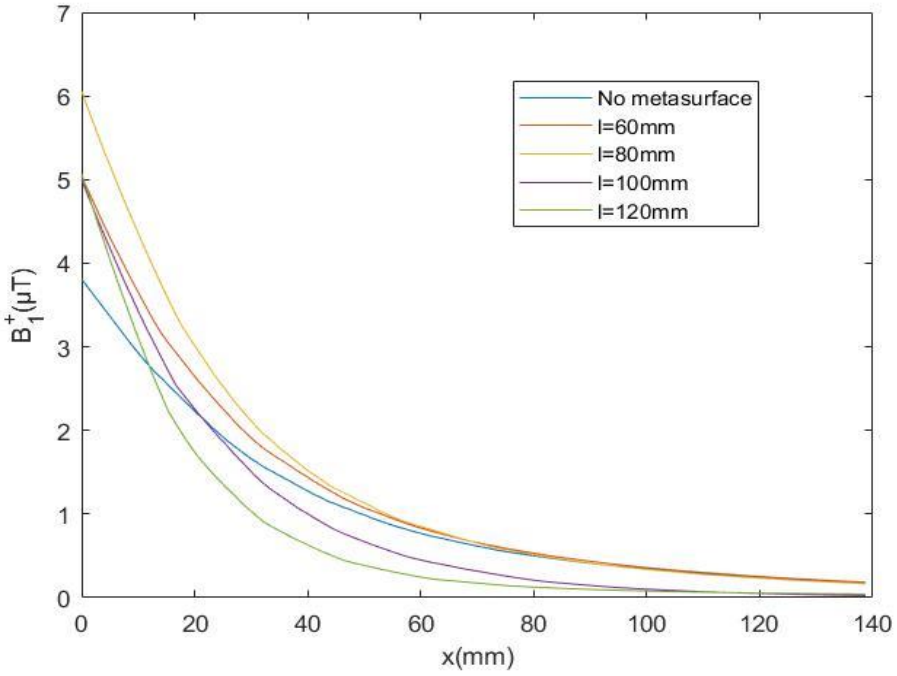

Fig. 3.12 The magnitude of magnetic flux density $|B1^{+}|$ inside the dielectric phantom along the x-axis when changing *l*.

3.6.2 Magnetic flux density B_1^+ field in 2D

One of the biggest gaps between previous researches in the field of interested and this research will be illustrated. The optimal design of w_d=1.8 mm, g_d=0.8 mm, and *l*=100 mm was investigated in details where the $|B_1^+|$ field in the x-y plane is represented by a false colour 2-D plot in Fig. 3.13. Fig. 3.13(a) shows the standard response near the metallic elements of the coil under intense field and a gradually decaying distribution

into the phantom, when the metasurface is removed. The squint in the field was due to the finite conductivity of the phantom. When the metasurface was placed between the RF coil and the phantom, there was a stronger field distribution near the coil and the surface of the phantom (Fig. 3.13(b)). In this case, the metasurface with high capacitance had an impact on the resonant frequency and the coil impedance, so different tuning and matching elements were required. The metasurface was acting as a second source to enhance the $|B_1^+|$ provided by the RF coil between the inductive RF coil and the dielectric phantom, and the field between the RF coils elements had increased significantly.

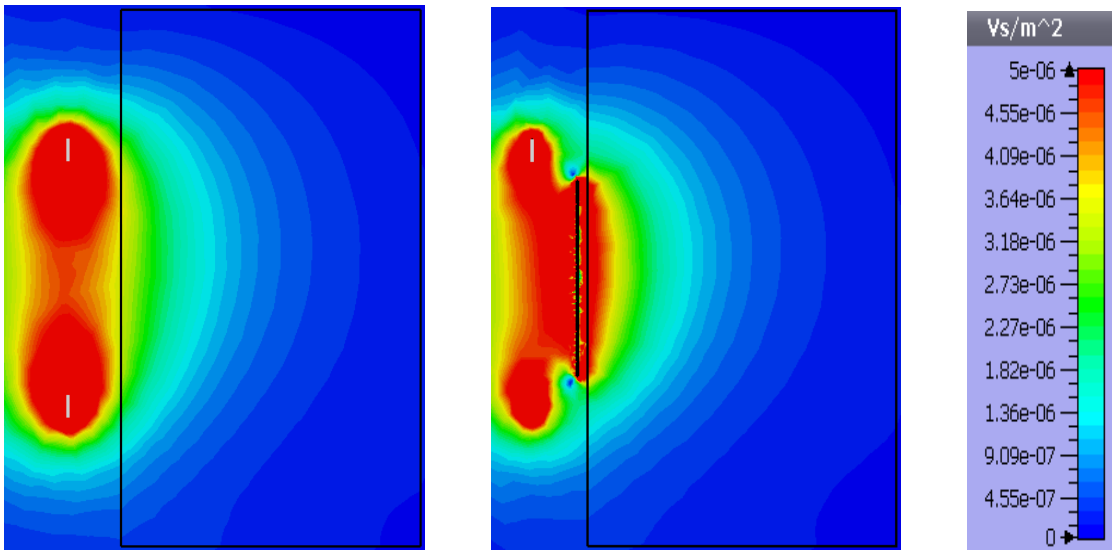

(a) (b)

Fig. 3.13 The 2D results of the magnetic flux density $|B1^+|$. (a) RF coil only. (b) With metasurface

Further, the field did not show any fluctuations as expected when applying periodic structures to multiple metasurface unit cells. Fig. 3.14 shows the 2D $|B_1^+|$ results from the research[88], when the periodic-structure metasurface was placed between the RF coil and the dielectric phantom in a 1.5T MRI system. The homogeneous field was influenced by the periodic structure, because the surface current would flow in the gap

between each unit cell instead of passing through the metasurface. The non-periodic structure used in this case improved the $|B_1^+|$ without influencing the evenly-distributed fields. Compared with Fig. 3.13, the effects of the metasurface on the uniformity of the $|B_1^+|$ could be avoided by using non-periodic structure. This benefit would enhance the susceptivity of the RF coil to increase the image quality.

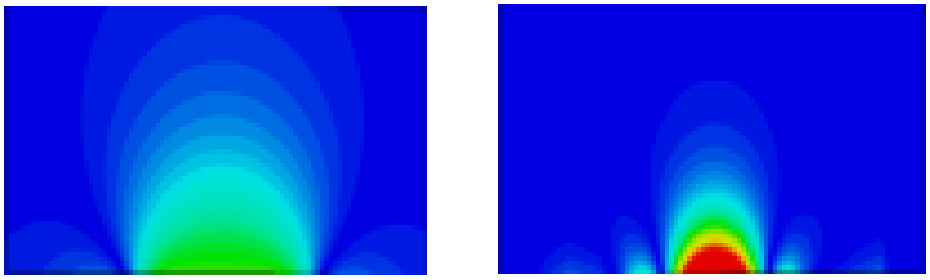

(a) (b)

Fig. 3.14 The 2D results of the magnetic flux density $|B1^+|$. (a) RF coil only. (b) With periodic-structure metasurface [88]

3.6.3 Normalized b1- along x-axis and y-axis and improvement

According to the formula 1.6, SNR is also characterized by the power absorption. In this subsection, the negative magnetic flux density (B_1^-) would be normalised with the power absorption to compare the receiver sensitivity of each case. A 1 W signal source was used to feed the RF coil. In this case, the magnitude of the normalised negative magnetic flux density $|B_{1\ nor}^-|$ inside the dielectric phantom was monitored along the x-axis. In order to do the fair comparison, the magnetic field and magnetic flux density were normalised to the square root of the power absorbed in the whole system. The absorbed power in the whole system for the cases of coil only P_{absNM} and within the metasurface P_{absM} can be calculated by Eq. (3.7) and Eq. (3.8), respectively.

$$P_{absNM} = P_{abs\ coil} + P_{abs\ ph} \qquad (3.7)$$

$$P_{absM} = P_{abs\,coil} + P_{abs\,ph} + P_{abs\,meta} \quad (3.8)$$

$$B_1^- nor = \frac{|B_1^-|}{\sqrt{P_{absL}}} \quad (3.9)$$

Where $P_{abs\ coil}$ is the absorbed power in the RF coil, $P_{abs\ ph}$ is the absorbed power in the dielectric phantom, and $P_{abs\ meta}$ is the absorbed power in the metasurface.

Fig. 3.15 shows the $|B_1^-{}_{nor}|$ along the x-axis of the dielectric phantom when w_d was adjusted. The results illustrated that the width of strip line could affect the enhancement in the $|B_1^-{}_{nor}|$ when w_d was changed from 1.5mm to 2.4mm. The $|B_1^-{}_{nor}|$ was always improved on the surface of phantom, and the maximum improvement on the phantom surface was 38% compared with the case of coil only at w_d=1.8 mm. From the surface impedance investigation in section 3.4, the metasurface significantly increased the whole penetration depth compared with the case of coil only. The improvement in penetration depth obtained in this case did not meet our expectation obtained by the 'surface impedance' approach with the largest increase in penetration depth being 38 mm when w_d=1.8 mm. It can be observed that there is a limit in the maximum increase of $|B_1^-{}_{nor}|$. For example, when w_d was increased over 2 mm, $|B_1^-{}_{nor}|$ would not keep increasing, and no further improvement could be achieved when w_d was smaller than 1.5mm.

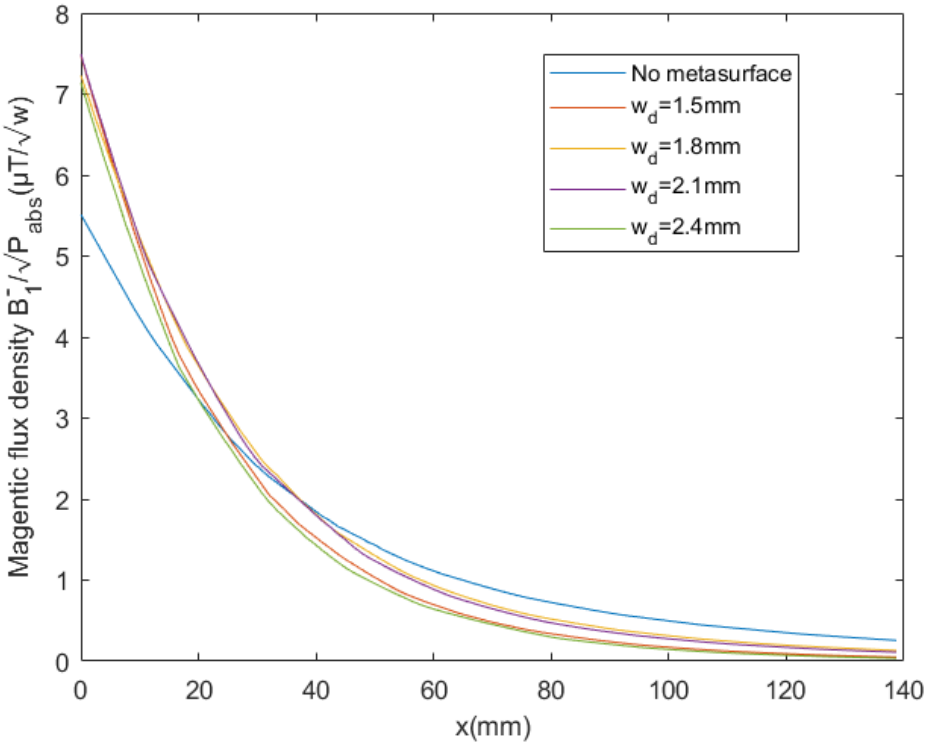

Fig. 3.15 The normalised B1- inside the dielectric phantom along the x-axis when w_d was adjusted

Fig. 3.16 shows the variation in the gap between each strip line. The results illustrated that g_d had more obvious effects on optimizing the penetration depth. In this case, all of metasurface designs also provide the enhancement in the $|B_1^{-}{}_{nor}|$ on the phantom surface. However, this enhancement only covered about 8 mm penetration depth when g_d=0.5 mm. The maximum $|B_1^{-}{}_{nor}|$ on the phantom surface and the largest penetration depth could be obtained at the same time when g_d=0.8mm.

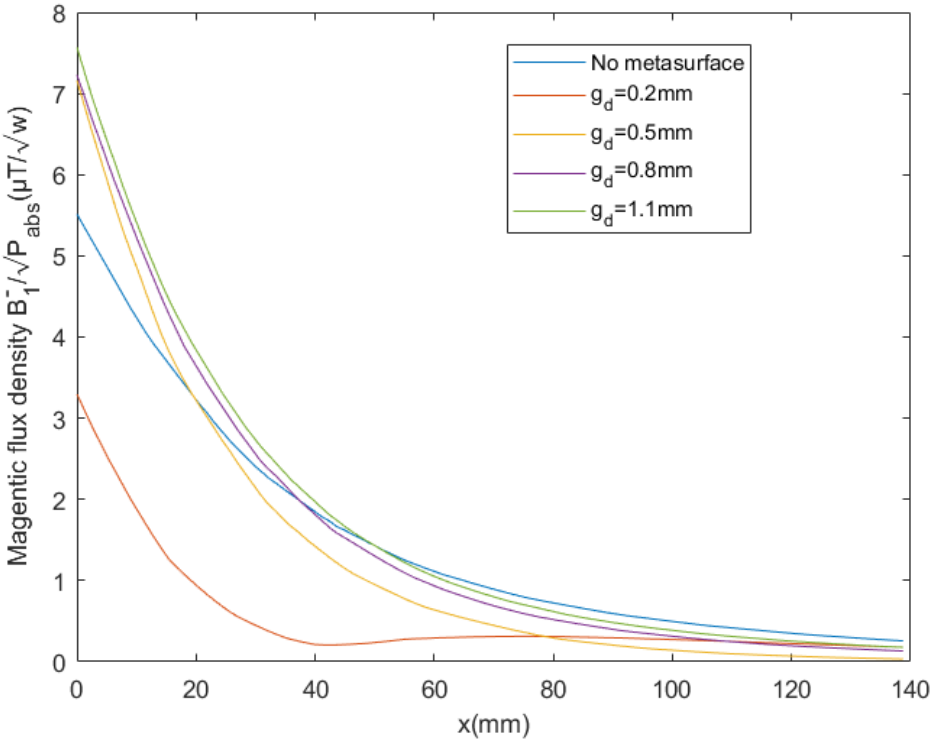

Fig. 3.16 The normalised B1- inside the dielectric phantom along the x-axis when $g_d$was adjusted

Fig. 3.17 shows the variation of the length of strip line. In this case, the length of the strip line l was adjusted from 60mm to 120mm with w_d=1.8mm and g_d= 0.8mm. From the results of $|B_1^-{}_{nor}|$, the highest $|B_1^-{}_{nor}|$ on the phantom surface was 8.7. When l was set as 80 mm, the enhancement covered the whole penetration depth compared with the case of coil only. In the MRI system, the penetration depth is an important parameter to influence the image quality, because most of imaged organs are far away from the skin. Therefore, the dimension of metasurface of w_d=1.8mm, g_d=0.8mm, l=80 mm was selected as the most suitable design for 1.5T MRI systems.

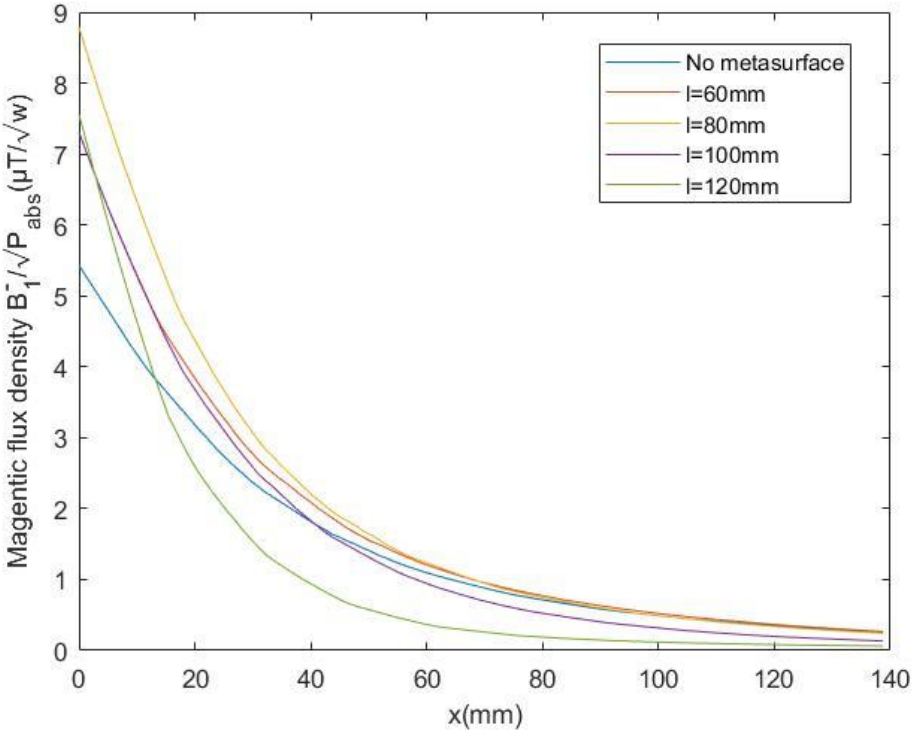

Fig. 3.17 The normalised B1- inside the dielectric phantom along the x-axis when *l* was adjusted

For more in-depth analysis, the improvement in the normalised B_1^- can be calculated by:

$$Improvement\ (\%) = \frac{(B_1^-{}_{norCIS} - B_1^-{}_{norNCIS}) * 100\%}{B_1^-{}_{norNCIS}} \qquad (3.10)$$

where $B_1^-{}_{norNCIS}$ is the $|B_1^-{}_{nor}|$ without a metasurface, and $B_1^-{}_{norCIS}$ is the $|B_1^-{}_{nor}|$ with a metasurface. Fig. 3.18 clearly shows the improvement in B_1^- over the full range of the x-axis when the length of strip line was changed. The line of 0% was used as the reference to show the improvement in penetration depth. Decreasing the length of the metasurface can increase the enhanced penetration depth, but the total improvement would be decreased when *l* was less than 80 mm. When *l* was 80mm, $|B_1^-{}_{nor}|$ was enhanced by 67% on the phantom surface.

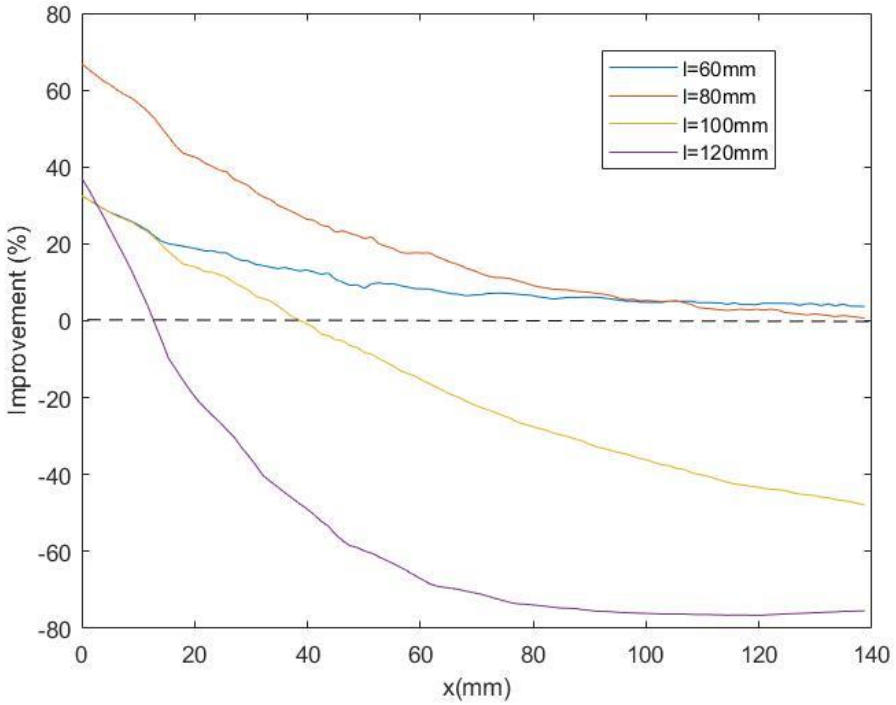

Fig. 3.18 The improvement in normalised flux density along x-axis when *l* was adjusted

Fig. 3.18 shows the $|B_1^-{}_{nor}|$ on the phantom surface along the y-axis. As shown in the figure, the effective imaging region along y-axis was from -50 mm to 50 mm when the metasurface was absent, and that was from -40 mm to 40 mm when the metasurface was present. The $|B_1^-{}_{nor}|$ was improved by about 67% around the central area when the metasurface was provided. This proves that metasurface sacrificed some imaging area to enhance the SNR around the central area.

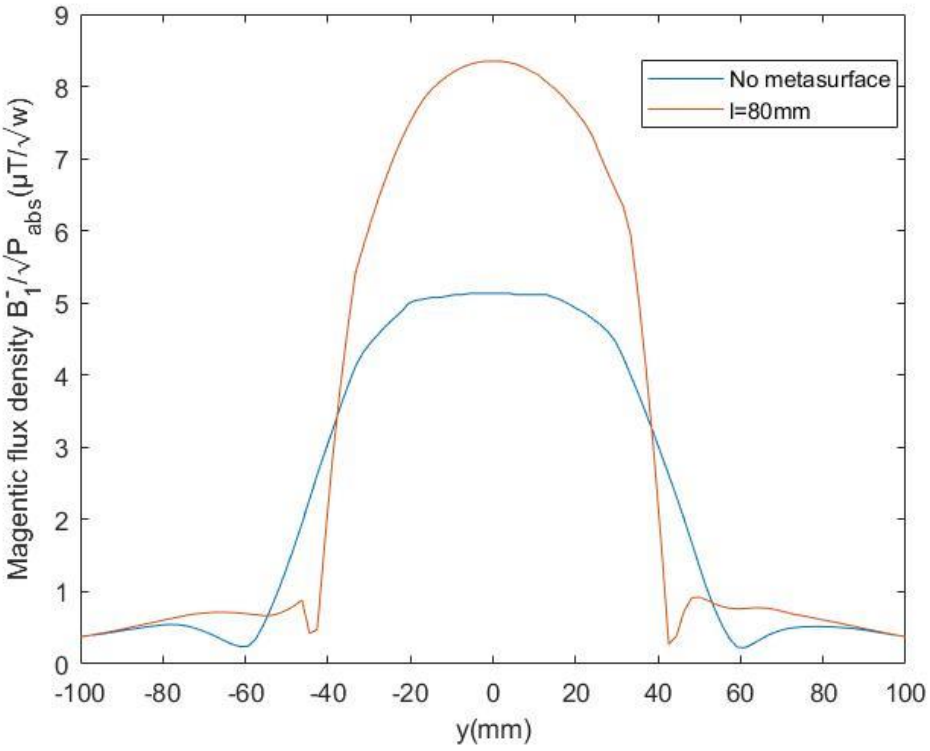

Fig. 3.19 The normalised B_1^- on the dielectric phantom surface and along the y-axis

3.6.4 Effects of the parameters D, S and H

The effects of the variation in parameters D, S, and H were investigated to find the relationship between them and $|B_1^-{}_{nor}|$. Fig. 3.20 provides the $|B_1^-{}_{nor}|$ results inside the dielectric phantom along the x-axis, when D was changed. As can be seen, very small increments were made in the $|B_1^-{}_{nor}|$ when D was increased. Fig. 3.21 indicates the results of $|B_1^-{}_{nor}|$ when S was adjusted, where $|B_1^-{}_{nor}|$ and penetration depth decreased regularly. When H was adjusted, D was kept as 20mm. From Figure 3.22, the changes in $|B_1^-{}_{nor}|$ when H was adjusted have the similar trend as that when S was adjusted. It can be found that $|B_1^-{}_{nor}|$ had larger dependence on the distance between the metasurface and the dielectric phantom, instead of the spacing between the RF coil and the phantom. Therefore, the metasurface plays a leading role in the transmission of an MRI model.

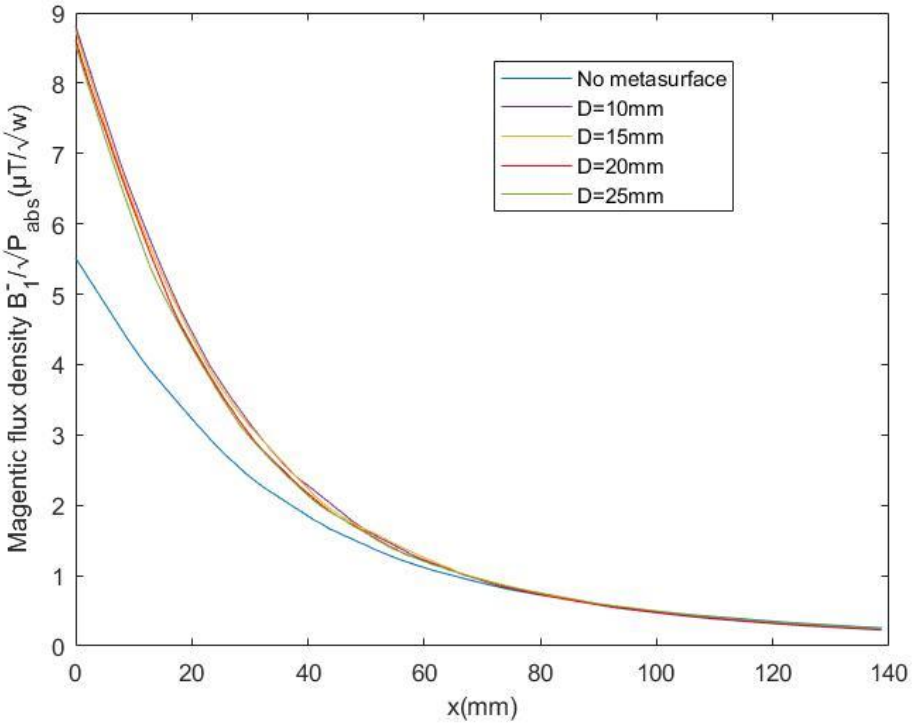

Fig. 3.20 The normalised B_1^- inside the dielectric phantom along the x-axis when D was adjusted

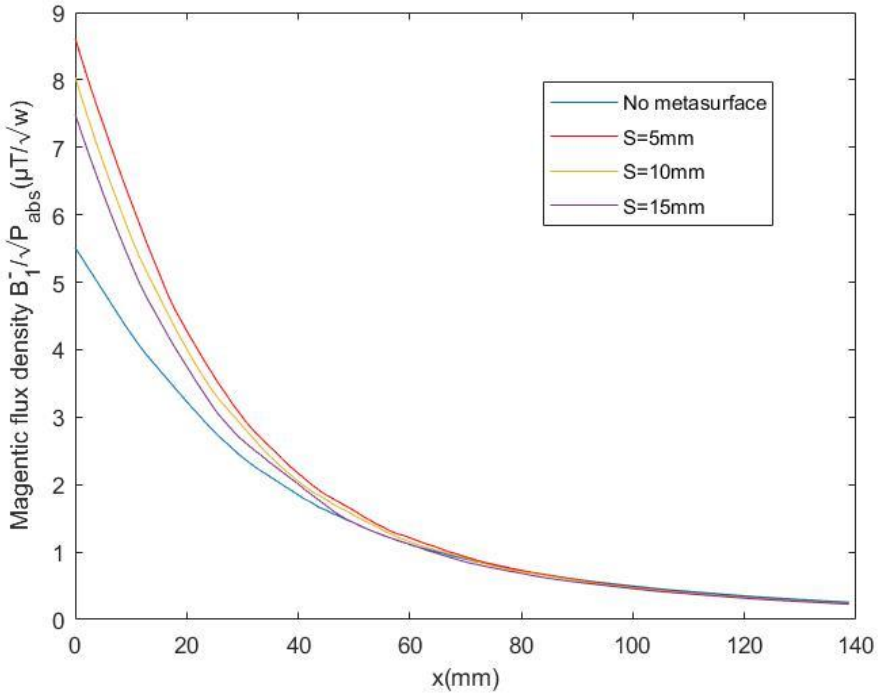

Fig. 3.21 The normalised B_1^- inside the dielectric phantom along the x-axis when S was adjusted

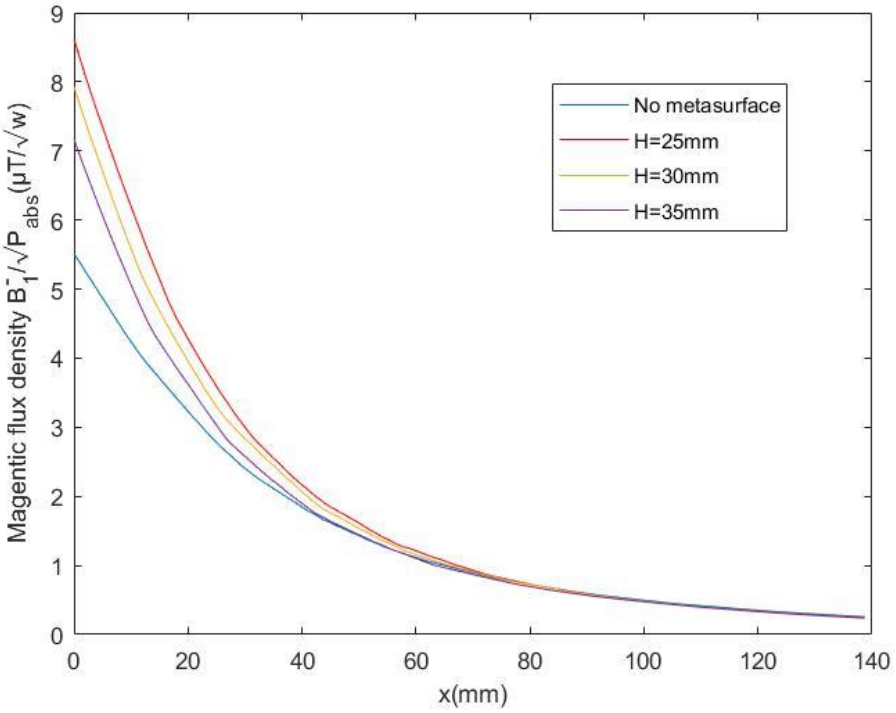

Fig. 3.22 The normalised B_1^- inside the dielectric phantom along the x-axis when H was adjusted

3.6.5 The mean value of magnetic field and magnetic flux density of specified volume

The optimal design of the metasurface was w_d=1.8mm, g_d=0.8mm, and l=80mm after adjusting the parameters of the metasurface and comparing the results of $|B_1^+|$. In the last case, $|B_1^+|$ was measured by a measure line (x=25-165 mm, y=z=0) in each case. In this subsection, the mean value of $|B_1^+|$ was measured by a certain volume, to clearly show the enhancement of $|B_1^+|$ in a part of human body.

Five cuboids with the same volume were enclosed by the range along x-axis (from 0mm to 71mm), which was obtained using the long side length of the RF coil S2 (100mm) divided by $\sqrt{2}$. The range along y-axis (from -50mm to 50mm) which was the short side length of the RF coil S1 (100mm). The length along z-axis varied from -50mm to -40mm, from -30mm to -20mm, from -5mm to 5mm, from 20mm to 30mm and from

40mm to 50mm. Take z=40-50mm for example, the volume enclosed by the red line in Fig. 3.23 was the specified cube tested in the simulation.

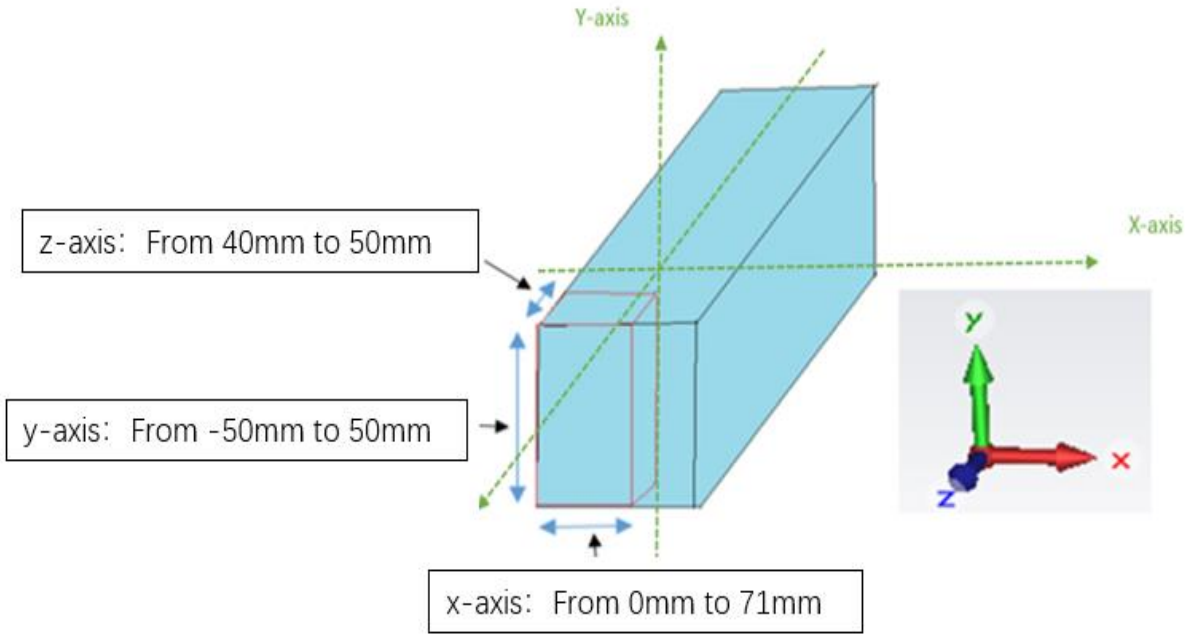

Fig. 3.23 Cube for z=40-50 mm, when x=0-71mm and y=-50-50mm

From Table 3.4, the mean value of the magnetic flux density of specified volume was decreased with the increase in the thickness of reactance layer. In addition, the $|B_1^+|$ results of '-50mm to -40mm' and '40mm to 50mm', and '-30mm to -20mm' and '20mm to 30mm' were almost same, because of the good homogeneous property. The mean values of the $|B_1^+|$ around the centre volume, '-5mm to +5mm' had the same trend as the $|B_1^+|$ shown in Fig. 3.12. The mean value of the $|B_1^+|$ was also not proportional to the length of the metasurface.

		$\|B_1^+\|$ (μT)				
CIS	Equivalent capacitance (pF)	-50mm~-40mm	-30mm~-20mm	-5mm~5mm	20mm~30mm	40mm~50mm
No metasurface	NA	0.61	0.73	1.07	0.73	0.6
L=60mm	61	0.84	1.45	1.74	1.44	0.83
L=80mm	108	0.98	1.6	1.86	1.59	0.97
L=100mm	168	0.86	1.43	1.71	1.42	0.86
L=120mm	236	0.73	1.31	1.6	1.32	0.75

Table 3.4 The mean value of magnetic flux density of specified volume.

3.6.6 Electric field

Fig. 3.24 and Fig. 3.25 show the magnitude of the electric field at x=25mm and x=40mm on the phantom surface and 15 mm inside the phantom, respectively. The magnitude of the electric field was increased by 46% compared with the case with the absence of the metasurface at the maximum electric field position (z=-40mm or z=40mm) on the phantom surface (x=25mm). The electric field was increased by 8% compared to the case with coil only.

Fig. 3.26 provides the change of 2D electric field when the metasurface was present or not. In this case, the length of the strip line was adjusted, so the impact of the dimension of the metasurface could be investigated further. From the results, it was obvious that the electric field around the phantom edge was focused on the centre with the increase in the length of the strip line on the metasurface. It was found that, when the *l* was 100mm, and the dimension of the metasurface was 104.4mm × 104.4mm which was

greater than the length of the RF coil (100mm), the electric field was almost focused on the centre of the dielectric phantom. This was beneficial for increasing the electric field strength, the SAR was also increased by the larger electric field to cause some safety risks, which will be discussed in next section.

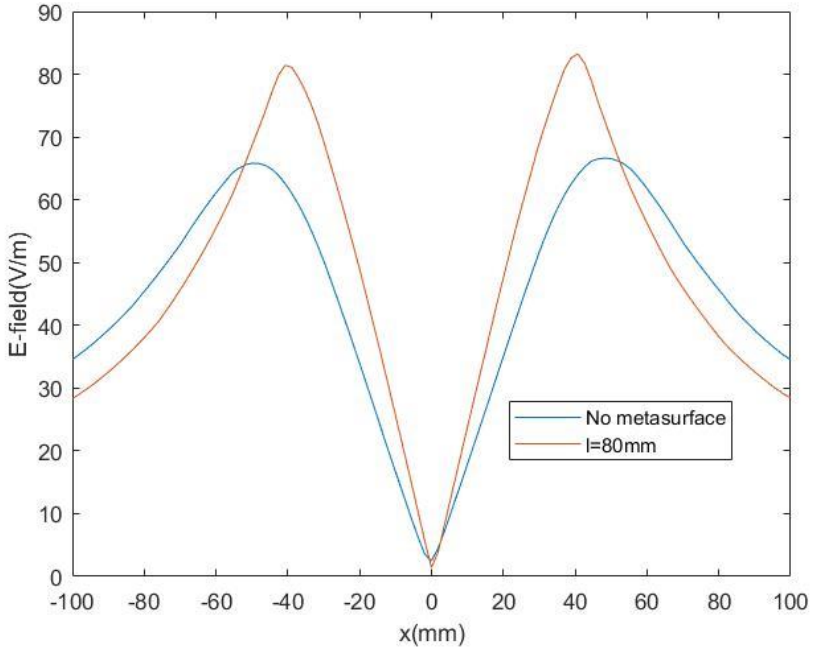

Fig. 3.24 The electric field on the dielectric phantom surface (x=25mm) along the y-axis

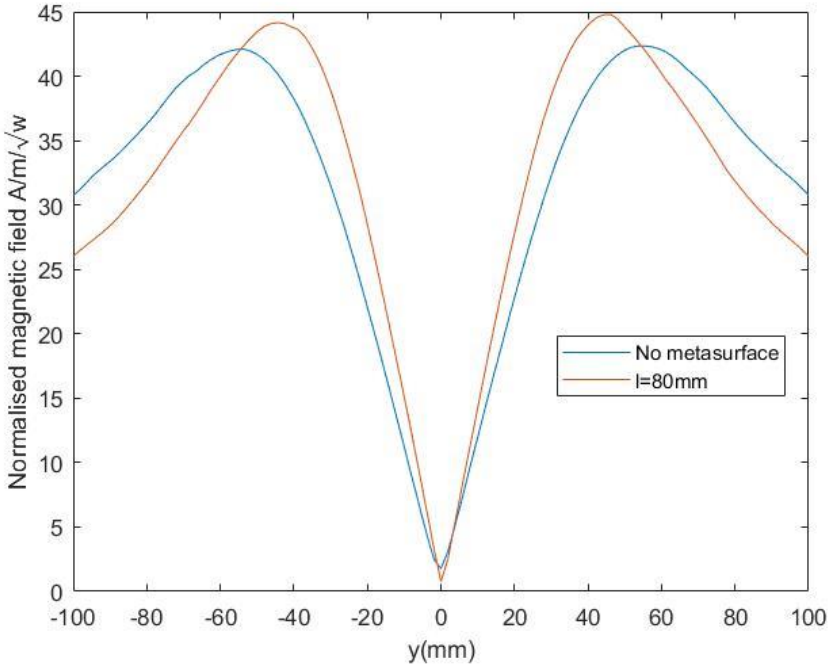

Fig. 3.25 The electric field inside the dielectric phantom (x=40mm) along the y-axis

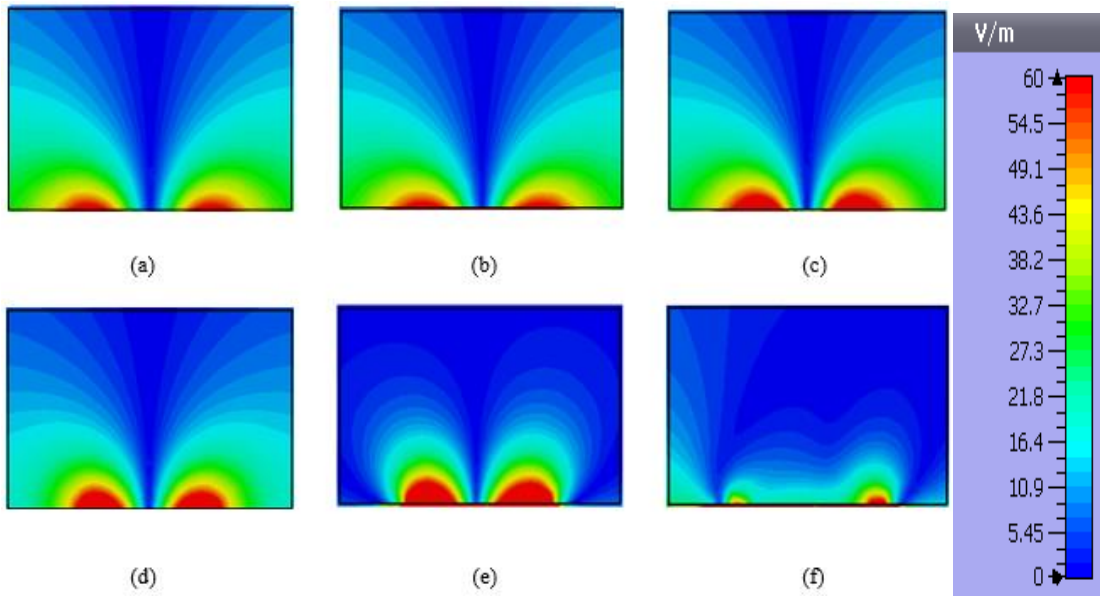

Fig. 3.26 The 2D results of electric field. (a) RF coil only. (b) With metasurface l =60 mm. (c) With metasurface l =80 mm. (d) With metasurface l =90 mm. (e) With metasurface l =100 mm. (f) With metasurface l =120 mm

3.6.7 SAR

As discussed in Section 1.2.3, the safety of MRI systems is measured by SAR, which is proportional to the electric field strength. From the equation of SAR shown in equation 1.11, SAR is proportional to E-field and not correlate to SNR. The simulated SAR values for the maximum 10g case were 4.22W/kg and 3.5W/kg, when the metasurface of w_d =1.8mm, g_d =0.8mm, and l=80mm was present and absent, respectively. The whole-body SAR was 0.36W/kg, and 0.45W/kg for the cases with metasurface and coil only, respectively under a 1W power source. According to IEC60604-2-33/2010, the maximum SAR allowed was 10W/kg for 10g and 2W/kg for the whole body. As a result, both of the local and the whole-body SAR were at the maximum level. The additional metasurface did not significantly increase the SAR, because the non-periodic metasurface used in this case did not enhance the field or B_1^- by focusing the field, and the electric field did not obtain obvious enhancement. Further, for the metasurface with dimension of w_d=1.8mm, g_d=0.8mm, and l=80mm, the SAR

were 4.61W/kg and 0.35W/kg for 10g case and the whole body, respectively. The reason was that the electric field was focused by the metasurface around the central area of the dielectric phantom, but this sacrificed the strength of the electric field at edges. Therefore, the SAR of 10g case was improved compared to the case with no metasurface, but the SAR for the whole body decreased.

3.7 Experimental validation with a dielectric phantom

3.7.1 Measure S-parameter and Q-factor in an RF bench

The capacitive layer with w_d=1.8mm, g_d=0.8mm, and l=100mm was manufactured for experiment. The results of S-parameter were displayed to show the resonance tuning and impedance matching work.

The RF coil was manufactured by the copper tape, and connected to a Vector Network Analyser (RF ZVL). The receiving probe was manufactured by semi-rigid coaxial cable with a diameter of 5cm. The metasurface was generated by using a chemically-etched 32μm copper layer with w_d=1.8mm g_d=0.8mm and l=100mm on a double-sided FR-4 PCB substrate. The photographs of the RF coil, the metasurface and dielectric phantom are illustrated in Fig. 3.27. The dielectric phantom used in this case contained 5L distilled water and 200g sodium chloride. The receiving probe was placed on the phantom surface, then the transmission coefficient between the RF coil and probe was obtained to make a comparison. Two RF coils were manufactured, and their resonant frequency was tuned to 63.85MHz, with the impedance matched for cases with the RF coil only case and with metasurface. When the metasurface was present, the tuning capacitance on the coil was 19.9pF with three capacitors in series, i.e. 100pF and 100pF and 33pF, and the matching capacitor was 15pF. When the metasurface was absent, the tuning capacitance on the coil was 28.3pF, with two capacitors in series, i.e. 200pF and

33pF, and the matching capacitor was 68pF.

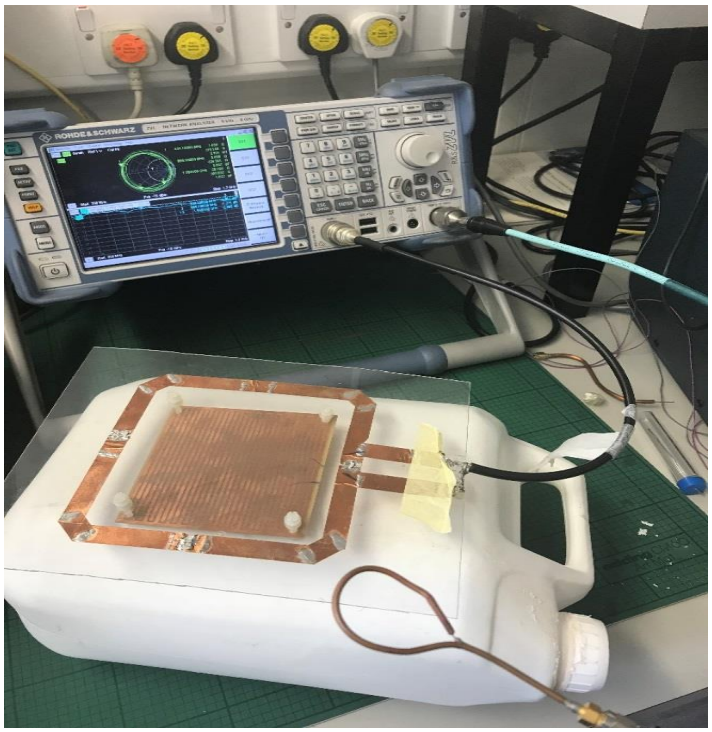

Fig. 3.27 The experimental set-up system in an RF bench

Fig. 3.28 shows the reflection coefficient (S_{11}) obtained from simulation and laboratory measurement. From the lab results, the metasurface provided a wider bandwidth compared with the case of RF coil only mainly due to the extra loss of the CIS. The difference between measured results and simulated results is caused by the different electromagnetic parameters of the dielectric phantom, and the tolerance in the fabrication.

From Fig. 3.29, the S_{21} at 63.85MHz was increased -4dB by adding the metasurface in the simulation and the laboratory measurement respectively. The S_{21} results obtained from the laboratory were worse than those from the simulation, because the simulation was conducted in an ideal environment, and some power were lost in the elements and transmission.

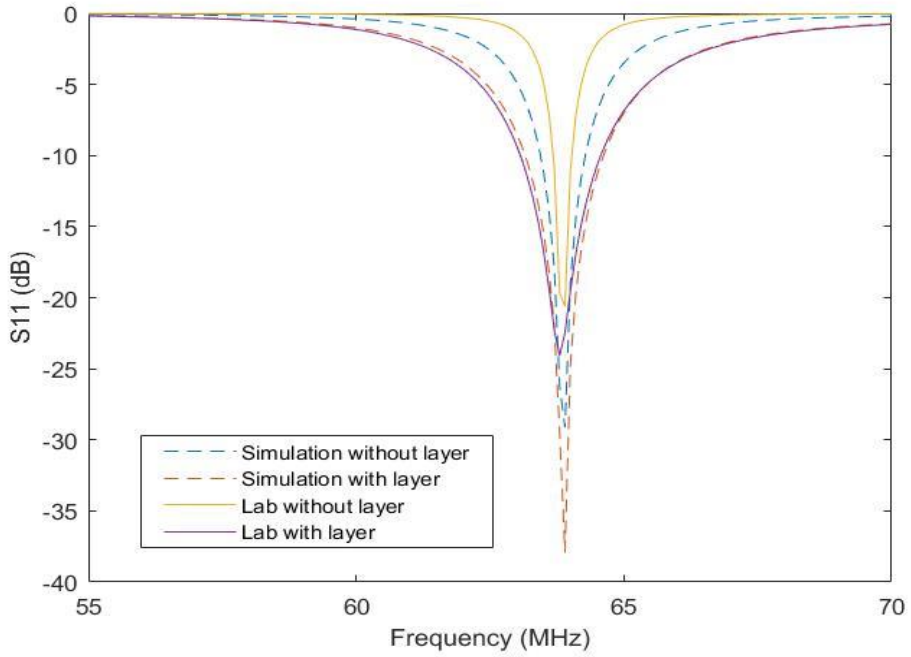

Fig. 3.28 Simulation and measurement results of the input match of RF coil

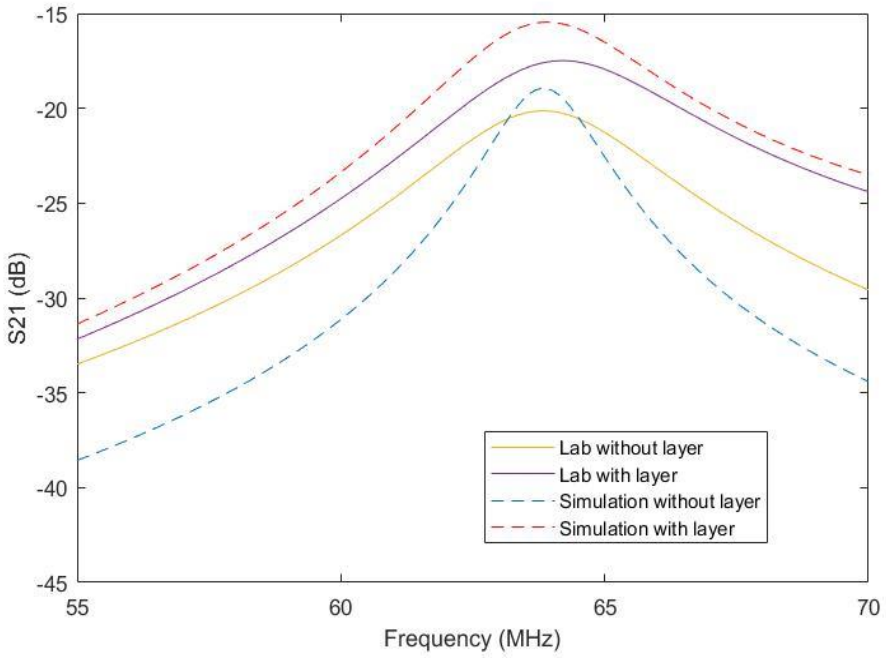

Fig. 3.29 Simulation and measurement results of the transmission coefficient of RF coil

3.7.2 Measure S-parameter and Q-factor in hospital's laboratory

Before testing the metasurface in the MRI scanner, the proposed RF measurement system was matched with the new dielectric phantom. The new dielectric phantom provided by the hospital had different electromagnetic parameters, so the RF coils for the case with or without the metasurface should be tuned and matched again. Fig. 3.30 gives the S_{b1} results, which show the RF coils had been tuned again for the cases with or without the metasurface. The tuning capacitance was 22.6pF with three capacitors in series, i.e.68pF, 68pF and 68pF, and the matching capacitor was tuned to 47pF when the metasurface was absent. The tuning capacitance was 13.3pF with three capacitors in series, i.e. 68pF, 68F and 22pF, and the matching capacitor was tuned to 33pF when the metasurface was present.

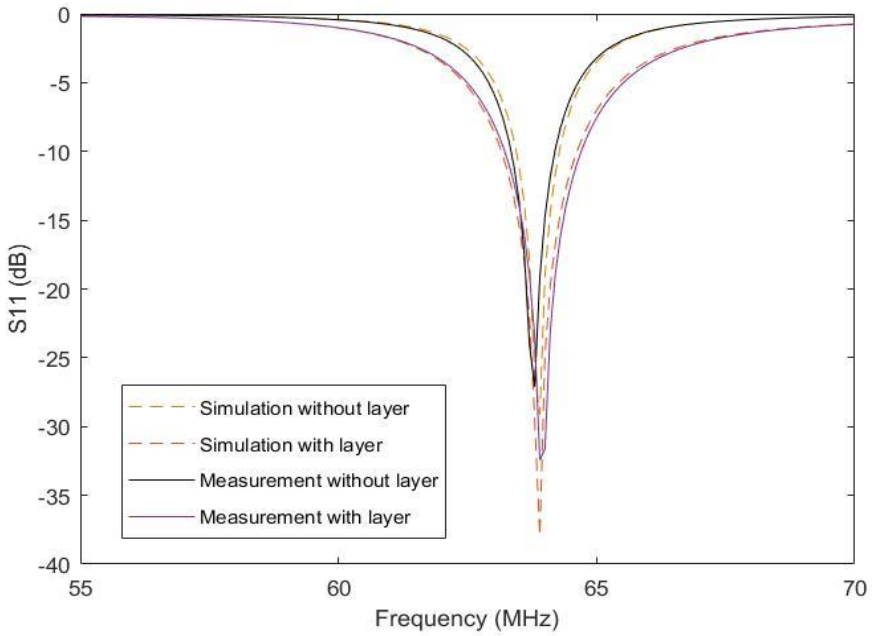

Fig. 3.30 Simulation and measurement results of the input match of RF coil

Fig. 3.31 presents the S_{21} results in the hospital bench. It was clearly observed that, the transmission performance of the RF coil in each case was changed again, due to the different electrical parameters of the new dielectric phantom. The metasurface showed better enhancement in transmission than the last case, and S_{21} was increased by -8dB

for this new phantom.

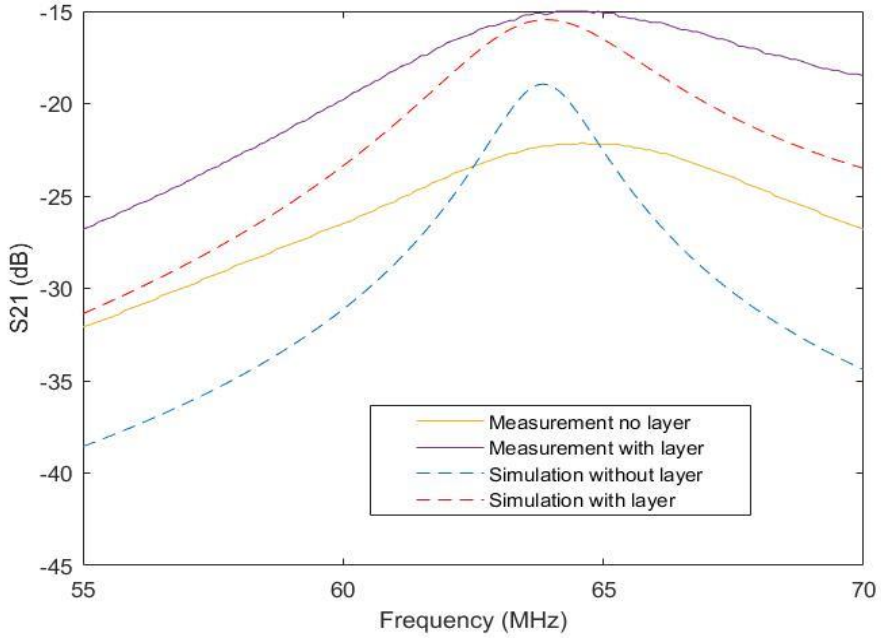

Fig. 3.31 Simulation and measurement results of the transmission coefficient of RF coil

Q-factor was also measured when measuring S-parameter to evaluate the performance of the RF coil. The Q loaded was measured when the dielectric phantom was present, and the Q unloaded was measured when the dielectric phantom was removed. The Q factor in each case can be calculated by:

$$\mathrm{Q} = \frac{Storage\ power}{Dissipated\ power} = \frac{\omega L}{R} = \frac{f_0}{\triangle f} \qquad (3.10)$$

where $\omega = 2\pi f_0$, f_0 is the resonant frequency, and $\triangle f$ is a -3 dB bandwidth of the RF coil. The Q ratio is the ratio of Q unloaded and Q loaded. Then, the rate of the SNR compared to the maximum value can be obtained by:

$$Q_{ratio} = \frac{Q_{unloaded}}{Q_{loaded}} \qquad (3.11)$$

$$\frac{SNR}{SNR_{max}} = \sqrt{1 - \frac{1}{Q_{ratio}}} \qquad (3.12)$$

Table 3.5 gives the results of Q-factor measured for both cases. According to Eq. (3.12), the SNR in both of the RF coils with and without the metasurface is more than 80%, which a satisfying result compared with the SNR_{max}. It should be noticed that, the SNR_{max} results is define the maximum SNR of the coil can be achieved when it loaded with a dielectric phantom compared with itself when it is unloaded, and define the quality of the coil.

	Q-unloaded	Q-loaded	Q-ratio	SNR ratio
Single RF coil	110	35.48	3.1	82.3%
RF coil with metasurface	67	23.93	2.8	80.2%

Table 3.5 The measured Q-factor with and without the metasurface

3.8 Results from the MRI scanner

Fig. 3.32 shows the proposed RF measurements system in the 1.5T MRI scanner, when the RF surface transceiver working with a metasurface. The key parameters of the MRI system used for measurement are listed in Table 3.6. All measurements were carried out with a fixed power of 160W. The x-axis was across the phantom, and the y and z-axis were on the horizontal surface of the phantom.

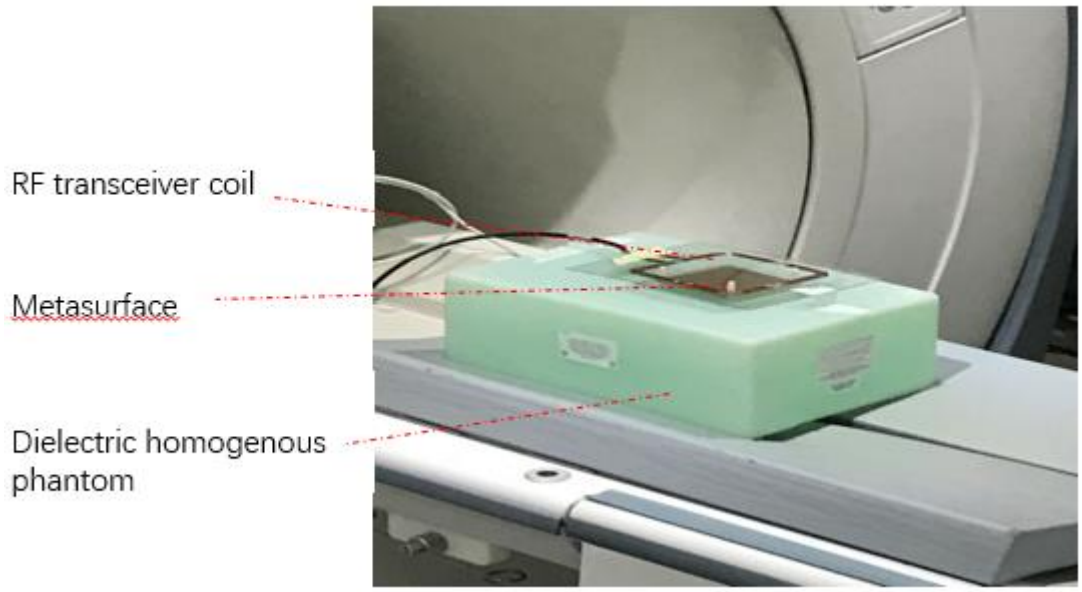

Fig. 3.32 The proposed RF measurement system in a 1.5 T MRI scanner

Parameter	Value
Pulse repetition time (ms) TR	500
Echo time (ms) TE	50
Band width (kHz)	15.63
Field of view (cm)	32x32
Slice thickness (mm)	10
Acquisition matric (pixels)	128x128
Spoil gradient echo	2D spoil gradient echo

Table 3.6 Key parameters of the MRI system

3.8.1 SNR

In this case, all the results from the 1.5T scanner were processed in Matlab. Fig. 3.33 provides the SNR at the coil centre along the x-axis which represents penetration depth. The highest points of two lines indicate the SNR on the phantom surface. It was clear that the SNR was increased from 590 to 1430 after adding the metasurface between the RF transceiver and dielectric phantom. The enhancement in SNR covered the whole penetration depth from 0mm to 100mm.

According to [88], metamaterial shows good performance in focusing the magnetic field, but it might have the risk of destroying the homogeneity of magnetic field, which would influence the image quality. Fig. 3.34 shows the SNR along the y-axis when x=25mm, z=0mm, which represents the SNR on the phantom surface. As can be seen, the metasurface had the similar smooth field as single the case of RF transceiver.

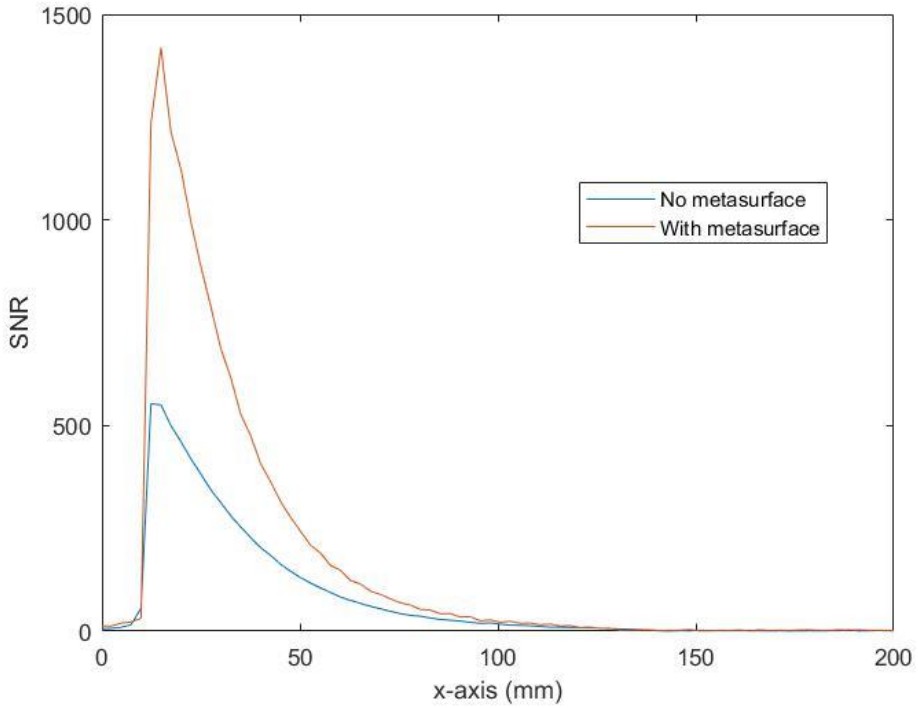

Fig. 3.33 Measured transceiver SNR at the centre (y=z=0) along x-axis

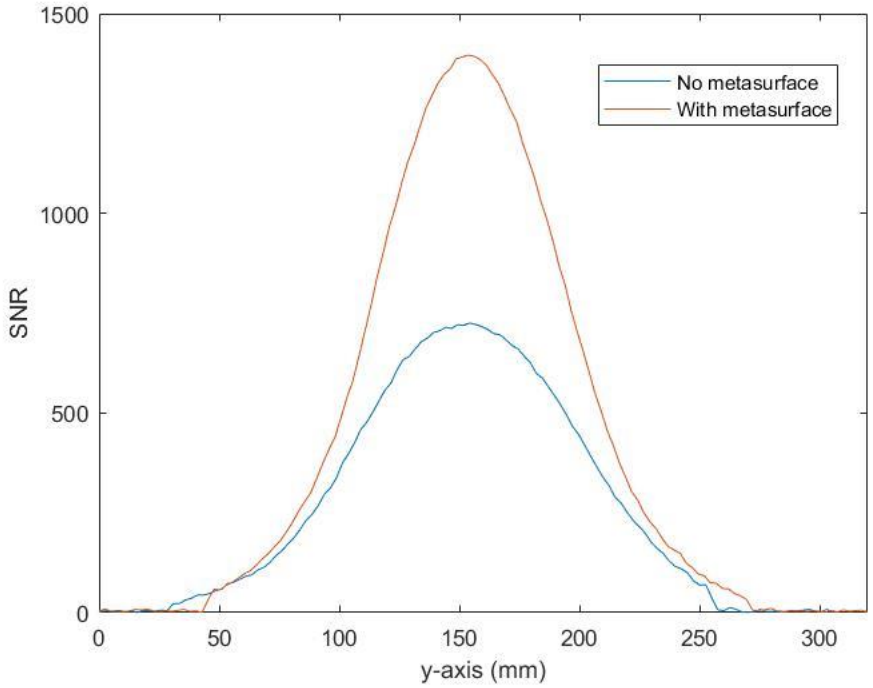

Fig. 3.34 Measured transceiver SNR on the phantom surface (x=25 mm, z=0 mm) along y-axis

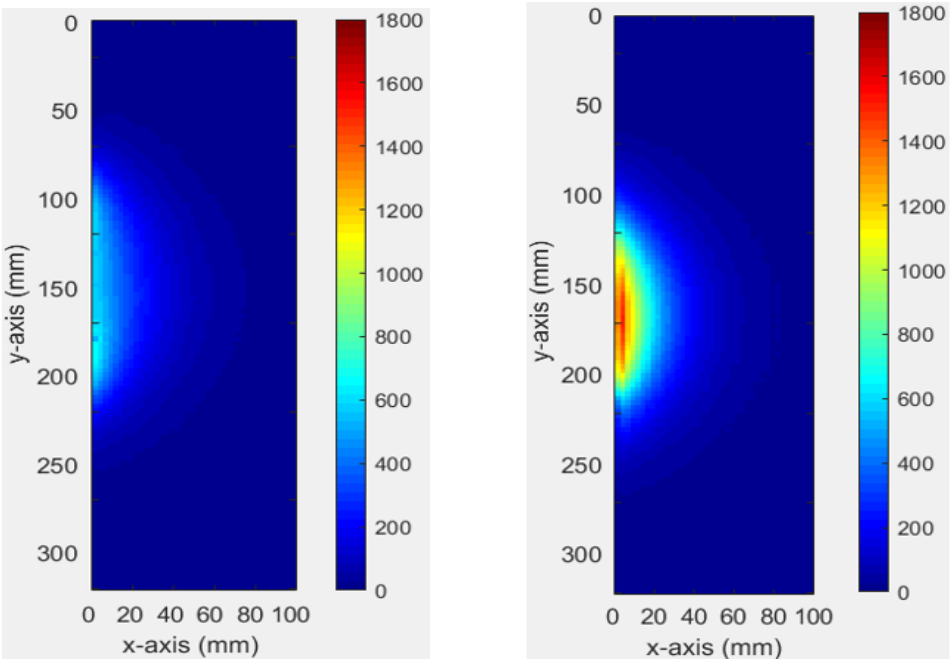

(a) (b)

Fig. 3.35 (a) Measured transceiver SNR at the centre (z=0), without metasurface. (b) Measured transceiver SNR at the centre (z=0), with metasurface

Fig. 3.35(a) and Fig. 3.35(b) show the SNR when the metasurface was absent and present, respectively. It could be clearly seen that the SNR could be improved significantly by adding the metasurface between the RF transceiver and phantom. The homogeneous field was also obtained after adding the metasurface, which was beneficial for the final imaging procedure.

3.8.2 Flip angle

The enhancement provided by the metasurface can be also defined by the flip angle α. According to MRI theory [86], when the external magnetic field B_1 is applied into the static field B_0, the magnetization vector M_0 will be rotated with an angle, which is called flip angle α. We have:

$$\mathrm{SNR} \approx \frac{|\sin(\gamma B_1^+ \tau) B_1^-|}{\sqrt{P_{abs}}} \qquad (3.13)$$

where $\frac{|B_1^-|}{\sqrt{P_{abs}}}$ is represent by the receiver sensitivity Rx. Eq. (3.12) can be transformed as:

$$\sin(\gamma B_1^+ \tau) = \frac{SNR}{R_x} \qquad (3.14)$$

If $\alpha = \gamma B_1^+ \tau$,

$$\alpha = \mathrm{asin}\left(\frac{SNR}{R_x}\right) \qquad (3.15)$$

where τ is the RF pulse duration, γ is the geometric ratio, and B^+_1 is the magnetic flux density generated by the RF transceiver in this case. Therefore, increasing the value of

α will increase the magnitude of $|B_1^+|$, which is proportional to the transmission efficiency.

Fig. 3.36(a) and Fig. 3.36(b) illustrate the flip angle maps without and with the metasurface respectively. It was clear that the flip angle decayed at the resions away from the phantom surface, and the maximum flip angle was at the centre of the metasurface. The long penetration depth and homogeneity provided by the metasurface was proved again.

In addition, the flip angle is directly proportional to the $|B_1^+|$, and the improvement in flip angle in percentage was expressed in Eq. (3.16) which describes the transmission efficiency of the transceiver

$$\eta(x,y) = \frac{\alpha_w(x,y) - \alpha_{wt}(x,y)}{\alpha_{wt}(x,y)} \times 100 \qquad (3.16)$$

where $\alpha_w(x,y)$ is the flip angle of the case with the metasurface, and $\alpha_{wt}(x,y)$ is the flip angle of the case without the metasurface.

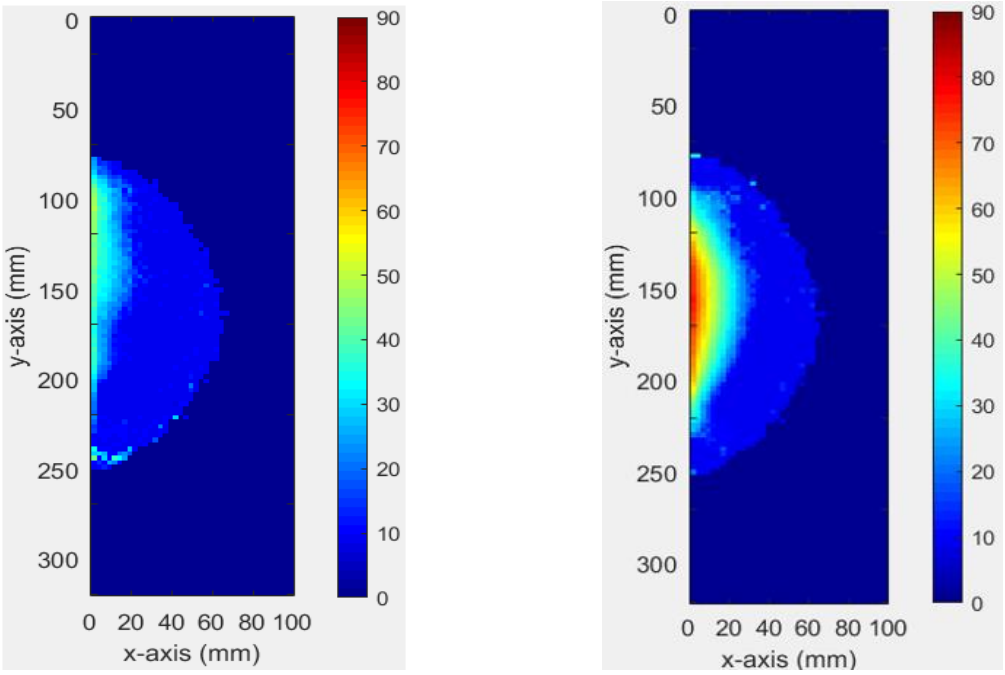

(a) (b)

Fig. 3.36 Measured transceiver flip angle at the centre (z=0) (a) without the

metasurface, and (b) with the metasurface

Fig. 3.37 shows the percentage of the improvement in the flip angle, which also describes the enhancement in the transmission efficiency of the transceiver.

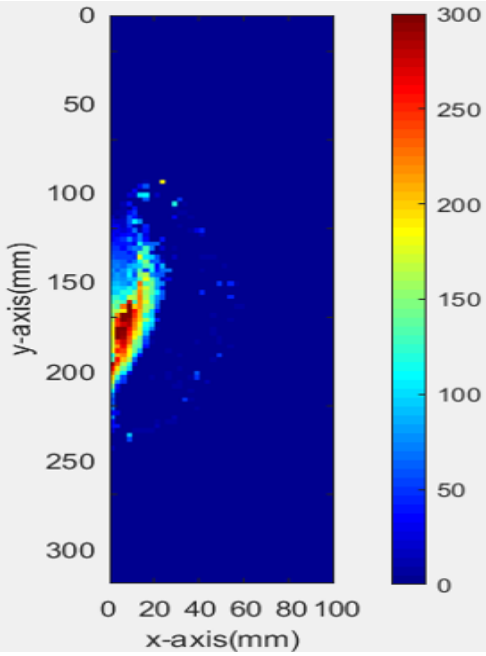

Fig. 3.37 The percentage of improvement in the flip angle at the centre (z=0)

3.8.3 Receiver sensitivity

The receiver sensitivity in 2D Ψ(x,y) which is proportional to the $|B_1^-|/\sqrt{P_{abs}}$ can be estimated by:

$$\psi_D(x,y) = \frac{SNR_D(x,y)}{\sin(\alpha_D(x,y))} \qquad (3.17)$$

$$\psi_S(x,y) = \frac{SNR_S(x,y)}{\sin(\alpha_S(x,y)(\frac{\alpha\ g_D}{\alpha\ g_S}))} \qquad (3.18)$$

where SNR_D and SNR_S are the SNR of the RF coil with the metasurface and the single tuned coil without the metasurface, respectively; α_D and α_S mean the flip angle for the RF coil with the metasurface and the single tuned coil, respectively. As investigated in subsection 3.8.2, the case with worse SNR always had smaller flip angle. Therefore, the global flip angle for the case without the metasurface was modified by the global flip angle ratio $\frac{\alpha g_D}{\alpha g_S}$ to provide a fair comparison. Fig. 3.38(a) and Fig. 3.38(b) provide the 2D results of the receiver sensitivity when the metasuface was absent and present, respectively. It can be observed that the metasurface also improved the receiver sensitivity without any destruction effects in the field.

The percentage of improvement in the receiver sensitivity can be calculated by:

$$\triangle \Psi = \frac{\Psi_w - \Psi_{wt}}{\Psi_{wt}} \times 100 \qquad (3.19)$$

where Ψ_w is the receiver sensitivity when the metasurface is present, and Ψ_{wt} is the receiver sensitivity when the metasurface is absent.

Fig. 3.39 illustrates the percentage of the improvement in receiver sensitivity by adding the metasurface at the centre, when z=0. The improvement around the centre area can be understand more clearly by observing the improvement in the flip angle in Fig. 63. The large improvement in the flip angle around the centre area caused obvious decrease in the receiver sensitivity.

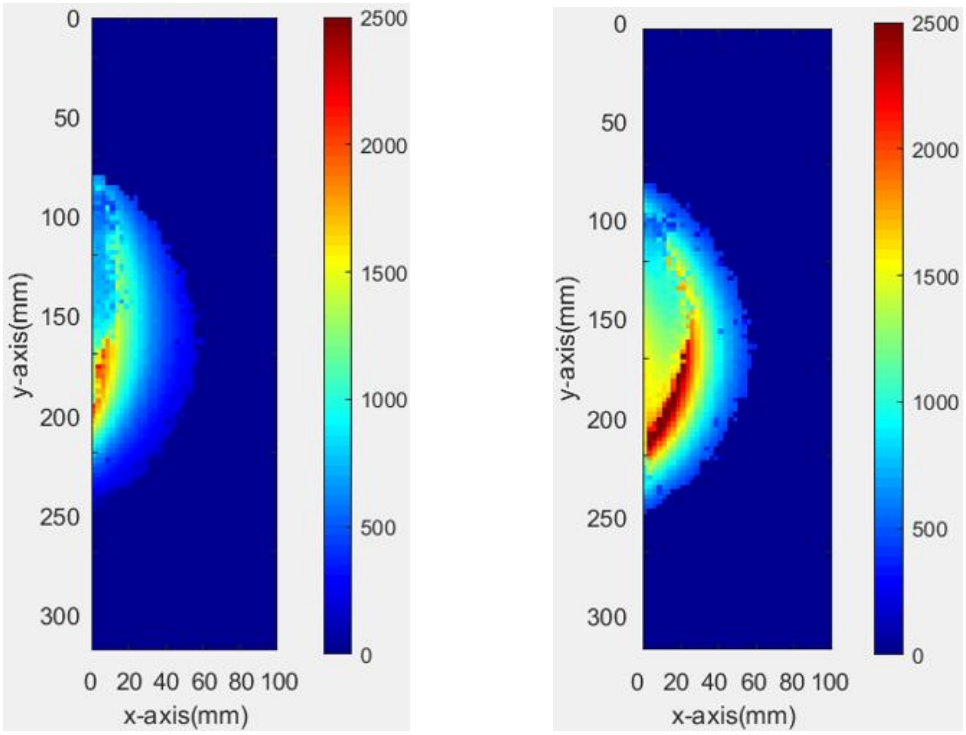

(a) (b)

Fig. 3.38 Measured receiver sensitivity at the centre (z=0) (a) without the metasurface and (b) with the metasurface

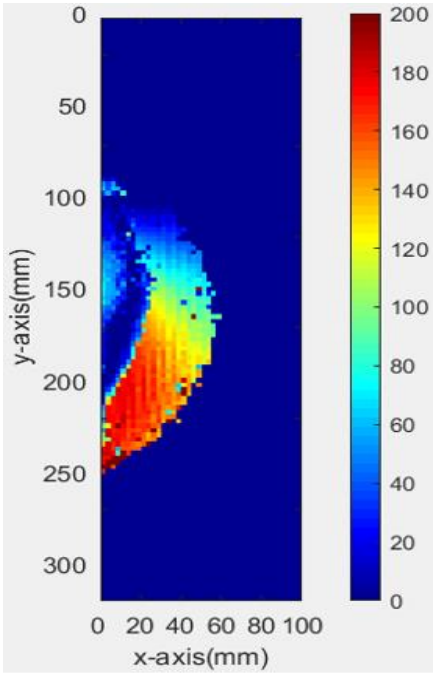

Fig. 3.39 The percentage of improvement in the receiver sensitivity at the centre (z=0)

3.9 Summary

In this chapter, a non-periodic and high-capacitance metasurface was developed for enhancing the SNR for 1.5T MRI systems and it was tested through numerical and experimental techniques. In the simulation, the positive magnetic flux density $|B_1^+|$ was improved by about 65% at the centre on the dielectric phantom surface, when the metasurface of w_d=1.8mm, g_d=0.8mm, l=80mm was placed between the RF coil and the dielectric phantom. This enhancement covered the whole penetration depth, which solved a problem of short penetration depth in some previous researches. Further, from the results of B_1^+, it was found there was no obvious relationship between the $|B_1^+|$ and the metasurface capacitance, because the electromagnetic property of the non-periodic structure depended more on the parameters of the strip lines on the layer surface. The negative flux density B_1^- were also investigated, which is normalised to the root of the absorbed power of the whole system corresponding to Eq. 1.6. The normalised magnetic flux density $|B_{1\ nor}^-|$ was improved by about 67% on the dielectric phantom surface, and this enhancement covered the whole dielectric phantom. In this case, the $|B_{1\ nor}^-|$ along the y-axis on the dielectric phantom surface was also investigated. The $|B_{1\ nor}^-|$ around the central area was increased by 60%, but this enhancement decreased the magnitude around the edges of the phantom. This property of the metasurface was highlighted again from the results of electric field. From the 2D results of the electric field, when the dimension of the metasurface was close or larger than the diameter of the RF coil, the electric field was localised by the metasurface. This property of the metasurface could help to focus the field to improve the SNR, but the enhancement in electric field also increased the value of SAR describing the electromagnetic energy absorbed by the biological tissue when exposed to an RF magnetic field. Although the SAR of all the metasurface designs satisfied the standard IEC60604-2-33/2010, there should always be a trade-off between the enhancement in SNR and SAR.

Next, the metasurface of w_d=1.8mm, g_d=0.8mm, and l=80mm was manufactured successfully. The metasurface was tested with the RF coil which was made by copper tape in the RF bench, by combining with a phantom full of saline firstly. The RF coils

showed high quality (proved by the results of Q factor), and good transmission performance (proved by the results of S_{21}). Then the RF coils were retested in the hospital's laboratory with the dielectric phantom consisting of $CuSO_4$, which has more accurate electromagnetic parameter with human body. The results of S_{21} obtained in this case were different from simulation results and the results from the RF bench. This proved that the phantom with different electromagnetic parameter was a factor influencing the transmission performance of the RF coil. Finally, the results of MRI measurements in the 1.5 T MRI scanner was processed in Matlab. From the SNR results along the x-axis, the SNR on the phantom surface was improved by 133% when the metasurface was present, and the enhancement provided by the metasurface covered the whole penetration depth. From the SNR results along y-axis on the phantom surface, the SNR around two edges were not decreased, as the dimension of the manufactured metasurface was smaller than the diameter of the RF coil. The SNR was decayed uniformly inside the dielectric phantom, which could not be achieved by periodic structure, and helped MRI scanner to obtain good-quality images.

In the Table 3.7, the enhancement provided by the non-periodic metasurface is compared with previous researches, which improved MRI systems by metamaterials in different types. It was found that, the non-periodic metasurface shown a significant improvement in the B_1 and SNR, especially the penetration depth is much better than using other types. The SAR describes the safety of the MRI system in this case is lower than other cases for enhancing RF system, which means the safety of the system is better. The SAR by using HIS is negative, because HIS improve the MRI system by optimizing the shield plane.

Parameter	Metamaterials type	1.5 T MRI	3-4.6 T MRI	7 T MRI
$\|B_1^+\|$	High impedance surface	10%[66]	-	7%[89]
	RF lens	-	-	-
	Dielectric pads	-	50%[90]	100%[81]
	Non-periodic metasurface	**65%**	**-**	**-**
SNR	High impedance surface	6%[66]	-	-
	RF lens	100%[91]	200%[91]	-
	Dielectric pads	-	20-40%[90]	53%[92],200%[81]
	Non-periodic metasurface	**133%**	**-**	**-**
Penetration depth	High impedance surface	20mm[66]	-	-
	RF lens	35mm[91]	38mm[91]	-
	Dielectric pads	-	-	-
	Non-periodic metasurface	**>100mm**	**-**	**-**
SAR	High impedance surface	-10%[66]	-	-48%[69]
	RF lens	-	-	-
	Dielectric pads	-	+50%[90]	+33%[92]
	Non-periodic metasurface	**+20%**	**-**	**-**

Table 3.7 Comparison between using the non-periodic metasurface against the methods from published literature

Chapter 4

The investigation of the dual-band property of non-periodic metasurface for 1.5 T MRI applications

4.1 Introduction

In the last chapter, a non-periodic metasurface is proposed to enhance B_1^+ to further increase the SNR of 1.5T MRI RF transceiver systems. It has been found that there was an extra frequency band appears in the higher frequency when the metasurface is present. How to tune this extra resonant frequency and match its impedance at the focused frequency is the main purpose of this chapter. With the development of biological imaging technology, an increasing number of nuclei have been used to image different organs in the human body. For example, human metabolism can be imaged by ^{31}P using high energy phosphates[1][2]. The information of the balance of glucose and

glycogen can be provided by ^{13}C[3][4][5]. The detection of tumorous tissues or cartilage can be achieved by ^{23}Na. [6][7][8] Therefore, multi-nuclei imaging becomes a high-efficiency and advanced imaging method. Parallel imaging is the most popular way to image several nuclei simultaneously, but it requires different imaging instructions and long imaging time. The works based on achieving or optimizing multi-nuclei MRI systems have been discussed in chapter 2. At present, the existing research on applying metamterial to multi-nuclei MRI is based on useing a periodic structure, and it could only be used in high-field-strength (7T) systems due to the limitation of size.

In this chapter, the dual band property of non-periodic metasurfaces is investigated to achieve fluorine nuclei (^{19}F) imaging (resonance frequency of 60.08MHz) and hydrogen nuclei (^{1}H) imaging (resonance frequency of 63.85MHz) for 1.5T MRI systems. As far as we know, this is the first time to achieve multi-nuclei imaging by using the metasurface with a dual loop coil with a single RF fed. Compared with the latest metasurfaces used in multi-nuclei imaging, the metasurface with non-periodic structure proposed in this case has much simpler and smaller structure, which simplifies the manufacturing and reduces the cost, and can be used in low field strength MRI systems. Furthermore, the even decay of the field provided by RF coil can be obtained by the non-periodic metasurface, while it can hardly be achieved by most periodic structures. In Section 4.3, the dual band property of the metasurface with non-periodic structure is investigated to determine the factors that can tune the frequency bands. In Section 4.4, the dual loop coil is proposed to tune the resonant frequencies independently, and the relationship between the capacitance on coils and the resonance frequency is obtained. The final design of the metasurface is determined by comparing the results of S-parameter, B_1^+ and normalized B_1^-.

4.2 MRI configuration

Numerical simulation was conducted in CST Microwave Studio 2015 in frequency domain. The key components used to model an MRI RF transceiver system is demonstrated in this section. The RF coil was fed by a 1W and 50Ω signal source. Fig.4.1 provides the cross section of the MRI scenario used in CST simulation, which consists of an RF coil, a non-periodic metasurface and a double-layer dielectric phantom to model human tissue and lungs The dielectric phantom consists of two same-size layers. The first layer is a 20mm-thick high-permittivity material with σ_H=0.4S/m and ε_H=63 to model an ^{1}H region. The second layer is also 20mm thick with σ_F=0S/m and ε_F=1 to model an ^{19}F region. The size of both phantoms is 20mm×230mm×335mm.Fig. 4.1(a) and Fig. 4.1(b) show the cross section when the metasurface is absent and present, respectively.

An RF transceiver coil was placed a distance of H away from the double-layer dielectric phantom mimicking a biological sample in the absence of the metasurface. In the presence of the metasurface, the space between the dielectric phantom and the metasurface is defined as S, and the distance between the RF coil and the metasurface is D. In order to measure the transmission coefficient (S_{21}) to compare the transmission performance in each case, an electrically small receiving probe with diameter of 6 mm was placed on the back surface of each phantom in different focused nuclei cases, so that the dual band property could be observed more clearly. The receiving probe was removed when conducting other tests, in order to prevent any electromagnetic effects from the probe.

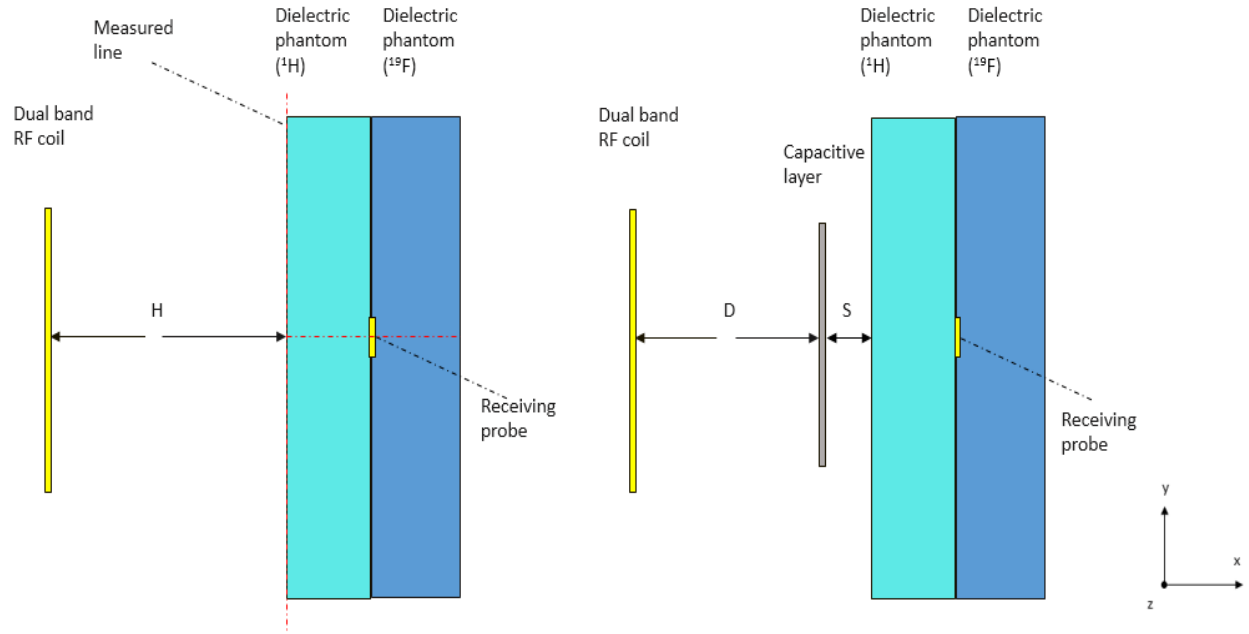

(a) (b)

Fig. 4.1 Cross section view of the MRI system. (a) RF coil only. (b) With metasurface

Furthermore, two red dash lines are used to measure the tested parameter such as magnetic field across the dielectric phantom, i.e. the line along *x*-axis (*x* is from 25mm to 65mm, *y*=*z*=0mm), and the line along *y*-axis (*y* is from -100mm to 100mm, *x*=25mm, *z*=0mm).

4.3 The dual band property of the metasurface

In Chapter 3, the metasurface with w_d=1.8mm, g_d=0.8mm and l=80mm was proposed to improve the SNR by increasing B_1 field, where the metasurface was placed between the RF coil and the dielectric phantom, and the resonance frequency of the RF coil was tuned to 63.85MHz. The S_{11} result of the RF transceiver system combined with this metasurface is shown in Fig. 4.2. It is obvious that an extra resonance frequency was generated at 92MHz, but the impedance matching was poor. How to tune this extra resonance frequency and match its impedance at the focused frequency bands becomes the main purpose of this chapter.

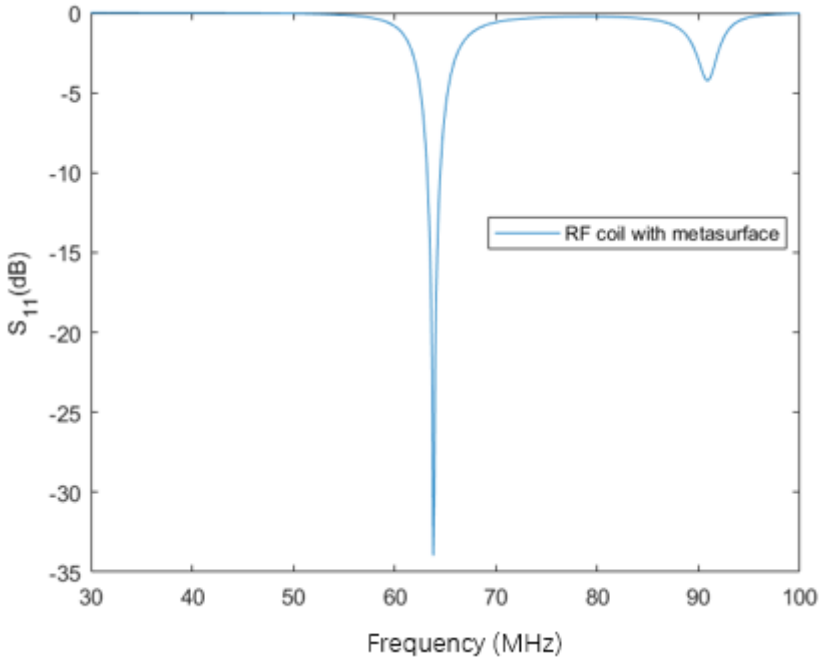

Fig. 4.2 Dual band property of the non-periodic metasurface

4.3.1 Effects of the distance between components

In this subsection, the relationship of the spacing between each component is investigated, in order to define the extra resonance frequency from the coupling between components. Fig. 4.3, Fig. 4.4 and Fig. 4.5 give the S_{11} results with D, S, and H independently changing. The resonance frequency of the RF coil was tuned to 63.85MHz in each case.

As illustrated in Fig. 4.3, when D was increased from 15mm to 30mm, the second resonance frequency was decreased from over 100MHz to 87MHz. This decrement in the frequency was decayed gradually, when the RF coil was placed further and further away from the metasurface. According to Fig. 4.4, when the S was increased from 5mm to 15mm, the second resonance frequency was increased from 92MHz to 100MHz. It should be noticed that, D was decreased when S was increased, because the position of the RF coil was fixed when the metasurface was moved away from the phantom and close to the RF coil. When H was adjusted, the RF coil and the metasurface were moved

together, so D was kept constant in this case. Fig. 4.5 indicates that no effect was applied to the second resonance frequency when H was changed.

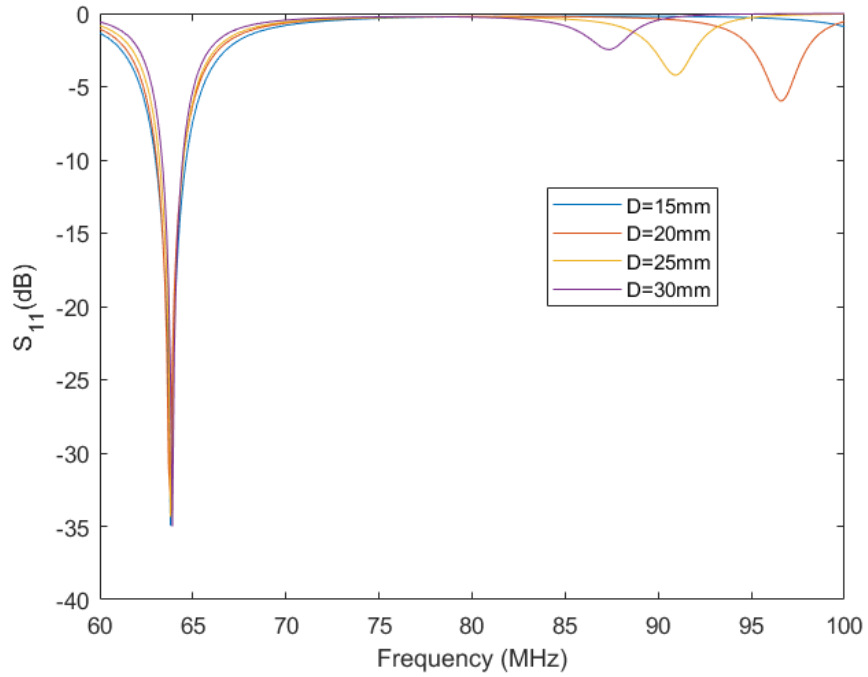

Fig. 4.3 Simulated S_{11} result when D was changed

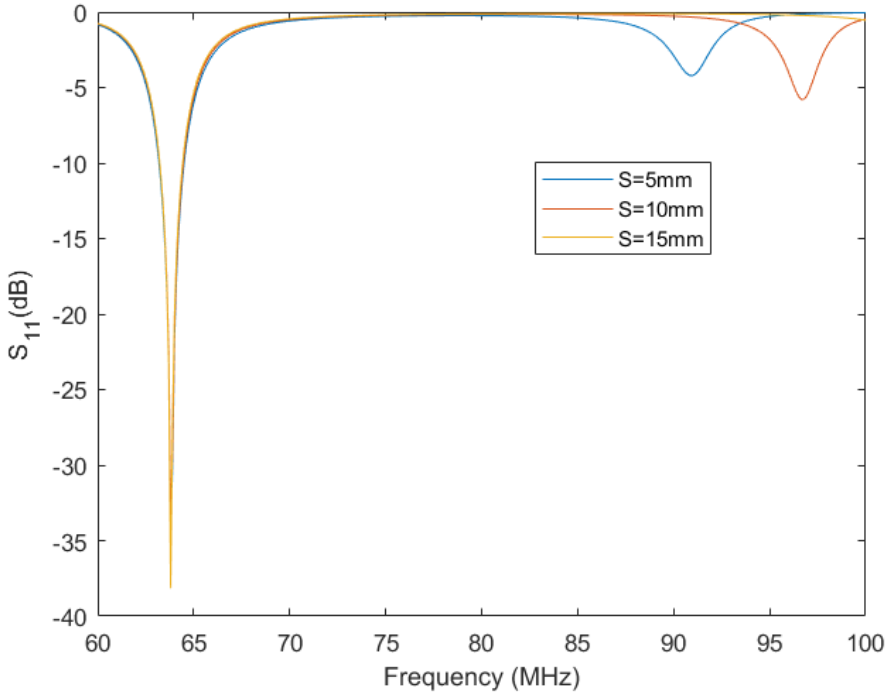

Fig. 4.4 Simulated S_{11} result when S was changed

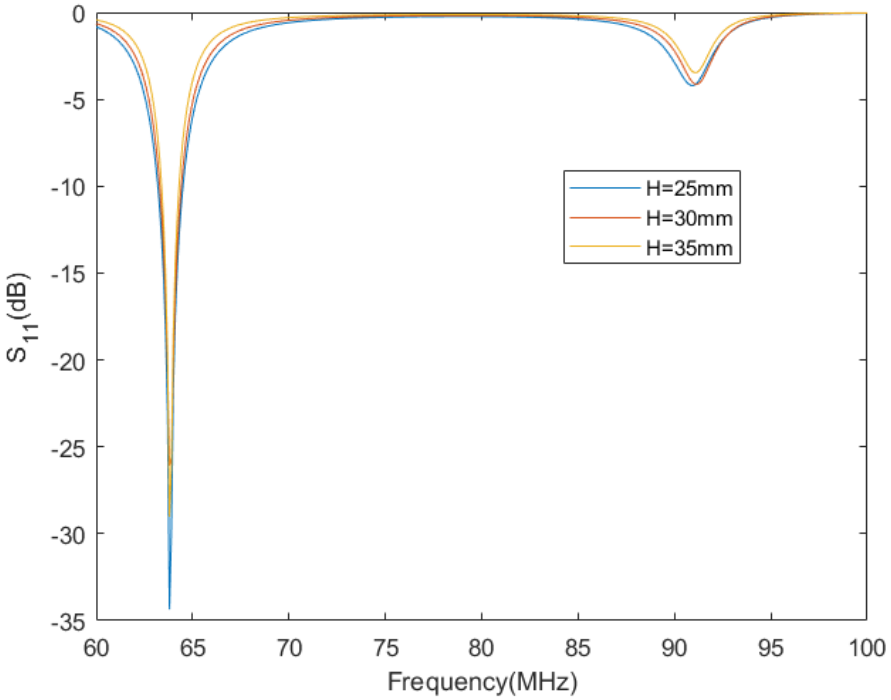

Fig. 4.5 Simulated S_{11} result when H was changed

From these results, it can be found that, when D was fixed, the second resonance frequency would be kept constant. The spacing between the RF coil and the dielectric phantom, and the spacing between the metasurface and phantom had no effect on the position of the second resonance frequency. When the spacing between the RF coil and the metasurface was increasing (by increasing D or reducing S), the resonance frequency was decreased. When the spacing between the RF coil and the metasurface was decreasing (by decreasing D or increasing S), the extra resonance frequency was increased. Therefore, the extra resonance frequency was generated by the coupling between the RF coil and the metasurface, and the resonance frequency was based on the distance between the RF coil and the metasurface. However, we expect the second resonance frequency to be tuned to 60.08MHz for ^{19}F imaging. When S=5 mm and D=25 mm, the second resonance frequency was at 87MHz, which was far away from 60.08MHz. Then, it was hard to tune the second resonance frequency by keeping increasing D, because the transmission performance would be significantly reduced when the RF coil was very far away from the dielectric phantom. Further tuning work

by adjusting the dimension of the metasurface is demonstrated in subsection 4.3.2.

4.3.2 Effects of the dimension of the metasurface

Fig. 4.6 indicates that, when w_d and g_d were kept as 1.8mm and 0.8mm, respectively, *l* was increased from 60mm to 100m, and the second resonance frequency decreased significantly. The matching capacitor C_m on the coil could only match the impedance to one resonance frequency only, so the other resonance was always matched in a poor manner. Fig. 4.7 shows the relationship between the width of the strip lines of the metasurface w_d and the second resonance frequency, with *l*=80mm, g_d=0.8mm, and the resonance frequency of the metasurface tuned to 63.85MHz. It is clear that, when w_d was increased, the second resonance frequency would be increased a little. Although the effect of w_d on the second resonance frequency was not satisfying, the impedance matching got some improvements. Fig. 4.8 provides the S_{11} results when g_d was adjusted from 0.2mm to 0.8mm, *l* and w_d were kept at 80mm and 1.8mm. When the gaps between each strip line were increased, the second resonance frequency would be increased a little.

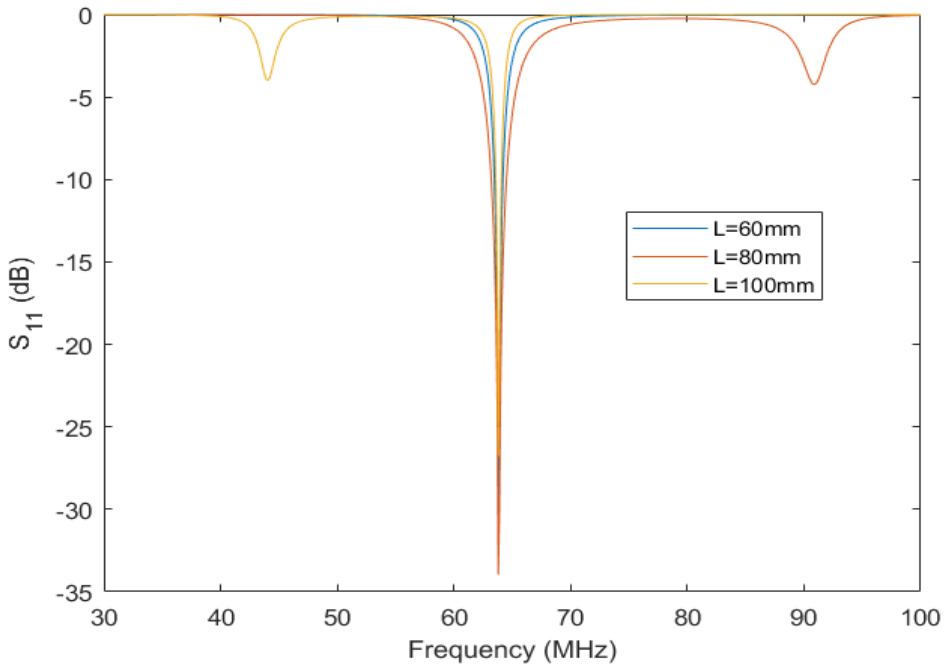

Fig. 4.6 Simulated S_{11} result when l was changed

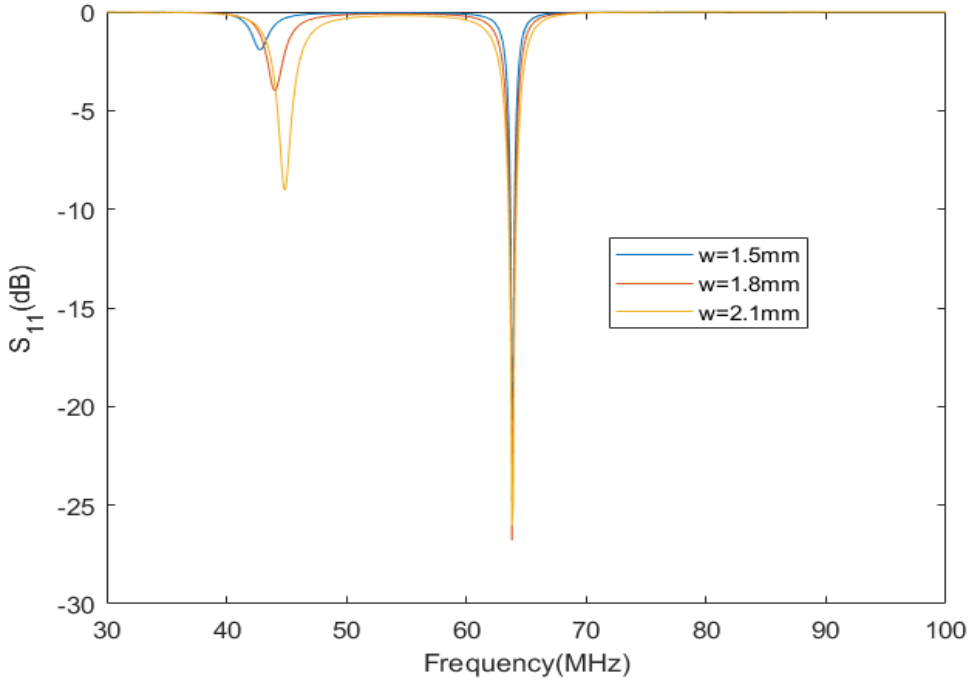

Fig. 4.7 Simulated S_{11} result when wd was changed

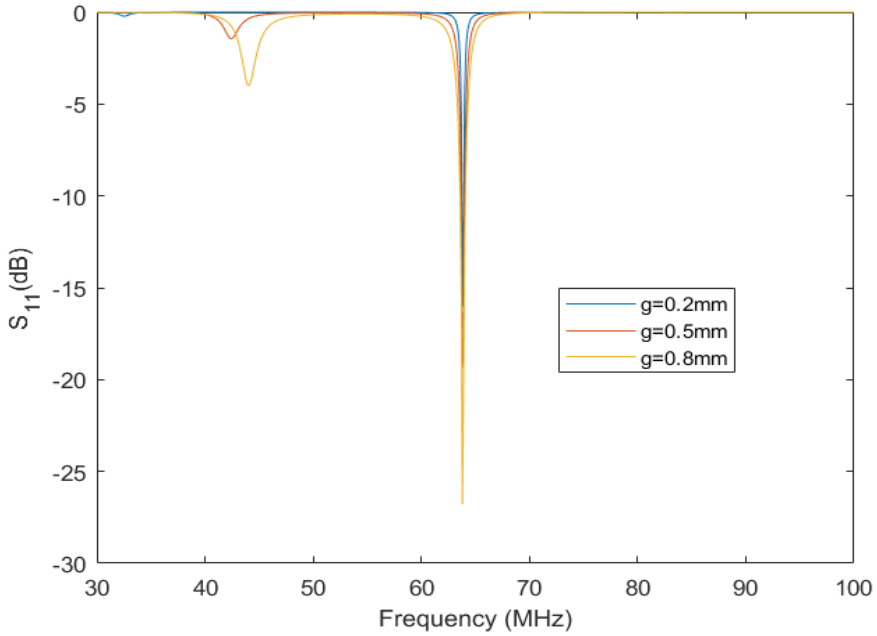

Fig. 4.8 Simulated S_{11} result when gd was changed

We can see the second resonance frequency was very sensitive to the change in *l*. However, this may cause some difficulties during the manufacturing and measuring process. From Chapter 3, it was found that when the shape or filler of the dielectric phantom was changed, the resonance frequency of the RF coil would change under different dielectric parameters of the dielectric phantom and different power losses during the measurement esonance frequency. The tuning on the RF coil would control both resonance frequencies. Thus, it is hard to tune the extra resonance frequency by the dimension of the metasurface in multi-nuclei application, because the resonance frequencies cannot be tuned independently. In the research[9], the authors solved this problem by combining two metasurfaces with different periodic structures to control the focused bands separately, but its periodic structure determined that it could only be used in high-field-strength MRI systems. The length of long metal resonator is 434mm for ^{1}H imaging at 300.1MHz for 7.05T MRI systems.

4.4 Further optimization in tuning work by using dual loop RF coil with single fed

Previous research shows that multi band could be achieved by adding extra RF loop and fed to produce extra resonance. For example, researchers developed 4T dual-tuned RF using dual loop coils to produce the bands at 45MHz and 170.2MHz for ^{23}Na and ^{1}H imaging, respectively, in 4T MRI systems, and the coupling between the two loops was improved by adding trap circuits. [83]Two RF feds were applied on each coil, so two resonance frequencies could be tuned separately by the tuning capacitors on each coil loop.

In this case, the additional surface coil was considered to tune the extra resonance frequency. During the simulation, it was found that an extra resonance frequency could be obtained by adding metasurface, so the RF fed on the second loop was removed.

The single fed dual loop RF coil was replaced by the dual loop coil with single RF fed. The RF coil was also chosen to be rectangular. Fig. 4.9 shows the dimensions of the proposed dual loop RF surface coil. The outer coil is 120mm×120mm for single tuned surface coil. The additional inner coil is 80mm×80mm. There is only one fed point, which is at the terminal of the outer coil. The outer coil includes a tuning capacitor C_{t1}, and the inner coil includes a tuning capacitor C_{t2}, and there is a matching capacitor C_m on the outer coil. Different from the double tuned RF coils, such as the double-tuned RF surface coil for MRI imaging of rat brains using interleaved ^{1}H and ^{23}Na, there is only one fed connected to the dual-loop coil used, and there is no extra trap circuit required to solve the coupling between the two coil loops.

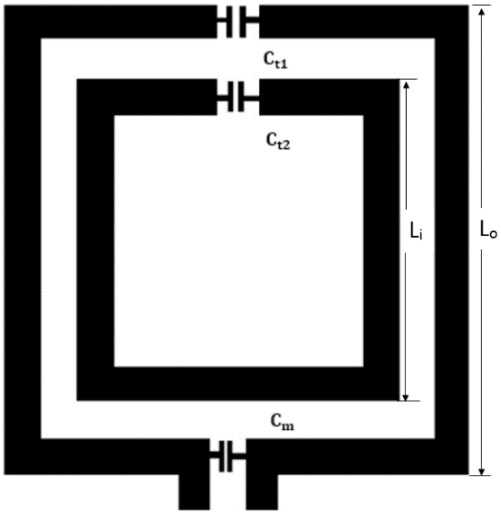

Fig. 4.9 Dual loop RF coil with single fed

4.4.1 Effects of the tuning capacitors on the dual loop coil

This subsection investigates the effects of the tuning capacitors on the outer coil C_{t1} and the inner coil C_{t2} resonance frequencywith the metasurface of w_d=1.8mm, g_d=0.8mm, and l=80mm placed between the dual loop coil and the phantom. Fig. 4.10 and Fig. 4.11 show the S_{11} results when adjusting the C_{t1} and C_{t2}, respectively.

From Fig. 4.10, adjusting the lumped capacitor C_{t1} did not result in independent tuning of the two resonance frequencies, and increasing the value of C_{t1} would reduce the frequency bands of both resonances. The change in the higher resonance frequency controlled by the mutual coupling between the RF coil and the phantom was not proportional to the capacitance of C_{t1}. Then, when C_{t1} was varied, there was a fixed gap between the two resonance frequencies, with C_{t1} greater than 30pF.

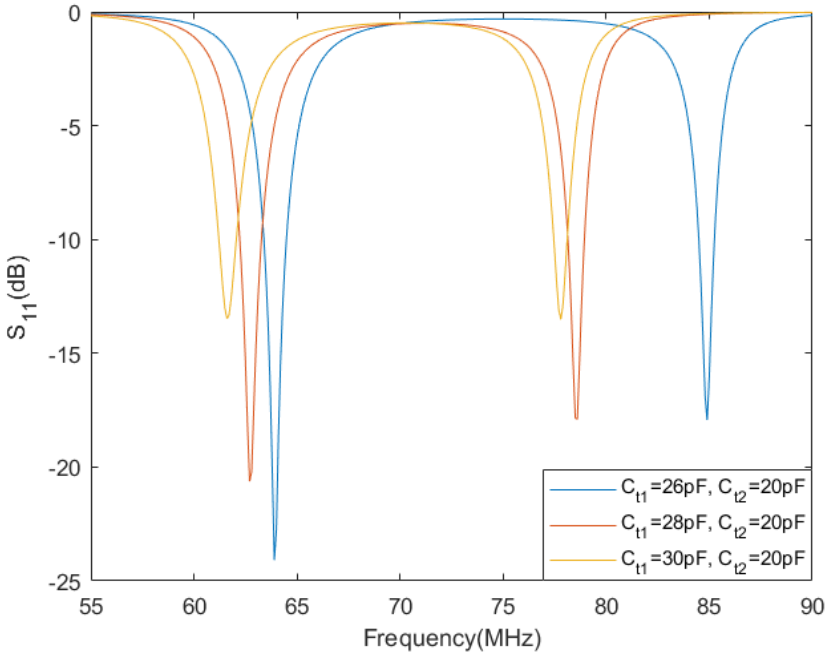

Fig. 4.10 Simulated S_{11} when C_{t1} was changed

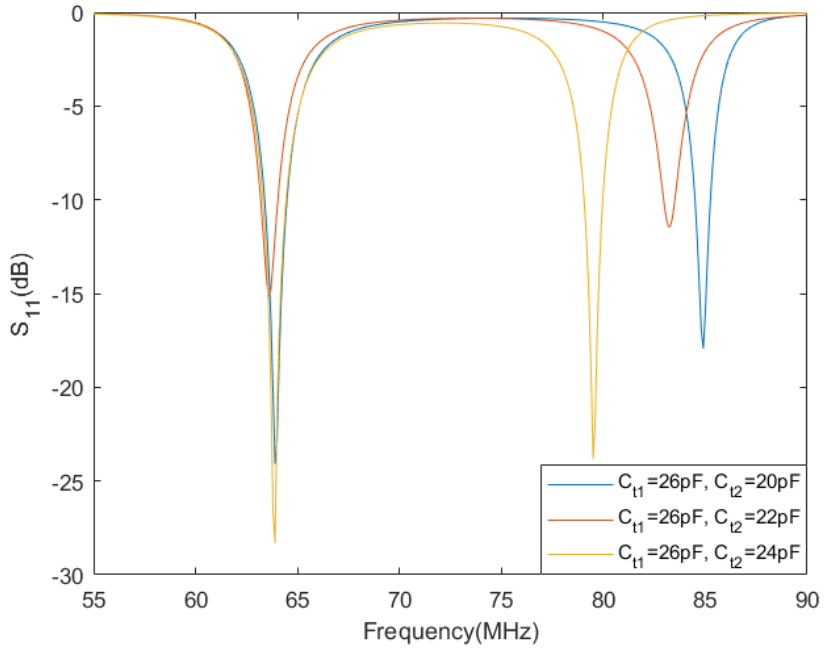

Fig. 4.11 Simulated S_{11} when C_{t2} was changed

From Fig. 4.11, when C_{t1} was kept constant, only the higher resonance frequency would be reduced when C_{t2} was increased. However, there was still a fixed gap between the two resonance frequencies, meaning that higher band could keep reducing by increasing the capacitance of C_{t2}. Thus, further adjustment in resonance frequency required the

small change in the dimension of the metasurface, which is investigated in subsection 4.4.2.

4.4.2 Effects of changing the dimension of the metasurface

During the simulation, we found that the extra resonance frequency provided by metasurface could be tuned independently by the tuning capacitor on the extra coil loop, but there was a limited frequency range when using tuning capacitor to control the extra resonance frequency. Thus, it is suggested to shift the extra resonance frequency to the frequency range the tuning capacitors can control by adjusting the dimension of the metasurface.

From subsection 4.3.2, it was found that *l* is the most effective parameter to tune the resonance frequency of the second resonance frequency. Fig. 4.12 presents the S_{11} results when *l* was varied from 80mm to 95mm, w_d and g_d were kept at 1.8mm and 0.8mm, respectively. The C_{t1} and C_{t2} were used to perform the small adjustment of resonance frequencies, and the impedance matching at 63.85MHz was accomplished by the C_m on the outer coil. It can be seen from Fig. 4.12 that, the low frequency resonance was increased with the digit length *l* decreasing, while the high frequency resonance was not significantly altered. All of cases got much better impedance match in two resonance frequencies due to high reflection coefficient S_{11}, compared with the cases of using single loop RF coil. When *l*=95mm, the lower resonance frequency was 62.8MHz, so *l* should be decreased a little again.

Fig. 4.13 shows the S_{11} results when *l* was adjusted from 96.5mm to 98.5mm. The matching capacitor C_m on the outer coil was adjusted from 190pF to 200pF to complete the impedance match in each case. When *l*=97.1mm, the two resonance frequencies at 60.08MHz and 63.85MHz could be achieved with good impedance match. The reason is the capacitance of metasurface was changed, so the resonant frequency of extra

resonance generated by metasurface was shifted.

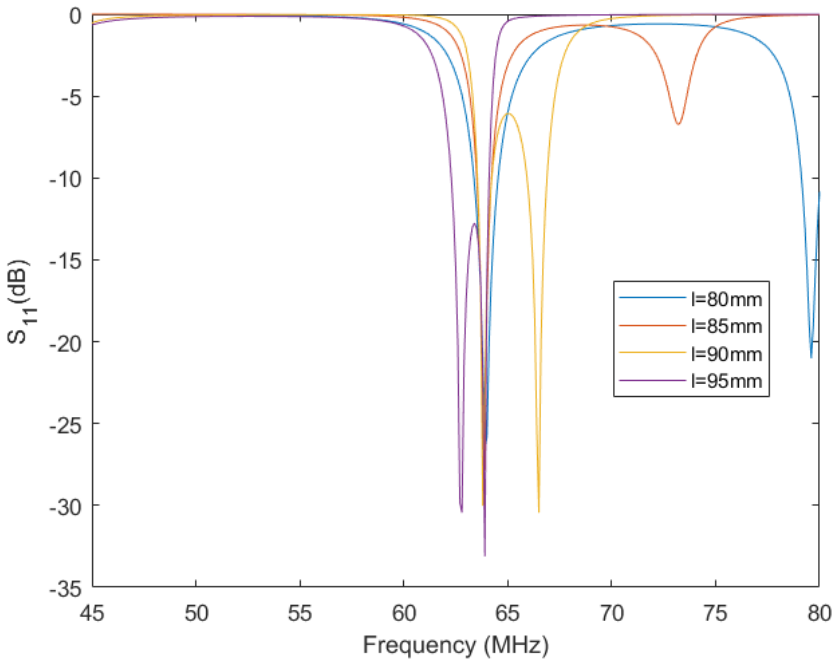

Fig. 4.12 Simulated S_{11} when l was changed

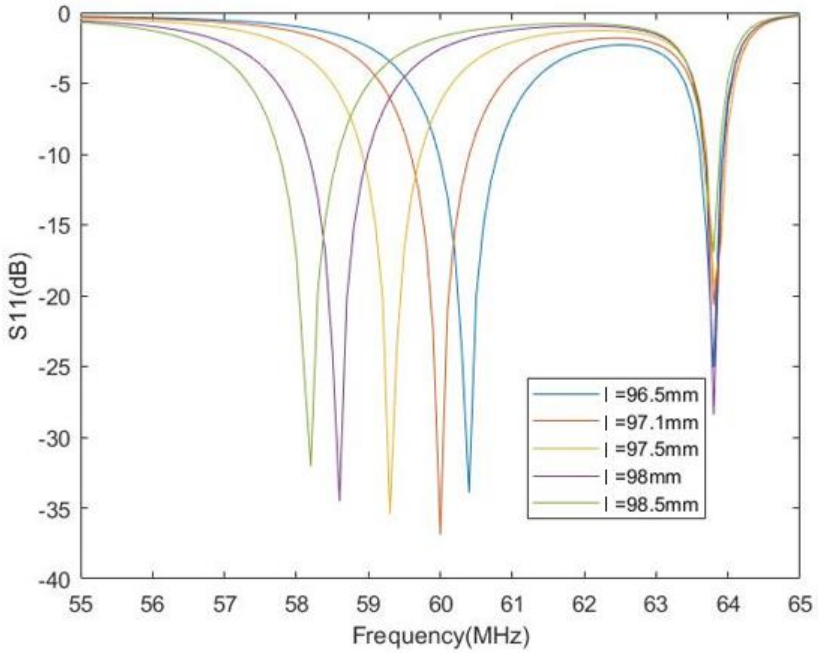

Fig. 4.13 Simulated S_{11} when l was adjusted in small range

As discussed in introduction part, the transmission performance of an MRI system is determined by B_1^+, which is proportional to the transmission coefficient S_{21} shown in Fig. 4.14. The peak value was correlated to the results of S_{11} shown in Fig. 4.11.

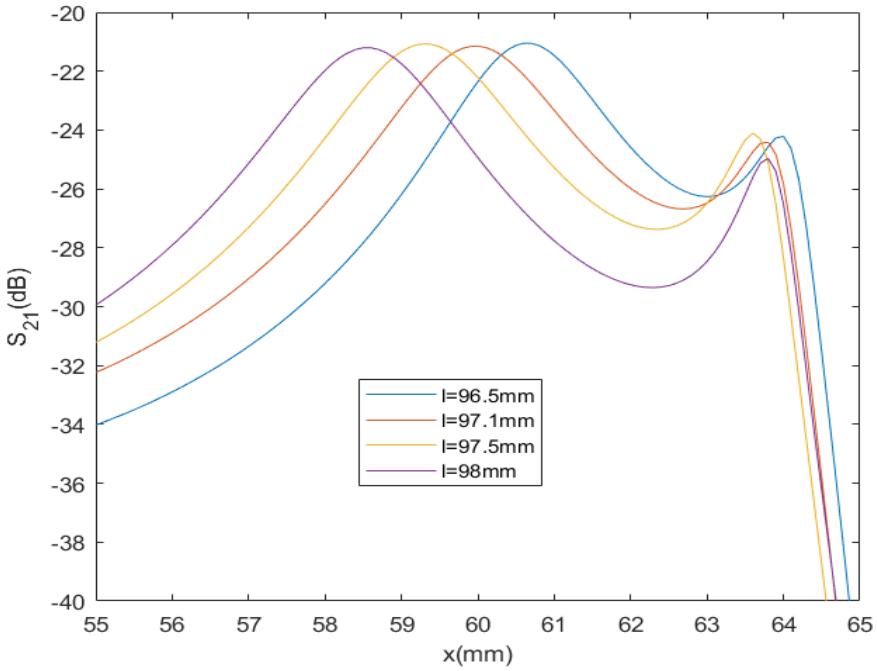

Fig. 4.14 Simulated S_{21} when l was adjusted in small range

Fig. 4.15 and Fig. 4.16 show the results of B_1^+ when *l* was adjusted from 96.5mm to 98mm at 60.08MHz and 63.85MHz, respectively. As discussed before, B_1^+ is proportional to S_{21}. The highest B_1^+ was achieved when *l*= 97.1mm, because only the metasurface with *l*=97.1mm had lower resonance at 60.08MHz, and the peak value of S_{21} was 60.08MHz. Fig.15 shows the value of B_1^+ at 63.85MHz when *l* was adjusted. The difference between each case was also related to the results of S_{21} shown in Fig. 4.14.

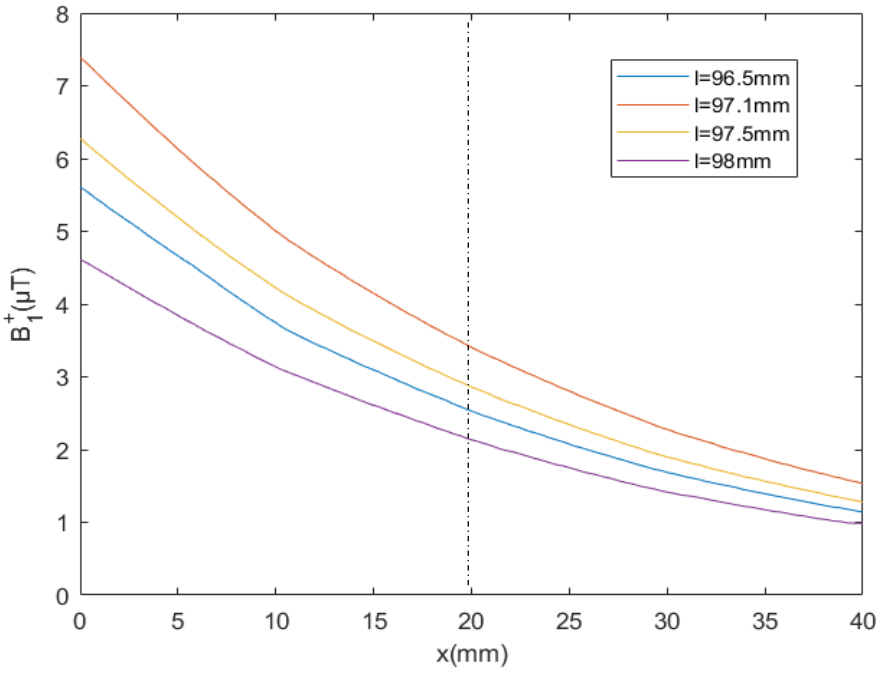

Fig. 4.15 Simulated B_1^+ at 60.08MHz when l was adjusted in small range

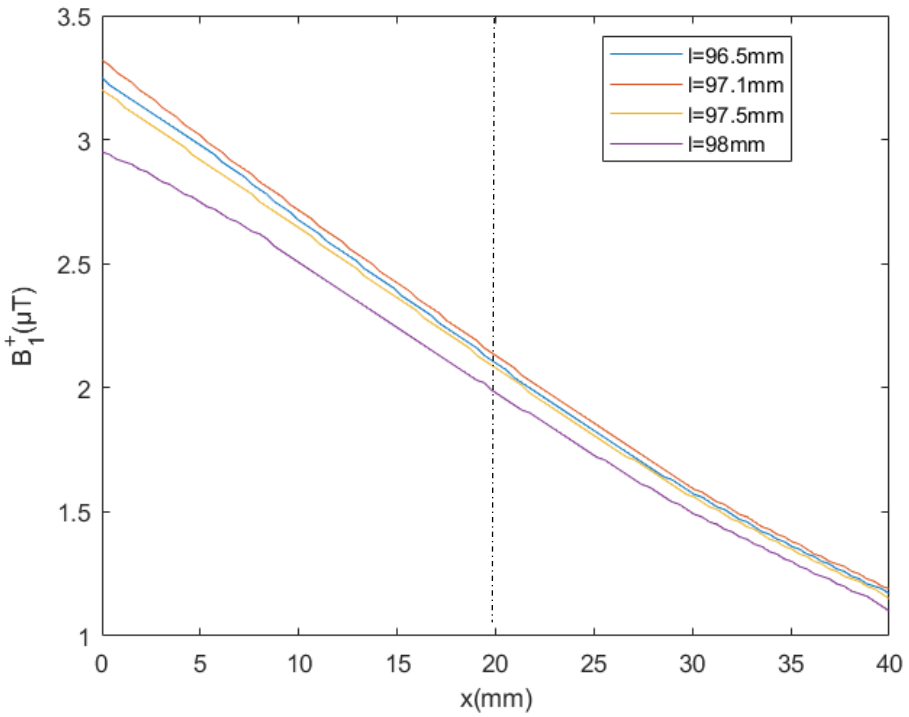

Fig. 4.16 Simulated B_1^+ at 63.85MHz when l was adjusted in small range

4.4.3 Effects of adjusting the distance between each component

In this case, we examined the effects of the distance between each component on the dual band property. The difference between this subsection and section 4.3 was that the single loop RF coil was replaced by the dual loop RF coil, and the dimension of the metasurface was adjusted. Therefore, the two resonance frequencies at 60.08MHz and 63.85MHz can be always achieved, and the relationship between the distance and transmission performance can be obtained. Fig.4.17, Fig. 4.18 and Fig. 4.19 present the S_{11} results when D, S and H were changed, respectively. It was found that the impedance match can not get improvement compared with the results shown in last subsection, and the two resonance frequencies could be tuned to 60.08MHz and 63.85MHz, respectively, in all cases.

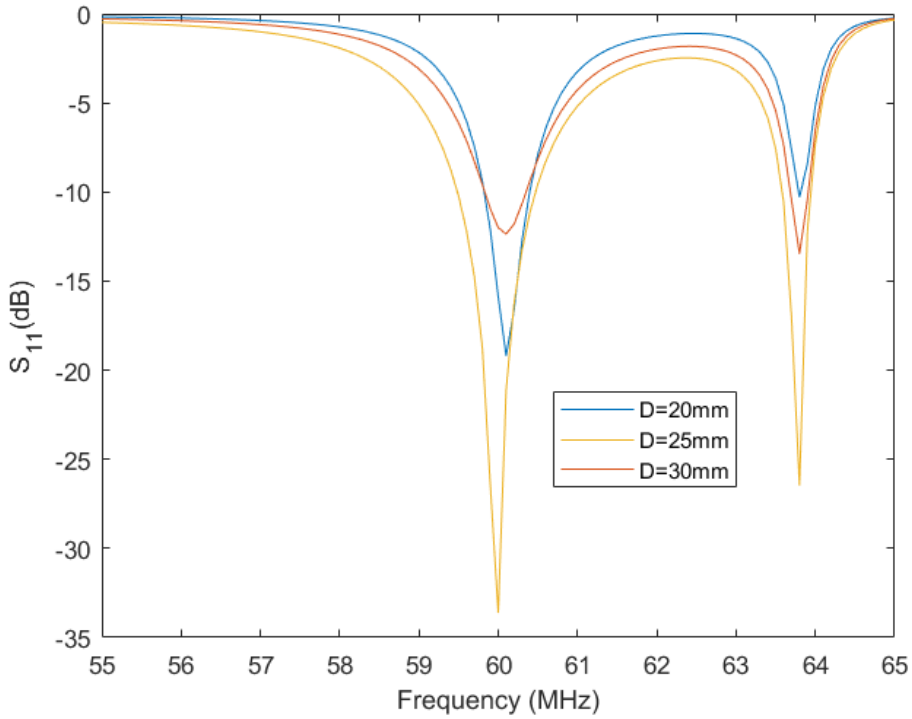

Fig. 4.17 Simulated S_{11} when D was changed

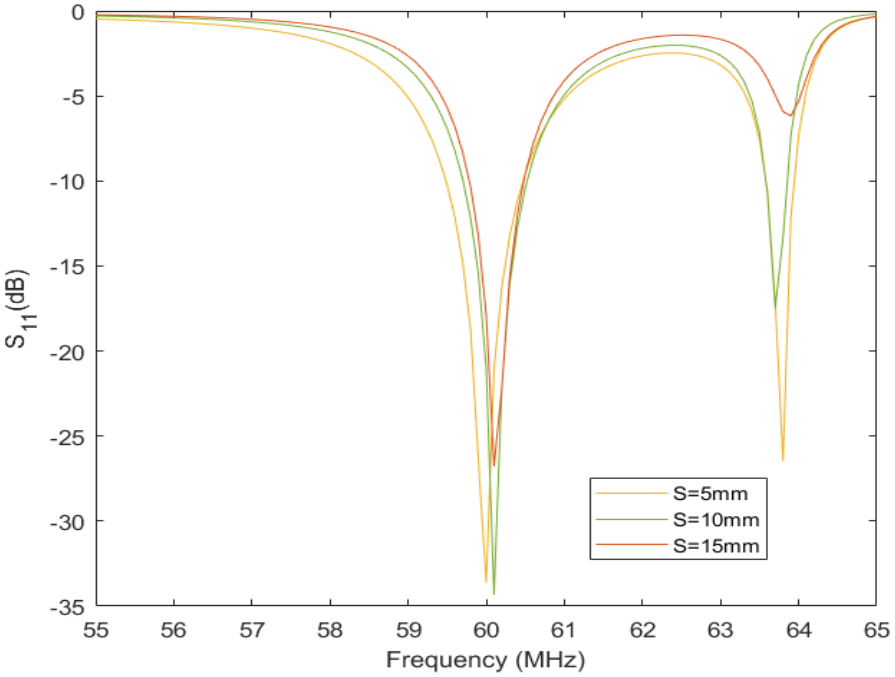

Fig. 4.18 Simulated S_{11} when S was changed

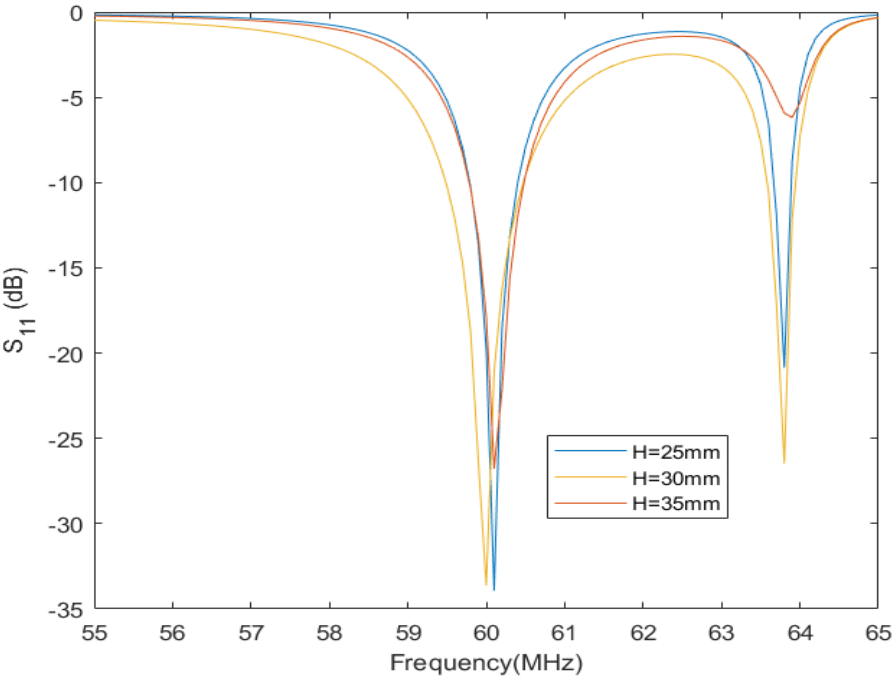

Fig. 4.19 Simulated S_{11} when H was changed

As discussed in the previous subsection, the transmission performance of an MRI system is determined by B_1^+. Then, the most appropriate distance between each component can be obtained by comparing the B_1^+ results. Fig. 4.20, Fig. 4.21 and Fig. 4.22 present the B_1^+ results at 60.08MHz when D, S and H were adjusted, respectively. Fig. 4.23, Fig. 4.24 and Fig. 4.25 display the B_1^+ results at 63.85MHz when D, S and H were adjusted, respectively. The dash line of x=20mm indicates the interface between the ^{1}H phantom and the ^{19}F phantom.

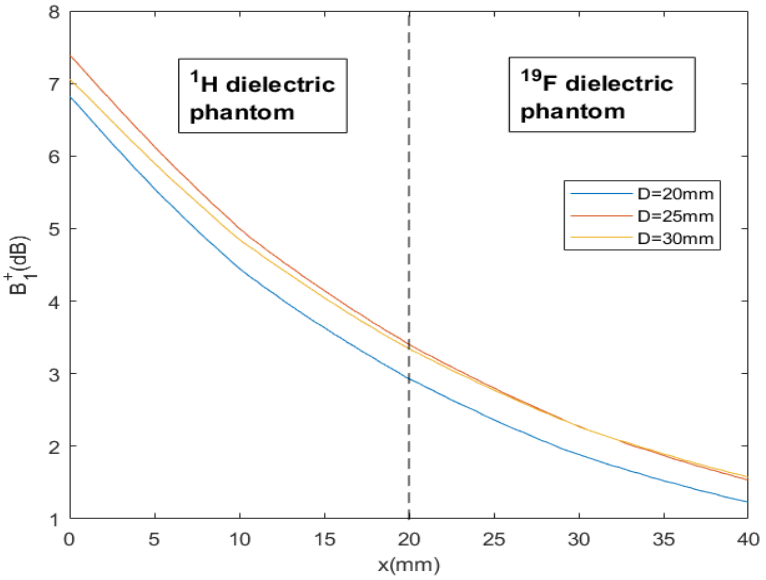

Fig. 4.20 Simulated B_1^+ at 60.08MHz when D was adjusted

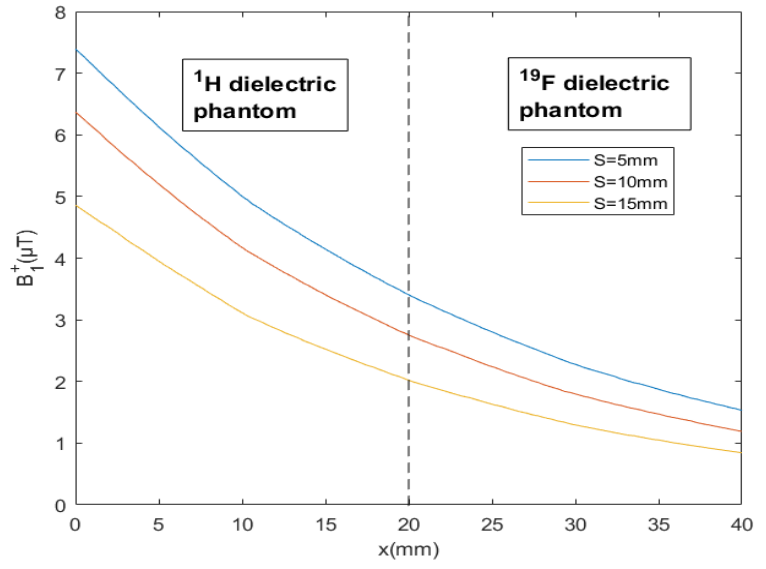

Fig. 4.21 Simulated B_1^+ at 60.08MHz when S was adjusted

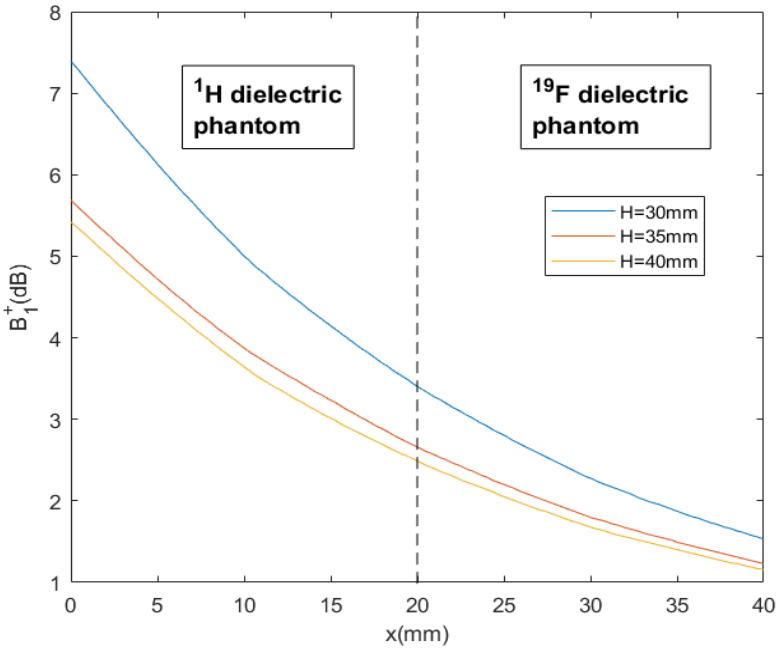

Fig. 4.22 Simulated B_1^+ at 60.08MHz when H was adjusted

From Fig. 4.20 and Fig. 4.21, it can be found that B_1^+ depended on the distance between the metasurface and the dielectric phantom instead of the spacing between the RF coil and the dielectric phantom. The magnitude of B_1^+ on the phantom surface was decayed with the metasurface getting far away from the phantom, and did not have obvious relationship with the distance between the RF coil and dielectric phantom. Fig. 4.22 illustrates that when H was increased, B_1^+ would be decreased, because the metasurface was away from the dielectric phantom.

The B_1^+ results at 63.85 MHz show the similar trend as those at 60.08MHz. The magnitude of B_1^+ was inversely proportional to the distance between the metasurface and the dielectric phantom.

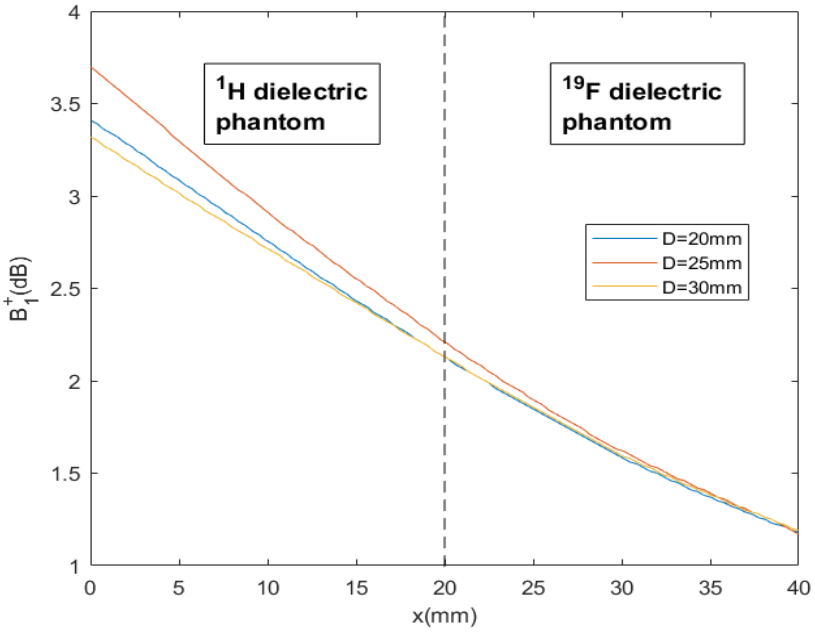

Fig. 4.23 Simulated B_1^+ at 63.85MHz when D was adjusted

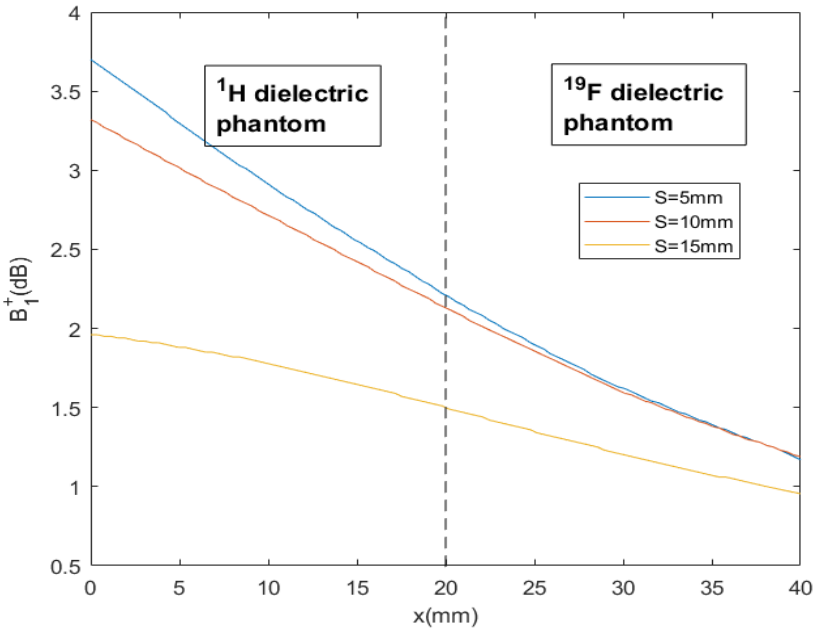

Fig. 4.24 Simulated B_1^+ at 63.85MHz when S was adjusted

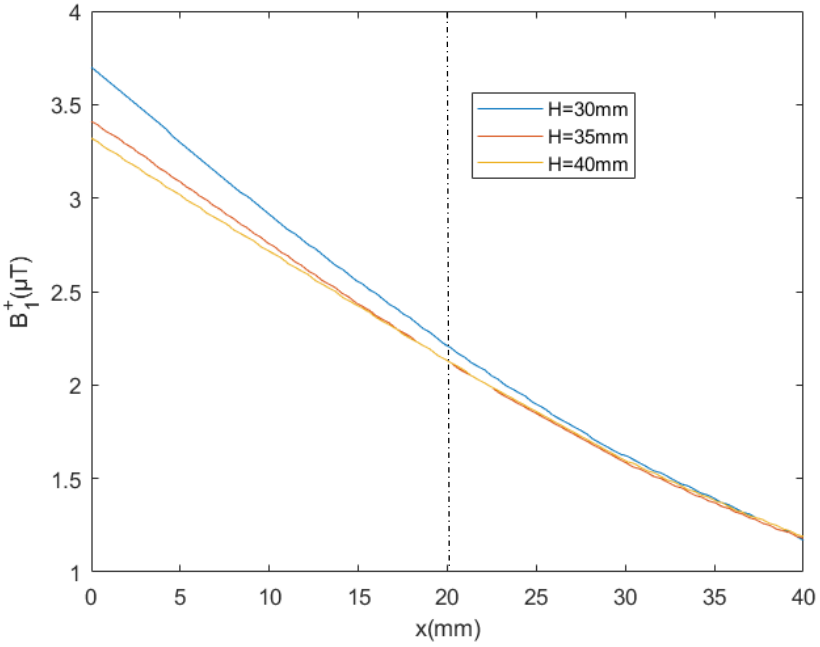

Fig. 4.25 Simulated B_1^+ at 63.85MHz when H was adjusted

4.5 Effects of replacing the resonance frequencies controlled by the tuning capacitors

As discussed in the previous subsection, the lumped element C_{t1} on the outer coil was used to control both resonance frequencies, and C_{t2} on the inner coil was used to control the higher resonance frequency. During the simulation, it was found that the function of C_{t1} and C_{t2} could be altered, when the dimension of the metasurface was changed to l=98mm, w_d=1.8mm and g_d=1mm. Fig. 4.26 shows the S_{11} results of two metasurface designs. Both two metasurface designs could achieve two resonance frequencies at 60.08MHz and 63.85MHz. Furthermore, the frequency band controlled by the C_{t2} always had narrower band and poorer S_{11} than the other frequency band.

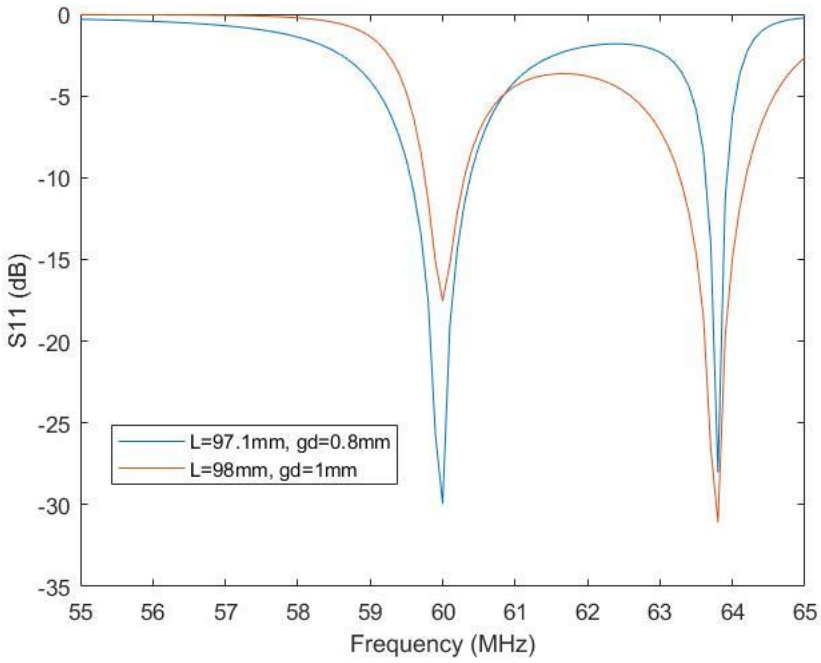

Fig. 4.26 Simulated S_{11} of two metasurface designs

Then, the transmission performance of these two metasurfaces were investigated by comparing with the coil only case. In this case, when the metasurface was absent, the distance between the RF coil and the phantom was kept as 5mm to maximize the performance of the RF coil. Fig. 4.27 shows the result of transmission coefficient (S_{21}) when the receiving probe was placed 20mm inside the ^{1}H phantom, and was on the interface between the ^{19}F phantom and ^{1}H phantom. Thus, the transmission performance at 63.85MHz for ^{1}H phantom was measured. The results were compared to the case of a single tuned coil or dual loop coil without metasurface tuned to 60.08MHz firstly. Both cases with metasurface had a resonance frequency at 63.85MHz, so S_{21} got significant improvement at 63.85MHz compared with the case of coil only tuned at 60.08MHz. Fig. 4.28 shows the S_{21} results when the resonance frequency of coil only cases were tuned to 63.85MHz, so the performance with the metasurface can be compared with the standard performance. When the metasurface with l=98mm was present, 1dB increment was obtained compared with coil only cases. Fig. 4.29 shows the S_{21} result when the receiving loop was placed on the back surface of the ^{19}F phantom. S_{21} was measured when the resonance frequency of the single or dual loop coil without

metasurface were tuned at 60.08MHz. According to the results of S_{21}, both metasurface designs provided extra band with acceptable performance compared with coil only cases, but both were lower than coil only cases after 40mm penetration depth.

There was a significant difference between the performances of two selected CIS designs. When using the metasurface of l=97.1mm, w_d=1.8mm and g_d=0.8mm, S_{21} was increased by about 2dB at 60.08MHz, and decreased by 1dB at 63.85MHz compared with coil only cases. When using the metasurface of l=98mm, w_d=1.8mm and g_d=1mm, S_{21} was decreased by 2dB at 60.08MHz, and increased by 2dB at 63.85MHz. A balance can be achieved depending on the type of MRI acquisition.

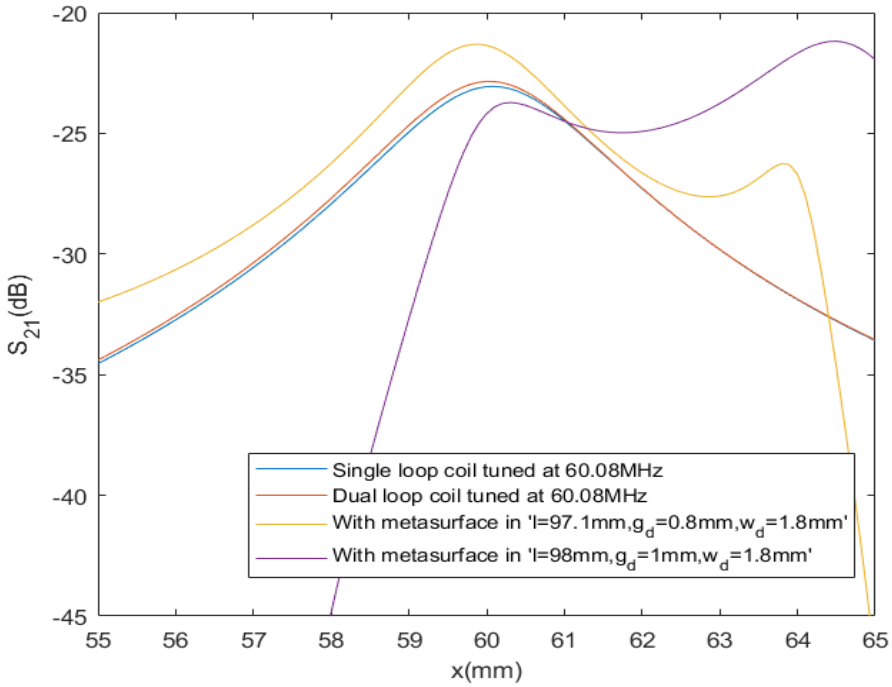

Fig. 4.27 Simulated S_{21} when single band loops were optimized for 60.08 MHz

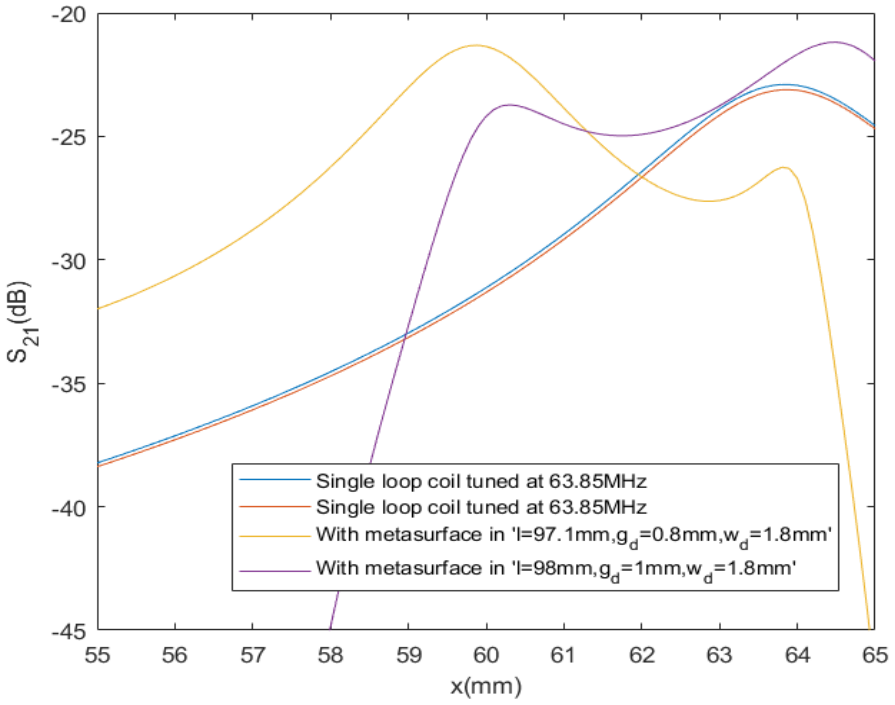

Fig. 4.28 Simulated S_{21} when single band loops were optimized for 63.85 MHz

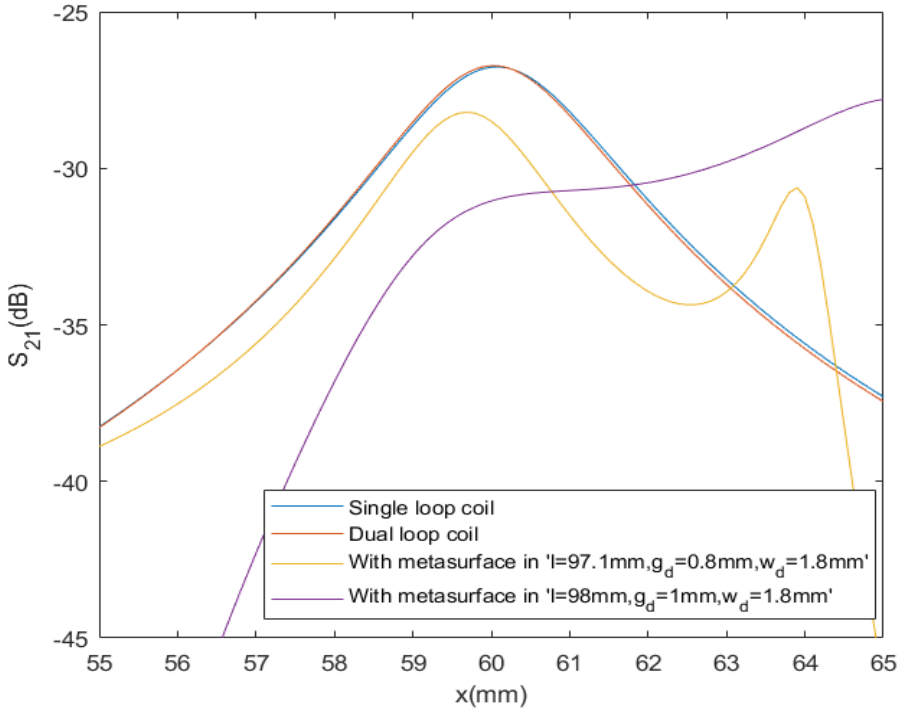

Fig. 4.29 Simulated S_{21} when single band loops were optimized for 60.08 MHz

4.6 Magnetic flux density B_1

In order to investigate the effects of the metasurface on the MRI RF transceiver system, B_1^+ and normalised B_1^- that characterize the transmission performance and receiver sensitivity, respectively, are discussed in this subsection. Fig. 4.30 indicates the 2D field of B_1^+, when the resonance frequency of each coil without metasurface was tuned at 60.08MHz. We can get some key information from the figure. Firstly, the dual loop RF coil with single fed showed worse field than single loop RF coil when the metasurface was absent, due to the energy losses in its complex structure and the coupling between extra lumped elements. From Fig. 4.31, both single and dual loop RF coils showed bad transmission performance at 63.85MHz because of the poor impedance match.

When two metasurface designs were placed between the RF coil and the dielectric phantom, good performance was achieved at the both frequencies of 60.08MHz and 63.85MHz. Furthermore, the results of B_1^+ of two designs indicate that each metasurface can improve the fields at one frequency band more than the other frequency band. The metasurface design of l=97.1mm, w_d=1.8mm and g_d=0.8mm could improve the B_1^+ field at 60.08MHz, which was better than the B_1^+ field at 63.85MHz. The second metasurface design of l=98mm, w_d=1.8mm and g_d=1mm could improve the B_1^+ field at 63.85MHz more, which was better than the B_1^+ field at 60.08MHz. Therefore, the field at the frequency band tuned by the C_{t1} could get more enhancement. Both metasurfaces had no destructive effects on the field using a periodic structure.

The results of normalised B_1^- are shown in Fig. 4.32 and Fig. 4.33. In this case, the x-axis is defined as from the hydrogen phantom surface to the back surface of the fluorine phantom. The dash line of x=20mm represents the interface between the fluorine phantom and the hydrogen phantom.

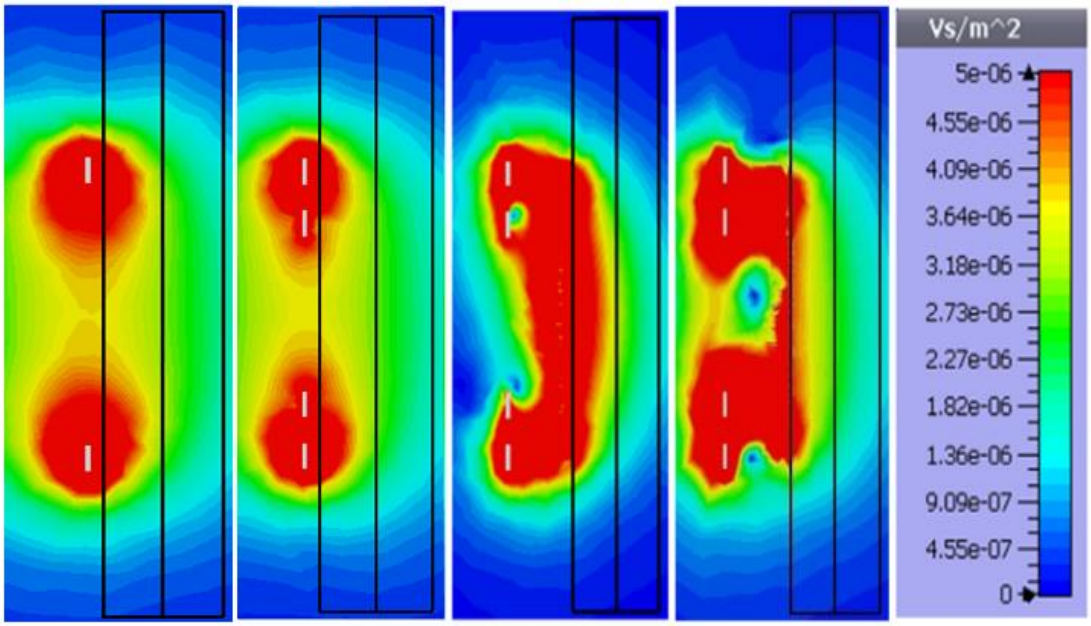

(a) (b) (c) (d)

Fig. 4.30 Simulated B_1^+ results in the *x-y* plane at 60.08MHz for two layer phantom. (a). Single loop coil. (b) Dual loop coil. (c) With metasurface of L=97.1mm, g_d=0.8mm, w_d=1.8mm (d) with metasurface of L=98mm, g_d =1mm, w_d=1.8mm)

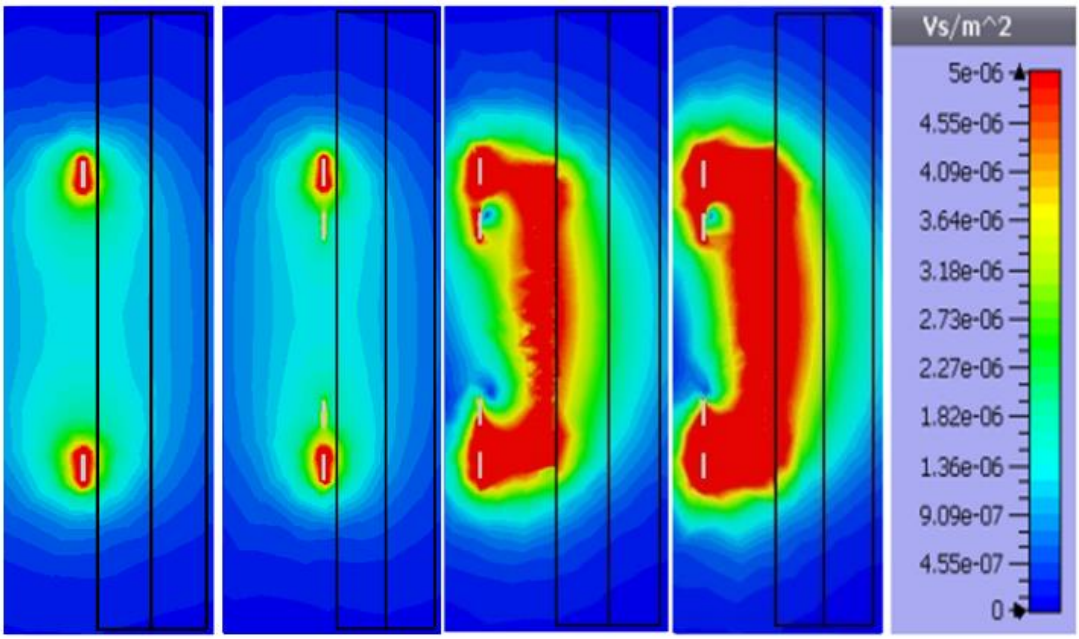

(a) (b) (c) (d)

Fig. 4.31 Simulated B_1^+ results in the *x-y* plane at 63.85 MHz for two layer phantom. (a). Single loop coil. (b) Dual loop coil. (c) With metasurface of *l* =97.1mm, g_d =0.8mm, and w_d =1.8mm) (d) with metasurface of *l* =98 mm, g_d=1 mm, w_d=1.8 mm

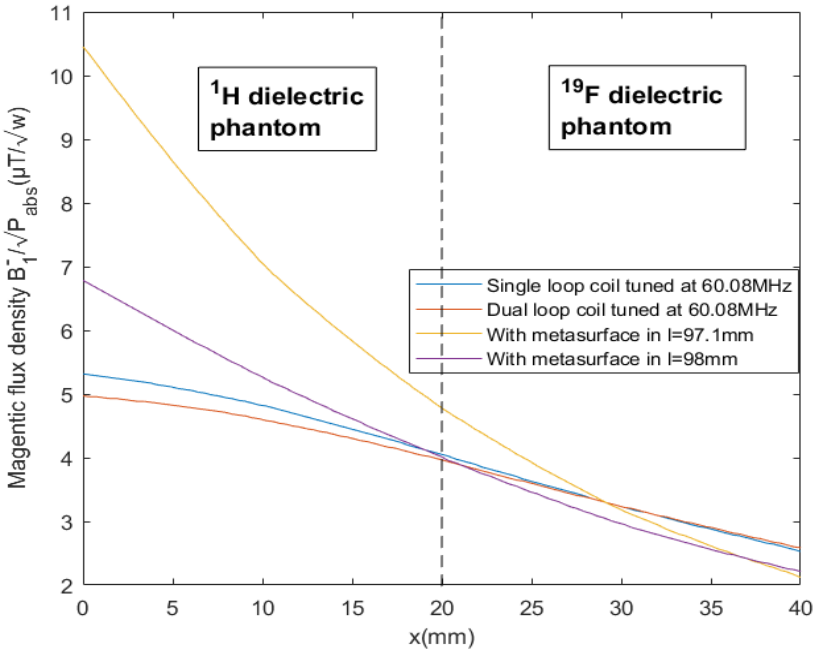

Fig. 4.32 The normalized B_1^- result inside the dielectric phantom along the x-axis at

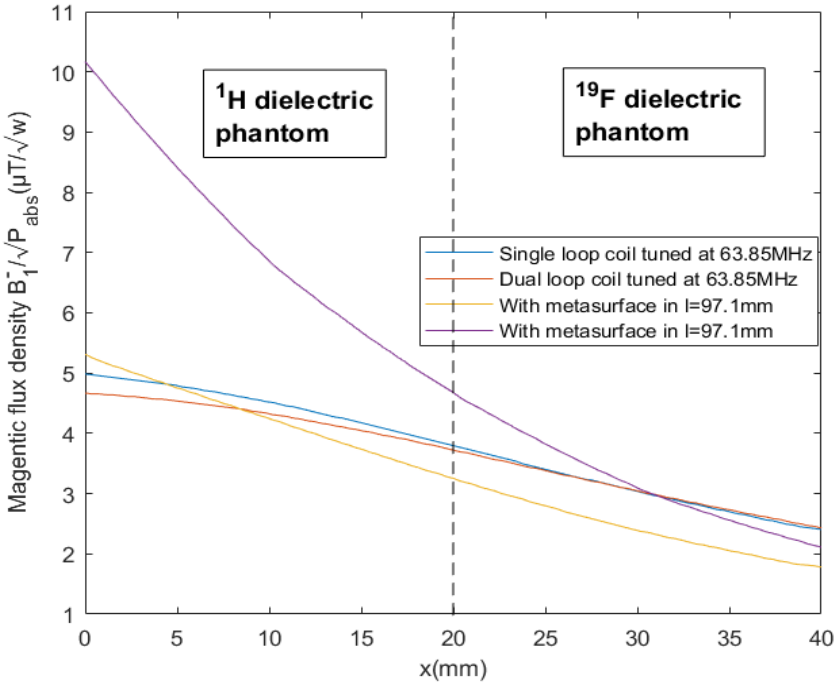

Fig. 4.33 The normalized B1$^-$ inside the dielectric phantom along the x-axis at 63.85MHz when the single RF coil cases was tuned at 63.85MHz

Fig. 4.32 shows the normalised B_1^- at 60.08MHz. When the metasurface of l=97.1mm, w_d=1.8mm and g_d=0.8mm was present, an improvement of about 24% was achieved at the surface of the ^{19}F phantom compared with single loop RF coil. This improvement covered a penetration depth of 8mm (from 20mm to 28mm). When the metasurface of *l*=98mm, w_d=1.8mm and g_d=1mm was present, the normalized B_1^- was similar to the RF coil tuned at 60.08MHz.

Fig. 4.33 show the normalized B_1^- at 63.85MHz. In this case, the normalized B_1^- results of single loop coil and dual loop coil were measured when their resonance frequencies were tuned to the focused frequency bands, respectively. When the resonance frequency of coil only cases was tuned to 60.08MHz, the normalized B_1^- results at 63.85MHz were closed to 1μT, due to the poor impedance matching, and the cases with metasurface showed acceptable results in the hydrogen phantom (from 0mm to 20mm), compared with the results of coil only cases shown in Fig. 4.32. From Fig. 4.33, when the metasurface of *l*=98mm, w_d=1.8mm and g_d=1mm was placed between the RF coil and the phantom, the normalized B_1^- was increased by 102% at the ^1H phantom surface, and this enhancement covered the whole width of the ^1H phantom.

From the normalized B_1^- results when the metasurface of l=97.1mm, w_d=1.8mm and g_d=0.8mm was placed between the RF coil and the phantom, the normalized B_1^- at 60.08 MHz increased by 24% on the ^{19}F phantom surface, and has similar normalized B_1^- as well-tuned single RF coil at 63.85MHz. When the metasurface of l=98mm, w_d=1.8mm and g_d=1mm was present, the normalized B_1^- at 63.85MHz increased by 102% at ^1H phantom surface. In other words, this shows that the fields at the resonance frequency controlled by the outer coil could get larger improvement, but the fields at the other frequencies still had similar performance as the single coil with perfect tuning.

4.7 Summary

In this chapter, the dual band property of the metasurface with non-periodic structure has been investigated. Firstly, the dual band property of the metasurface was proved to be derived from the coupling between the RF coil and the metasurface. The second resonance frequency was only tuned when the spacing between the RF coil and the metasurface was adjusted. Then, the relationship between the dimension of the metasurface and the second resonance frequency was investigated, and the length of the strip lines on metasurface, *l*, was found to be the most effective parameter to shift the extra resonance frequency. The problem of changing the dimension of the metasurface to tune the second resonance frequency was also obvious. The tuning capacitor on the RF coil tuned the both resonance frequencies. Consequently, the tuning was very hard during the measurement when some factors were influencing the resonance frequency of the RF coil, such as the dielectric phantom and the soldering. Then, the matching capacitor could only adjust one resonance frequency to impedance match, so the transmission performance of the resonance without matching was very poor.

In order to tune the second resonance frequency more accurately and confirm the performance, the dual loop RF coil with single fed was proposed to improve the multi-band tuning work. Firstly, no extra resonance frequencies could be provided by the dual loop RF coil until the metasurface was placed between the RF coil and the dielectric phantom. Then, the overall performance of the dual loop RF coil was worse than the single loop coil as more energy was lost due to its complex structure and extra lumped elements. Therefore, the improvement from the metasurface would be compared with single loop RF coil when the metasurface was in absent. After adjusting the parameters, the final design of the metasurface used to achieve dual band imaging was l=97.1mm, w_d=1.8mm and g_d=0.8mm and l=98mm, w_d=1.8mm and g_d=1mm. The former design using C_{t2} controlled the higher band independently, and the latter design using C_{t2} controlled the lower band independently. The performance of these designs was determined by S_{21}, B_1^+ and normalized B_1^-. All the results showed that, the resonance freqnency controlled by the tuning capacitor on the outer RF coil C_{t1} could always have

better performance than the resonance frequency controlled by C_{t2}. As a result, we could know that the resonance frequency provided by the RF coil had better transmission performance than the that by the coupling between the metasurface and the RF coil. From the results of B_1^+ field, both of the metasurfaces showed homogeneous fields at 60.08MHz and 63.85MHz. The B_1^- normalized results indicated that the two metasurfaces had acceptable normalized B_1^- at both focused frequencies compared with well-tuned single coil. When the metasurface of l=97.1mm, w_d=1.8mm and g_d=0.8mm was present, the normalized B_1^- was increased by 6% at ^{1}H phantom surface at 63.85MHz, and 24% at the ^{19}F phantom surface at 60.08MHz. When the metasurface of l=98mm, w_d=1.8mm and g_d=1mm was present, the normalized B_1^- was increased by 102% at the ^{1}H phantom surface, and similar performance with single tuned coil at the ^{19}F phantom surface at 60.08MHz.

Chapter 5

Measurements of the metasurface in dual band imaging

5.1 Introduction

In the last chapter, we have proposed two metasurface designs which could achieve dual band imaging at 60.08MHz and 63.85MHz for fluorine imaging and hydrogen imaging, respectively. One metasurface is with l=97.1mm, g_d =0.8mm, w_d =1.8mm, which has the similar performance as the single loop RF coil tuned at 63.85MHz and increased normalized B_1^- at the ^{19}F phantom surface by 24% at 60.08MHz. The other metasurface design is with l=98mm, w_d=1.8mm and g_d=1mm, which has the similar normalised B_1^- as the well-tuned single loop coil without the metasurface at 60.08 MHz, and the normalised B_1^- is increased by 102% at the ^1H phantom surface.

In this chapter, the metasurface design of *l*=97.1mm, g_d =0.8mm, w_d =1.8mm is further investigated. The reason is that the fluorine nuclei imaging is always used in lungs

imaging, which is 2-3cm away from the skin, thus requiring more enhancement than hydrogen nuclei, due to extra power losses in the part between skin and lungs. In the last chapter, the metasurface of l=97.1mm, g_d =0.8mm, w_d =1.8mm shows more enhancement in B_1^- at 60.08 MHz, compared with the other metasurface design.

In section 5.2, the 2D field of B_1^+ and E-field are analyzed to characterize the enhancement provided by the metasurface in the simulation. Section 5.3 presents the experiment in a lab environment. Two dielectric phantom models are tested. One is dual layer phantom, which consists of a 30cm×20cm×2cm hydrogen phantom full of $CuSO_4$ solution, and a glass bottle full of fluorine to model a fluorine phantom. This phantom type is used to prove the model simulated in CST. The other phantom model is based on human body, where the fluorine phantom is considered as the real lungs surrounded by hydrogen nuclei. The fluorine phantom which is a plastic bag full of fluorine gas is placed inside of the hydrogen phantom full of $CuSO_4$ solution. The S-parameter, SNR and flip angle are analyzed in each case to compare the metasurface design in two models with two single loop RF coils tuned to 60.08MHz and 63.85MHz, respectively. Section 5.4 provides the conclusion of this chapter and compares the measurement results with previous research results to highlight the novelty and the improvement of the proposed non-periodic metasurface.

5.2 MRI Concept and Metasurface Design

In chapter 4, the performance of the metasurface was analyzed by the comparison with the single loop RF coils tuned to 60.08MHz and 63.85MHz, and the single loop RF coils were placed 5mm away from the dielectric phantom. When measuring the RF transceiver model within the MRI scanner, it was suggested to place the single loop RF coil on the dielectric phantom to maximise the performance of the case without the metasurface, although the RF surface coil should keep a certain distance from the human body to ensure the safety. In this case, when the metasurface was absent, the

single loop coil was placed on the dielectric phantom surface. When the metasurface was present, the dual loop coil was placed 25mm away from the metasurface, and the metasurface was placed 5mm away from the dielectric phantom surface.

5.2.1 Magnetic flux density B_1^+

The performance of the RF transceiver system with the metasurface of *l*=97.1mm, gd=0.8mm, w=1.8mm has been evaluated by numerical simulation in chapter 4. In this case, the optimization in the field from the metasurface is analyzed by comparing the results of B_1^+ field in linear with a measured line along the phantom centre or in 2D.

The 2D B_1^+ fields in the *x*-*y* plane are shown in Fig. 1 and Fig. 2, with the frequency being 60.08MHz and 63.85MHz, respectively. The positions of the hydrogen phantom and fluorine phantom were determined by the left rectangular and the right rectangular in Fig. 5.1 and Fig. 5.2. As shown in Fig. 5.1, the metasurface showed good performance in enhancing the B_1^+ fields with uniform distribution, although the field strength was reduced in a faster manner than other cases towards the edge of the ^{19}F phantom. Fig. 5.2 shows the B_1^+ results at 63.85MHz. The dual loop coil with the metasurface had the similar performance inside the hydrogen phantom as the single loop RF coil with perfect tuning, but the field strength decayed faster inside the fluorine than the coil only case.

In order to compare the B_1^+ results in a more objective way, a measure line through the phantom centre was set, as represented by a red dash in Fig. 5.1. The measure line was used to calculate the B_1^+ field strength along the *x*-axis. The decay trend of field strength can also be reflected by the linear results of B_1^+ which measured the B_1^+ field strength along the central line. Fig. 5.3 shows the $|B_1^+|$ results at 60.08MHz through the centre of both ^1H dielectric phantom and ^{19}F dielectric phantom. The starting point *x*=0mm means the top surface of the ^1H phantom, the ending point *x*=40mm means the back surface of the ^{19}F phantom, and the interface of the ^1H phantom and ^{19}F phantom is at

x=20 mm represented by a dash line. The B_1^+ results from *x*=20mm to *x*=40mm showed the decay of B_1^+ in the ^{19}F phantom. When the metasurface of l=97.1mm, gd=0.8mm, w=1.8mm was present, was an improvement of about 24% was achieved at the surface of the ^{19}F phantom compared with single tuned coil. However, the performance was inferior to the single loop coil in ^{19}F phantom, due to the higher decay ratio.

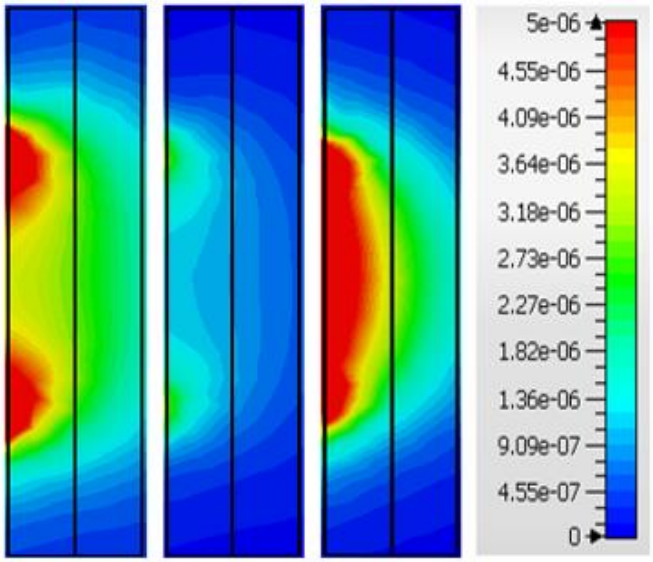

(a) (b) (c)

Fig. 5.1 B_1^+ results through *x*-*y* plane at 60.08MHz(z=0), (a) single loop coil tuned at 60.08MHz, (b) single loop coil tuned at 63.85MHz, (c) dual loop coil with metasurface

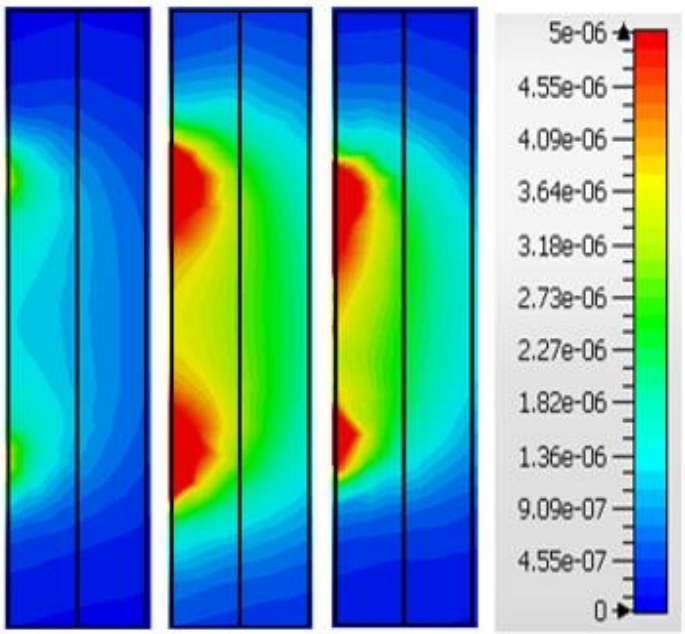

(a) (b) (c)

Fig. 5.2 B_1^+ results through *x*-*y* plane at 63.85MHz(z=0), (a) single loop coil tuned at 60.08MHz, (b) single loop coil tuned at 63.85MHz, (c) dual loop coil with metasurface

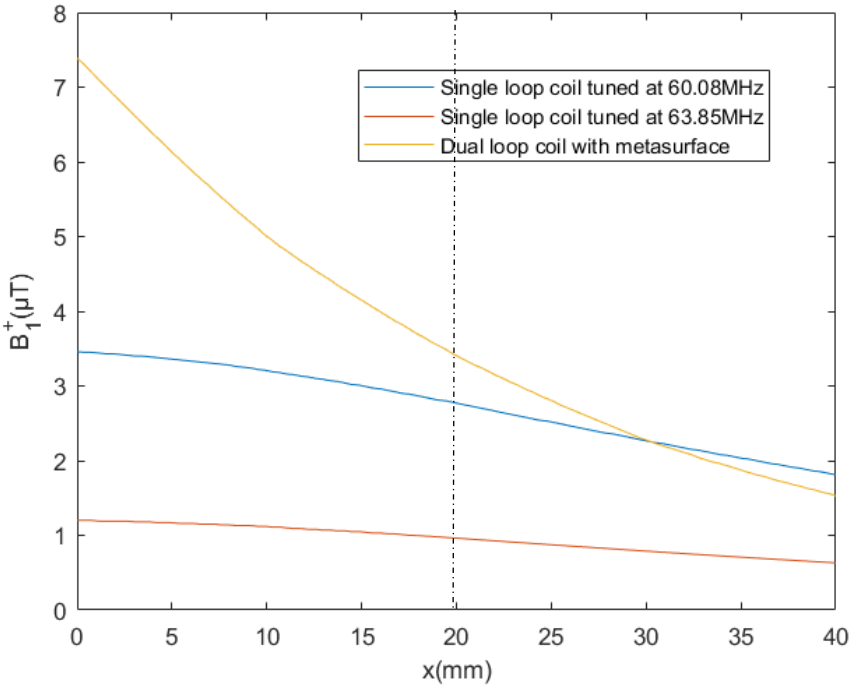

Fig. 5.3 Simulated B_1^+ results along x-axis at 60.08MHz (y=z=0)

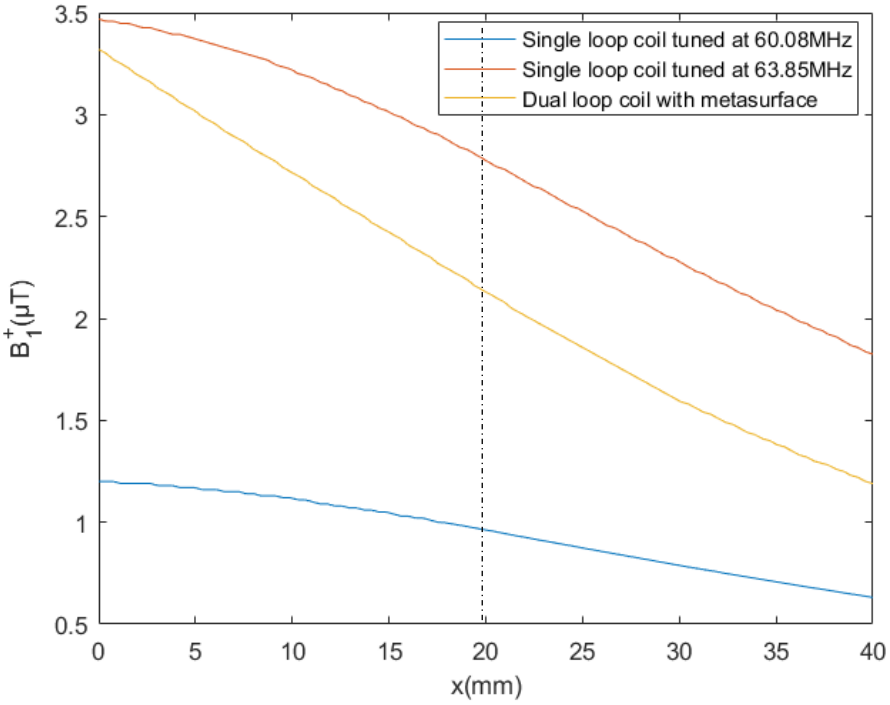

Fig. 5.4 Simulated B_1^+ results along x-axis at 63.85MHz (y=z=0)

Fig. 5.4 presents the results of B_1^+ at 63.85MHz for ^{1}H MRI. The decay procedure in the ^{1}H phantom can be observed from x=0mm to x=20mm. The metasurface did not show some improvement in this case, but it showed acceptable transmission performance compared with the single loop coil tuned at 60.08MHz due to its dual band property. The B_1^+ field strength was decreased by 20% at the back surface of the hydrogen phantom (x=20mm). The performance was reduced by 4.1% compared to the single coil placed on the phantom surface.

5.2.2 Electric field

Fig. 5.5 and Fig. 5.6 show the E-field in 2D inside the dielectric phantom in x-y plane at z=0, when the resonance frequency was at 60.08MHz and 63.85MHz, respectively. Each figure has a red dash line at the magnitude of the E-field at the maximum value regions (R1, R2 and R3 for Fig. 5 (a), (b) and (c) respectively) which represent the magnitude of the E-field when the resonance frequency was tuned to 60.08MHz.

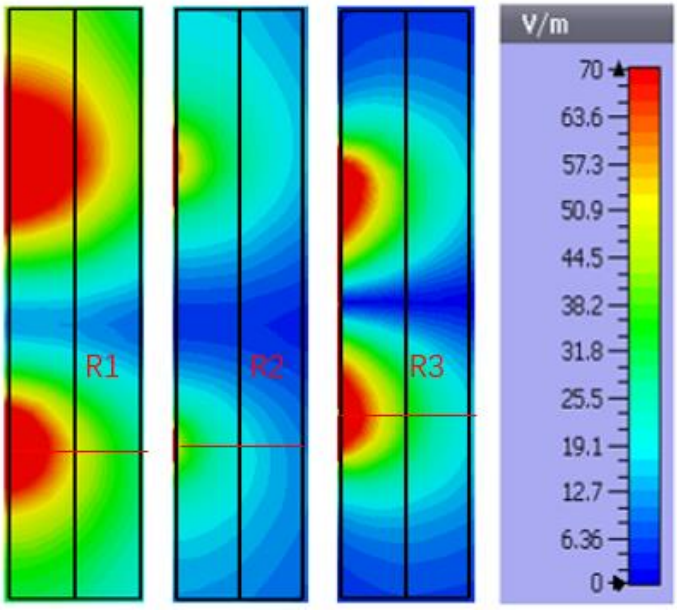

(a) (b) (c)

Fig. 5.5 E-field through x-y plane at 60.08MHz(z=0), (a) single loop coil tuned at 60.08MHz, (b) tuned at 63.85MHz, (c) dual loop coil with metasurface

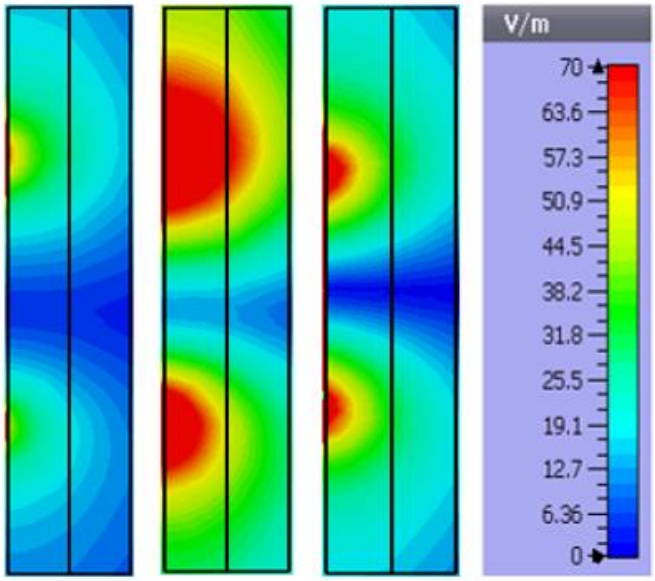

(a) (b) (c)

Fig. 5.6 E-field through x-y plane at 60.08MHz(z=0), (a) single loop coil tuned at 60.08MHz, (b) tuned at 63.85MHz, (c) dual loop coil with metasurface

In Fig.5.5, R1=46mm, R2=42mm and R3=33mm, and the penetration depth of the E-field had obvious decay with the distance increasing when the metasurface was present. Therefore, the total SAR in the dielectric phantom would decrease, due to the decrease in the overall E-field. The reason is that although B_1^+ could be improved by placing the RF coil near the phantom surface, the E-field would also be increased. Fig. 5.6 shows the E-field at 63.85MHz, where the single loop RF coil tuned at 63.85MHz also had a stronger E-field compared with the dual loop coil with the metasurface.

5.3 Metasurface manufacturing

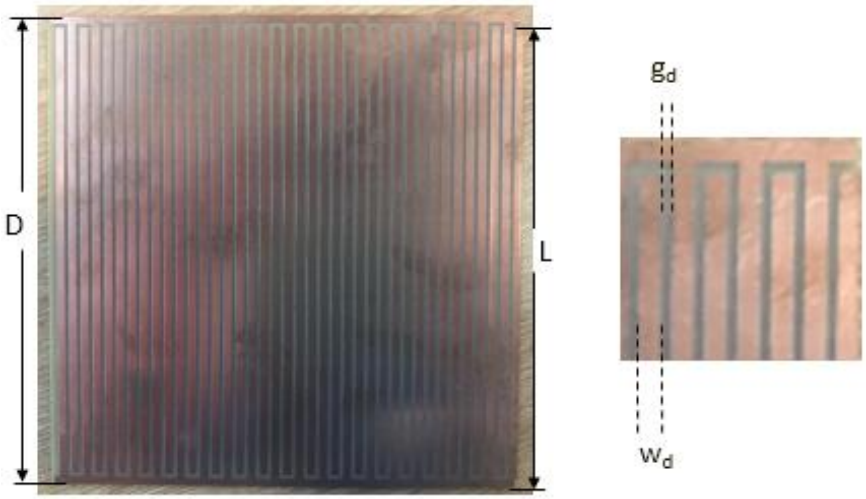

Fig. 5.7 Manufactured metasurface

The metasurface design with l=97.1mm, g_d =0.8mm, w_d =1.8mm was manufactured and tested in a 1.5T MRI scanner. The metasurface was manufactured using a PCB etching technique, by printing the copper on both sides of FR-4 borad. The top layer is shown in Fig. 5.7, and the bottom layer is an orthogonal copy of the top layer to produce dual polarization.

5.4 Experimental verification with a dielectric phantom

5.4.1 Dual layer phantom

Two different phantom structures were tested in this case. The first structure was the 'dual layer phantom', which was similar ^{1}H phantom to the model in simulation and consisted of two separate phantoms. The top layer was hydrogen phantom mimicked by a 30cm×20cm×2cm A4 plastic box, which was filled with $CuSO_4$ solution. The

bottom layer was a glass bottle full of dry fluorine gas. Fig. 5.8 shows the cross section of the model tested in the 1.5T MRI system. According to the standard ratio of proton phantom, the ratio of $CuSO_4$ to water was 1.96: 1000. Therefore, the mass ratio of $CuSO_4$: water was 3.83g:1950g.

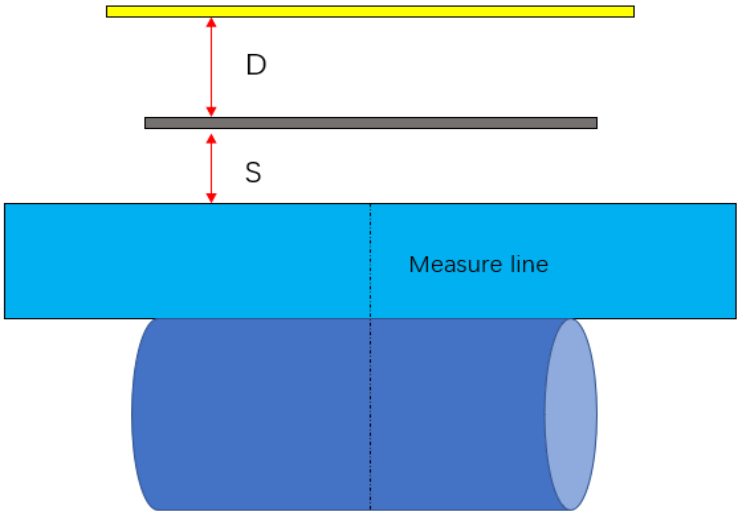

Fig. 5.8 Cross section of the RF transceiver system with dual layer phantom

Fig. 5.9 (a) shows the photograph of the system and Fig. 5.9 (b) shows the ^{19}F phantom, i.e. a glass bottle with diameter of 8.6cm and length of 14 cm. The fluorine phantom was fixed under the hydrogen phantom by foam board on two sides. Fig. 5.10 (a) shows the dual-loop coil used for the metasurface case, and there was only one feed point on the outer coil. Fig. 5.10 (b) shows the single loop coil used as single tuned coil. The settings of the MRI scanner are shown in Table 5.1.

(a) (b)

Fig. 5.9 (a) RF transceiver system in the 1.5T MRI scanner, (b)fluorine phantom

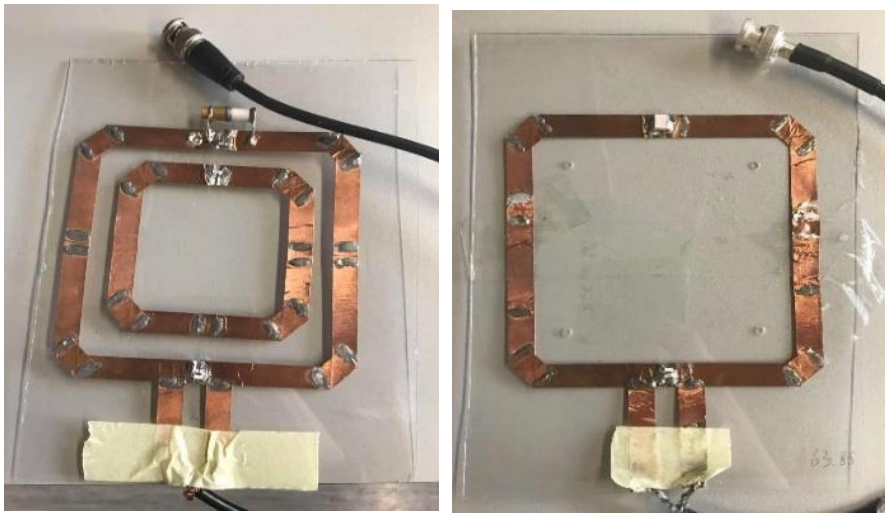

(a) (b)

Fig. 5.10 Manufacutred RF coil (a) in dual loop, (b) in single loop

In the case with the metasurface, the RF coil was placed 30mm away from the hydrogen phantom surface, and the metasurface was placed 5mm away from the hydrogen phantom surface. When the metasurface was absent, the single tuned coils (tuned at 60.08MHz or 63.85MHz) were tested on the hydrogen phantom surface.

Parameter	Value
Pulse repetition time (ms)	400
Echo time (ms)	8.6
Bandwidth (kHz)	2.00
Field of view (cm)	30×30
Slices	16
Acquisition matric (pixels)	32×32
Tesla	1.5
Transmitting power (W)	816

Table 5.1 Parameters of the 1.5T MRI scanner

5.4.1.1 Measured S-parameter in lab

Firstly, the coils were tested in lab environment to measure their S-parameter to make sure all of them were matched to a 50Ω source. Fig. 5.11 shows the S_{11} results after tuning and matching. The dual loop coil with metasurface provided a wide band covering both 60.08MHz and 63.85MHz, and a minimum reflection coefficient of 15dB was achieved. The tuning capacitance was selected as C_1=10 pF, C_2=33 pF the on outer coil and C_3=2.2pF on the inner coil with a matching capacitance Cm=68pF for the dual loop coil when the metasurface was present. The tuning capacitance was selected as C_1=2.2pF and C_2=33pF with a matching capacitance Cm=100pF for the single loop coil tuned at 60.08MHz. The tuning capacitance was selected as C_1=30pF with a matching capacitance C_m=100pF for the single loop coil tuned at 63.85MHz. Tuning and matching were conducted by a one-port calibrated R&S ZVL vector network analyzer.

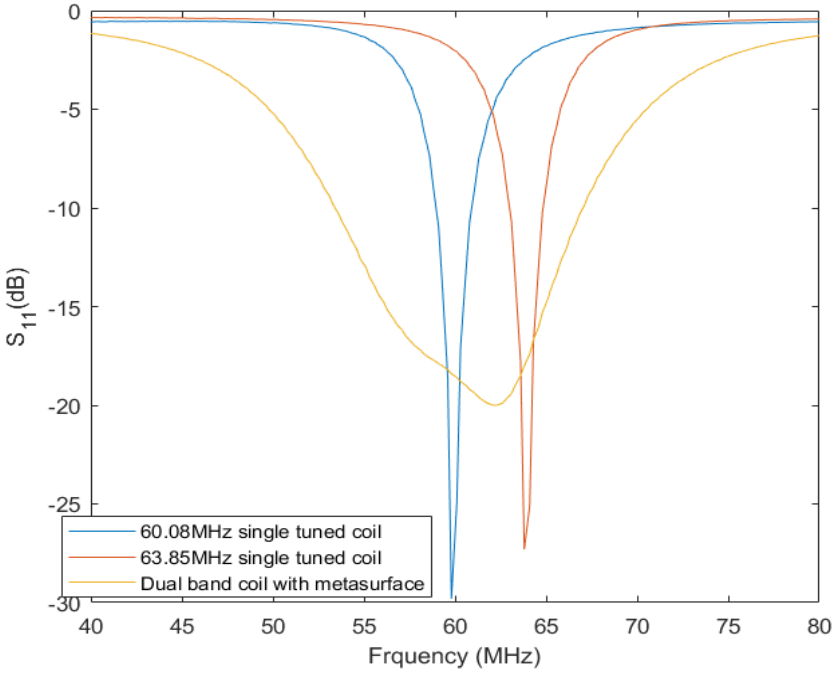

Fig. 5.11 Measured S_{11} RF coil in RF bench

In the experiment, S_{21} was measured at 60.08 MHz and 63.85 MHz by the second coil with diameter of 3cm, which was placed on the hydrogen phantom surface and the fluorine phantom surface separately. The second coil had negligible effects on the measured magnetic field due to its small volume.

Fig. 5.12 shows the S_{21} results when the second coil was placed on the hydrogen phantom surface, in order to estimate the transmission performance for ^{1}H imaging. Comparing the S_{21} at 63.85MHz of the dual loop coil with metasurface with the single loop coil tuned at 63.85MHz, it was found that S_{21} was increased from -23.1dB to -17.8dB by adding the metasurface. The S_{21} of the single loop coil tuned at 60.08MHz for ^{19}F imaging was around -30.1dB due to poor matching.

Fig. 5.13 shows the S_{21} results when the second coil was placed on the ^{19}F phantom surface, in order to estimate the transmission performance across the sample for ^{19}F imaging. This result is correlated to the simulation result shown in Fig. 4.27 and Fig. 4.28. The difference between simulation results and measurement results is because the receiving probe is placed on be ^{1}H phantom surface in the simulation when resonant

frequency was tuned to 63.85MHz. The overall S_{21} decreased a lot compared with the S_{21} results shown in Fig. 5.12, because the total transmission distance increased, and there were some power losses in the hydrogen phantom. The improvement was approximately 3.6dB by comparing the S_{21} at 60.08MHz of the dual loop coil with metasurface with the single loop coil tuned at 60.08MHz. The S_{21} of the single loop coil tuned at 63.85MHz was less than -42dB.

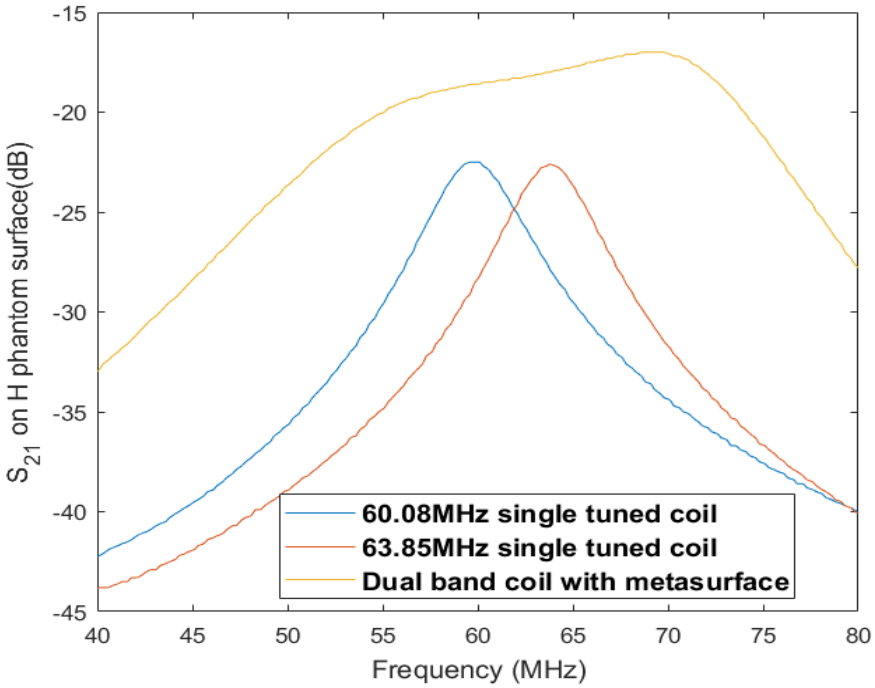

Fig. 5.12 Measured S_{21} results on the ^{1}H phantom surface

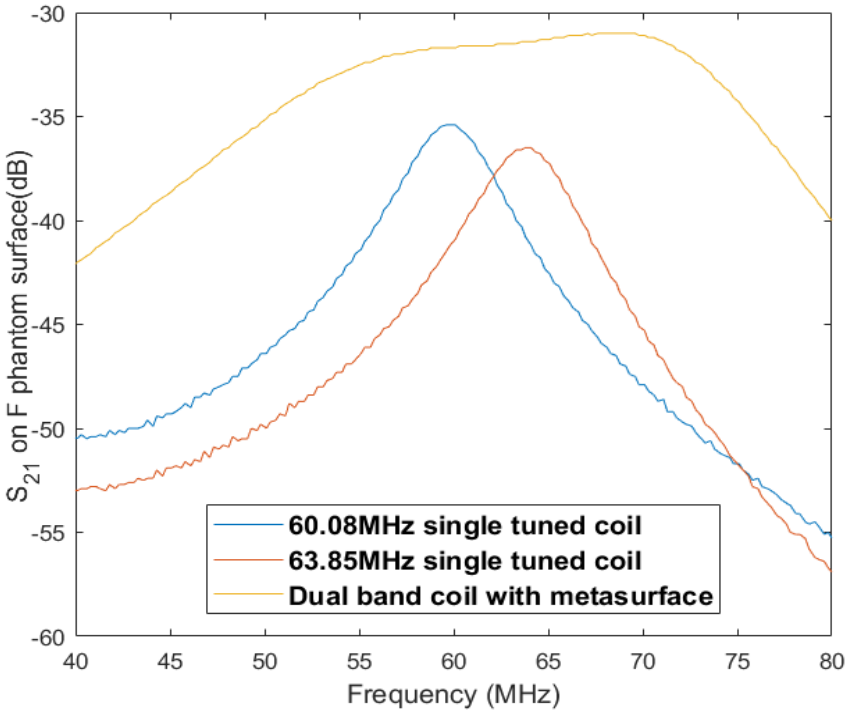

Fig. 5.13 Measured S_{21} results on the ^{19}F phantom surface

5.4.1.2 Measured SNR in MRI

Then, the full system was tested in a 1.5T MRI scanner (GE HDx Milwaukee, USA). The multi-slice 2D spoiled gradient echo pulse sequence was used to conduct ^{1}H imaging, and 3D spoiled gradient echo was used to conduct ^{19}F imaging.

When the resonance frequency of the RF pulse was tuned to 63.85MHz, only the hydrogen phantom could be imaged. Fig. 5.14 gives the SNR results during the hydrogen imaging. The case with the metasurface showed obvious improvement compared to the case of placing 63.85MHz single tuned coil on the phantom surface. The SNR intensity on the surface was increased by 10%. From Fig. 5.14(b), it was clear that the image quality was very poor due to the resonance frequencies of RF pulse and RF coil were poorly matched, which also corresponded to the S_{21} results.

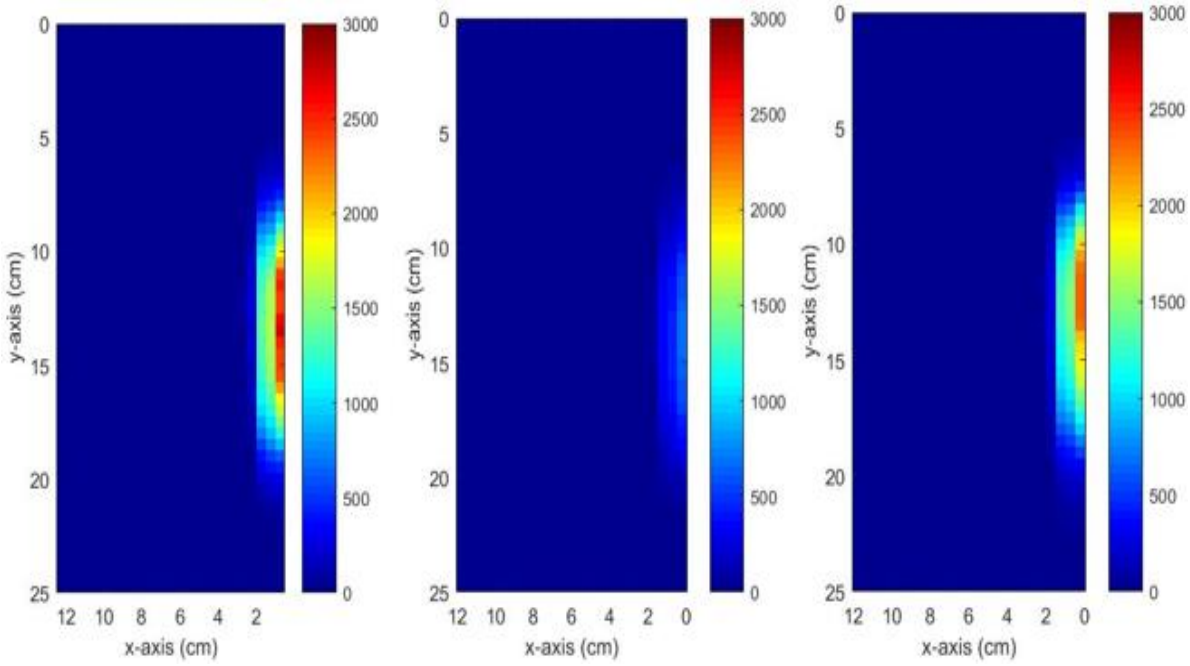

(a) (b) (c)

Fig. 5.14 Measured SNR results at the coil centre for proton imaging. (z=0). (a) Dual loop coil with metasurface. (b) Single loop coil tuned at 60.08MHz. (c) tuned at 63.85MHz

The SNR was also investigated by the linear results, which mearsured by a mearsure line through the centre of ^{1}H phantom surface to the backsurface of ^{19}F phantom. Fig. 5.15 shows the different decay trends of SNR and the enhancement in SNR around the ^{1}H phantom surface. The SNR intensities of all cases were decayed to about zero by 2cm, as the thickness of the hydrogen phantom was 2 cm. The SNR of dual loop coil with metasurface was 2378 on the phantom surface, the SNR of 60.08MHz single tuned coil was 803 and the SNR of 63.85MHz single tuned coil was 2152.

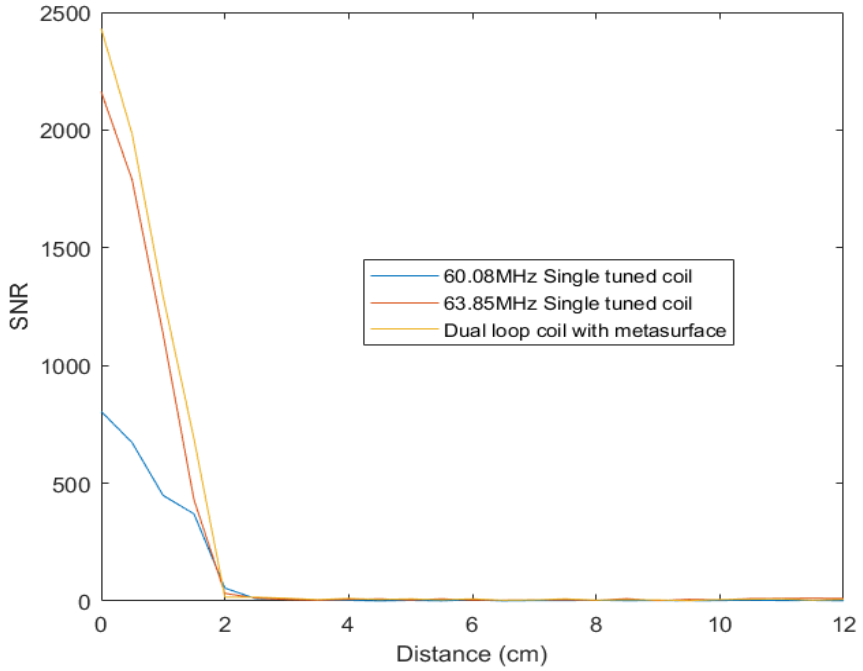

Fig. 5.15 Measured SNR results in linear form for proton imaging

Fig. 5.16 shows the SNR of each model with the resonant frequency of RF pulse being 60.08MHz. It is obvious that the SNR of fluorine imaging was much different from that of hydrogen imaging. Firstly, the resolution of fluorine imaging was lower, because of the nature of ^{19}F NMR and spin density. Then, the highest intensity of hydrogen imaging was around the surface of hydrogen phantom, while the highest intensity of fluorine imaging was around the centre of the ^{19}F phantom. This phenomenon resulted from the 'partial voluming' effect, which could be mitigated with smaller pixels such as the pixels in ^{1}H. Namely, for the first two pixels, only half or less of the actual voxel volume would contain ^{19}F gas which the SNR was directly proportional to. However, we can still find out that the metasurface provided remarkable enhancement in overall SNR from Fig. 5.16.

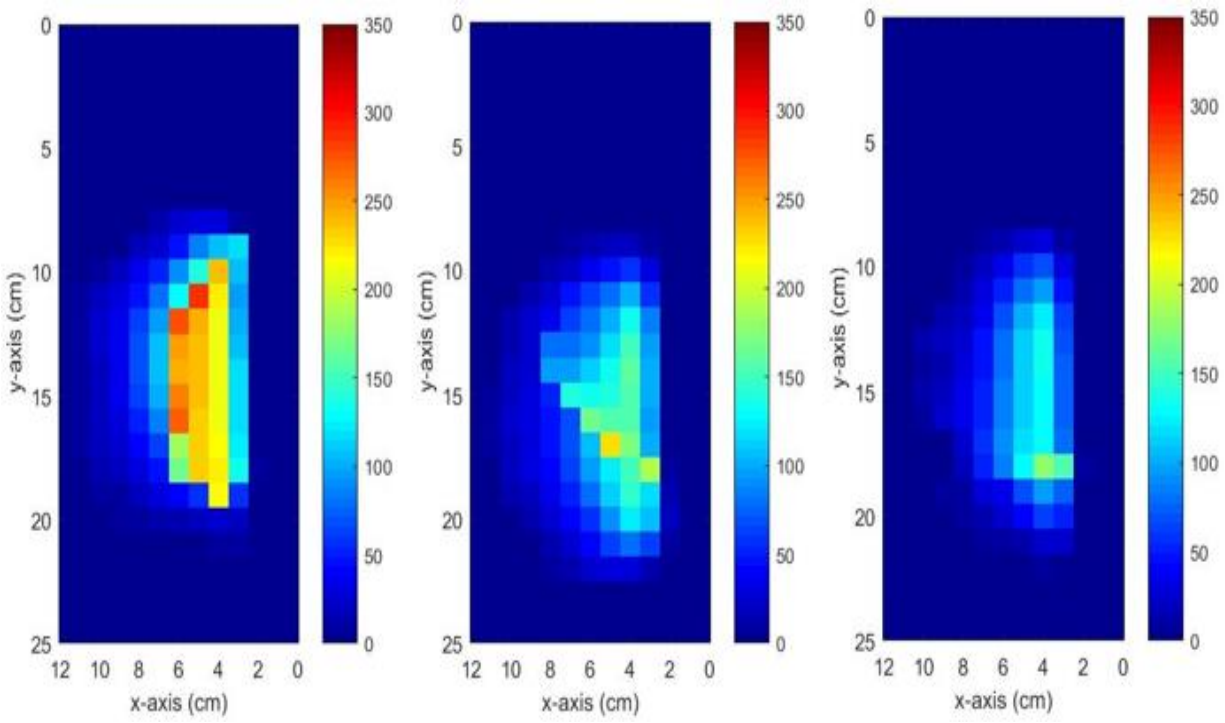

(a) (b) (c)

Fig. 5.16 Measured SNR results for fluorine imaging. (z=0). (a) Dual loop coil with metasurface. (b) Single loop coil tuned at 60.08MHz. (c) tuned at 63.85MHz

The linear results of SNR for fluorine imaging are shown in Fig. 5.17. It was hard to make fair comparison by comparing the SNR around fluorine phantom surface in each case, because the SNR started increasing on the fluorine phantom surface. The diameter of the glass bottle full of fluorine was 8.6cm, so the SNR started increasing at 2cm, and decayed to about 0 at about 10.6cm. The peak value of SNR of the dual loop coil with the metasurface was 227 on the phantom surface, the highest SNR of the 60.08MHz single tuned coil was 173 and the highest SNR of the 60.08MHz single tuned coil was 131.

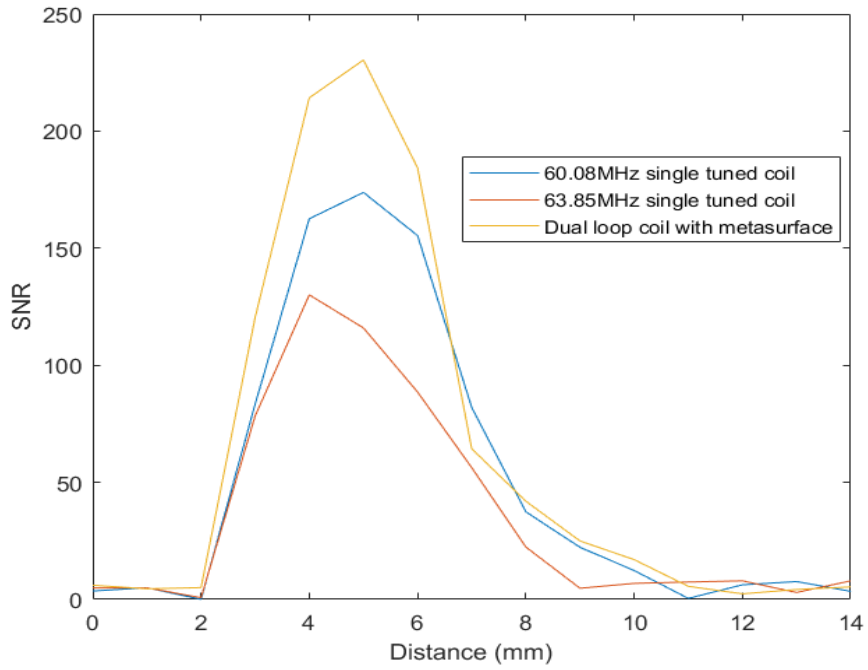

Fig. 5.17 Measured SNR results in linear form for fluorine imaging

5.4.1.3 Measured flip angle in MRI

Further, the enhancement provided by the metasurface can be also characterized by the flip angle α apart from SNR. The definition of flip angle has been discussed in details in chapter 3. The results of flip angle during the hydrogen imaging are shown in Fig. 5.18. As proved in the previous subsection, flip angle is proportional to SNR, so higher flip angle under the same transmitting power always means higher SNR and better transmission performance. From the flip angle results, the additional metasurface also helped to increase the entire flip angle, but the effective area was smaller than that of the 63.85MHz single tuned coil case, due to the strong focusing performance provided by the metasurface.

Fig. 5.19 gives the results of the flip angle of fluorine imaging. The metasurface shows a good performance to improve the flip angle around central area around the fluorine phantom surface. The single loop coil tuned at 60.08MHz had considerable effective area, although the flip angle around the phantom surface was lower than that with the

metasurface.

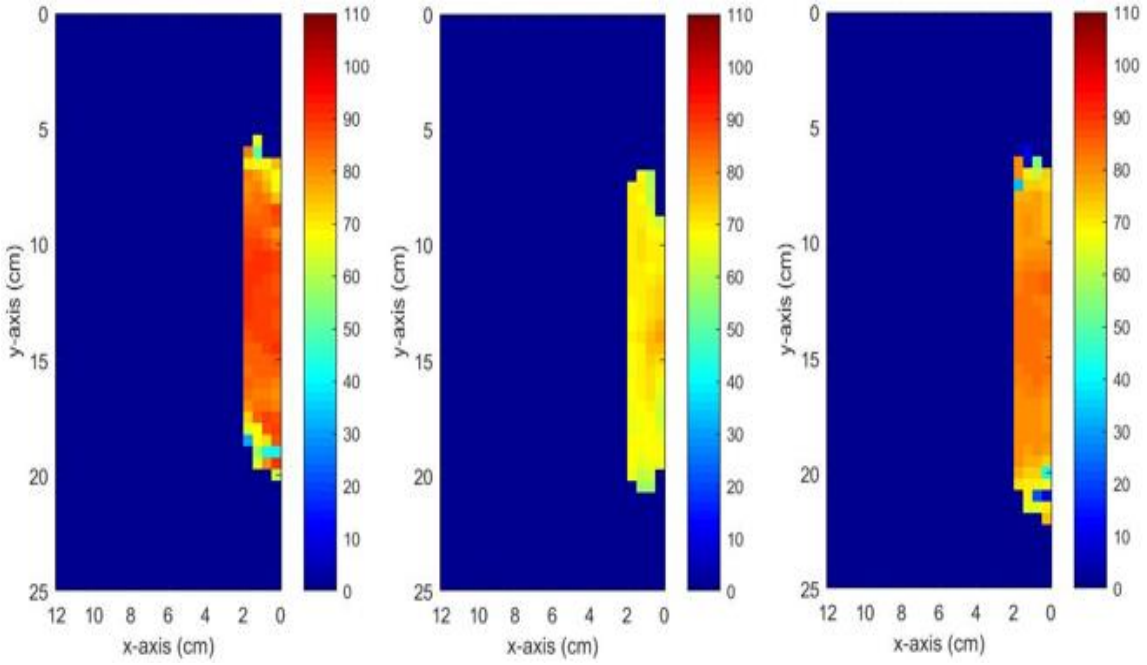

(a) (b) (c)

Fig. 5.18 Flip angle map for proton imaging. (z=0). (a) Dual loop coil with metasurface. (b) Single loop coil tuned at 60.08MHz. (c) tuned at 63.85MHz

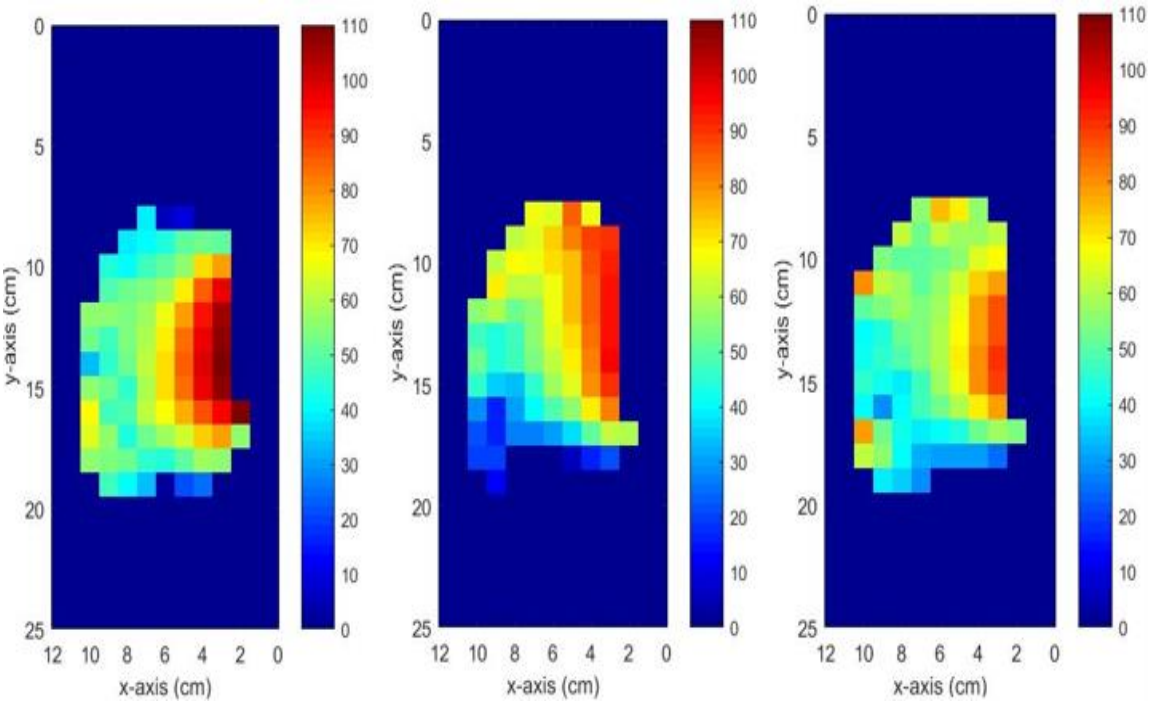

(a) (b) (c)

Fig. 5.19 Flip angle map for fluorine imaging. (z=0). (a) Dual loop coil with metasurface. (b) Single loop coil tuned at 60.08MHz. (c) tuned at 63.85MHz

5.4.1.4 Measured receiver sensitivity in MRI

The receiver sensitivity of each case can be compared by measuring the receiver sensitivity which normalizes SNR to the sine of the flip angle at each *x*-*y* pixel. The definition of the receiver sensitivity has been discussed in chapter 3. The receiver sensitivity in each case had totally the same trend as the SNR, but some got extra improvement, such as the area around the phantom surface in 63.85MHz single tuned coil case, as indicated from Fig. 5.20.

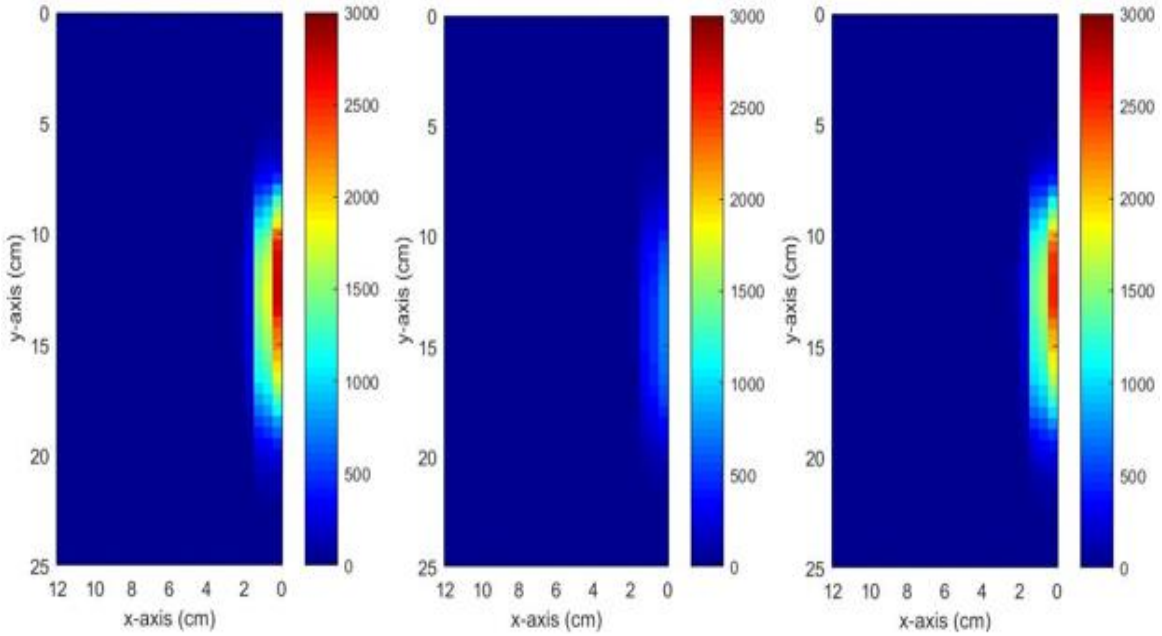

(a) (b) (c)

Fig. 5.20 Receiver sensitivity for proton imaging. (z=0). (a) Dual loop coil with metasurface. (b) Single loop coil tuned at 60.08MHz. (c) tuned at 63.85MHz

Similar to the receiver sensitivity of hydrogen imaging case, the overall receiver sensitivities of fluorine imaging were almost the same as the SNR results in Fig. 5.16. The receiver sensitivity of single loop coil tuned at 60.08MHz got more improvement around the fluorine surface shown in Fig. 5.21, as it had more improvement in flip angle around the fluorine phantom surface as shown in the last case.

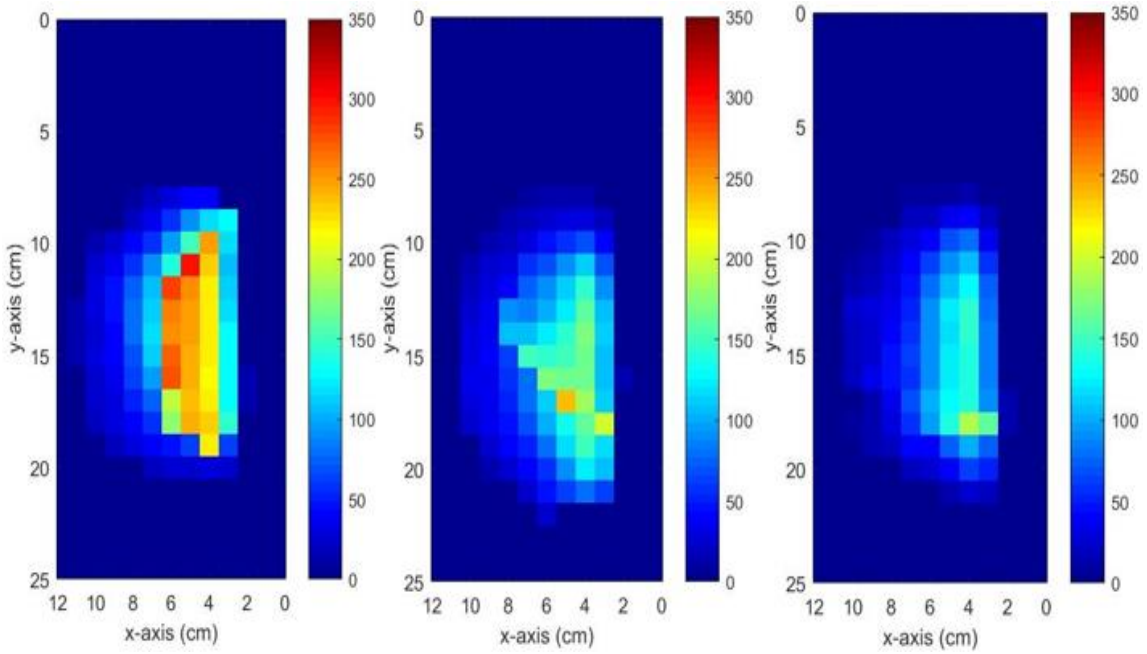

(a) (b) (c)

Fig. 5.21 Receiver sensitivity for proton imaging. (z=0). (a) Dual loop coil with metasurface. (b) Single loop coil tuned at 60.08MHz. (c) tuned at 63.85MHz

5.4.2 Embedded structure phantom

The other structure is the 'embedded structure' to represent real human body, where a plastic bag, filled with fluorine, was placed inside the hydrogen phantom which was a cuboid container full of $CuSO_4$ solution. The cross section of the whole MRI system contained 'embedded structure' phantom is shown in Fig. 5.22. Fig. 5.23 shows the image of the phantom. The thickness L of the fluorine phantom was about 50mm. The linear results of SNR can be presented in a more clear manner if these parameters were displayed in the scale. The tuning capacitance was set as C_{t1}=2.2pF, C_{t2}=4.7pF and C_{t3}=22pF on the outer coil and C_{t4}=3.3pF on the inner coil with two matching capacitances of C_{m1}=68pF and C_{m2}=100pF for dual loop coil when the metasurface was present. The tuning capacitance was set as C_{t1}=33pF with two matching capacitances of C_{m1}=150pF and C_{m2}=33pF for single loop coil tuned at 60.08MHz. The tuning capacitance was set as C_{t1}=27pF, with two parallel matching capacitances of

C_{m1}=150pF and C_{m2}=33pF for single loop coil tuned at 63.85MHz.

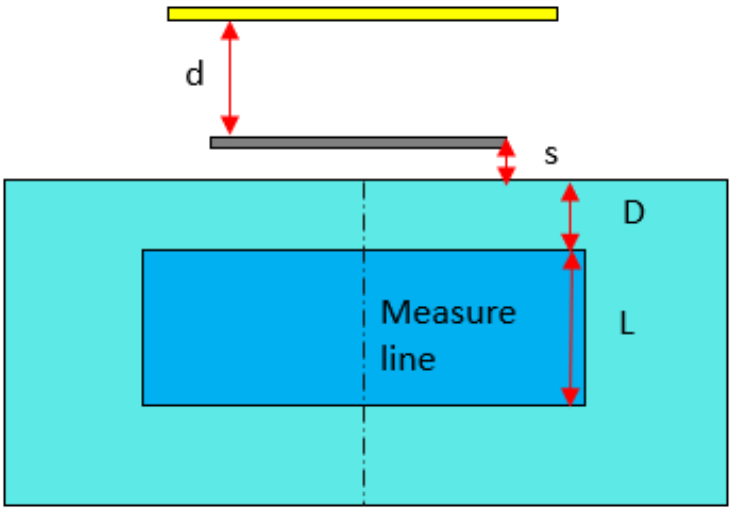

Fig. 5.22 Cross section of ‘embedded structure phantom ‘configuration tested in the 1.5T MRI system

Fig. 5.23 Cross section of ‘embedded structure phantom’ in lab

5.4.2.1 Measured S-parameter in lab

Fig. 5.24 shows the S_{11} results after tuning and matching. In this case, the dual band provided by the metasurface became more obvious. The gap between the two bands could be adjusted by changing the space between the coil and hydrogen phantom surface. After the adjustment, the space d between the coil and hydrogen phantom surface was set as 40mm, to make sure that both bands at 60.08MHz and 63.85MHz had the minimum reflection coefficient of -17dB.

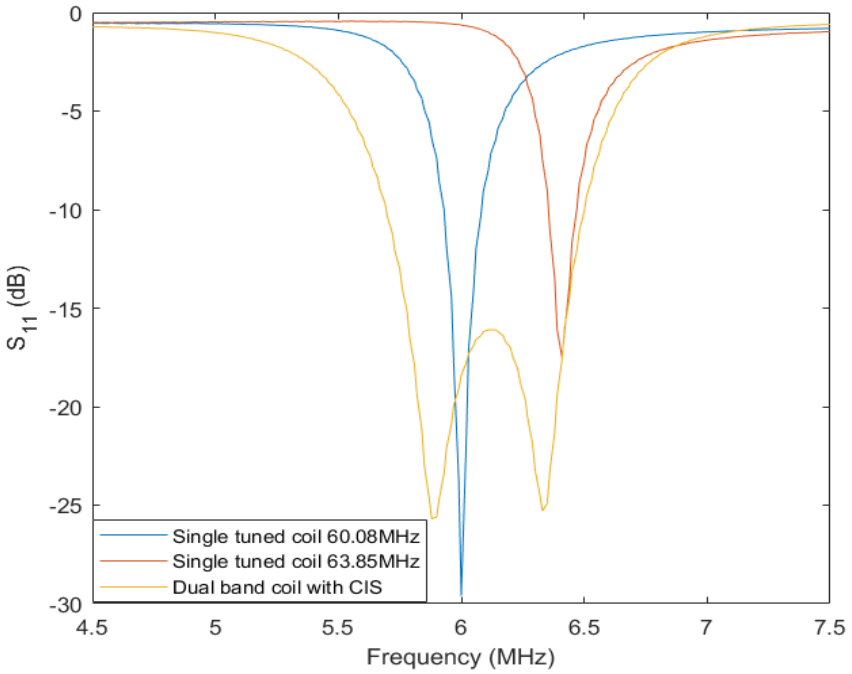

Fig. 5.24 Measured S_{11} results in RF bench

As the fluorine phantom was placed inside the hydrogen phantom, the S_{21} on the fluorine phantom could not be measured in this case. Fig. 5.25 shows the S_{21} on the hydrogen phantom surface. The S_{21} at 63.85MHz was improved from -18.2dB to -14.5dB by comparing the dual loop coil with metasurface and the single loop coil tuned at 63.85MHz. Further, the transmission performance at 60.08MHz was predicted by comparing the S_{21} at 60.08MHz on the hydrogen phantom surface, which was improved from -18.6dB to 15.1dB by comparing the dual loop coil with metasurface and the single loop coil tuned at 60.08MHz.

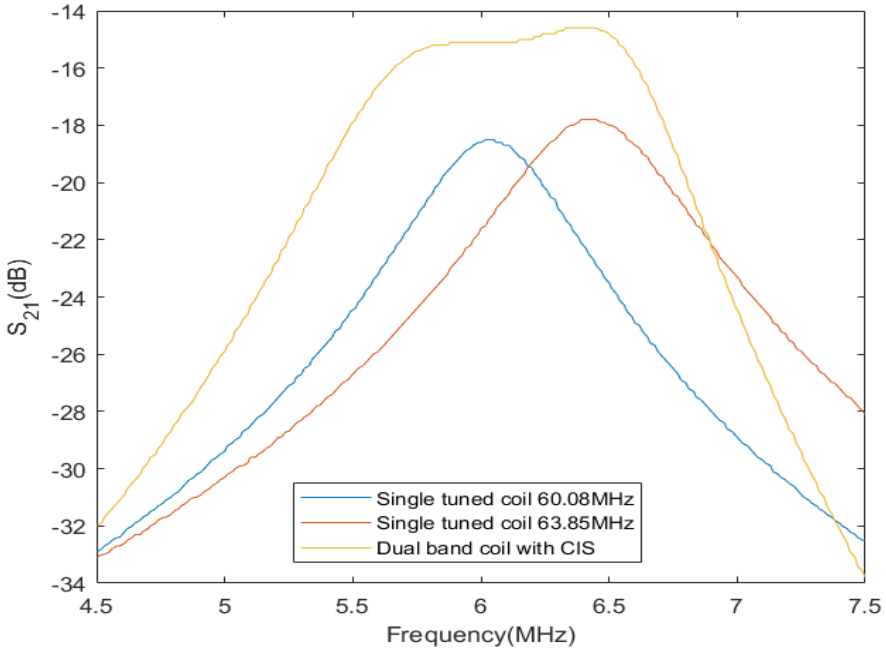

Fig. 5.25 Dual band property of the non-periodic metasurface

5.4.2.2 Measured SNR in MRI

The 2D results of SNR are shown in Fig. 5.26, with the resonance frequency of RF pulse from MRI being 63.85MHz. The enhancement provided by the metasurface can be pointed out more clearly. When the resonance frequency of RF coil was not matched to the resonance frequency of the nuclei used for imaging, the SNR will be dropped. From Fig. 5.26(b) and Fig. 5.26(c), when the resonance frequency was tuned from 60.08MHz to 63.85MHz, and the intensity of SNR increased slightly. When the metasurface was placed between the RF coil and phantom, there was an obvious enhancement in SNR around the phantom surface. The SNR results in all cases were decayed to 0 before 3.3cm due to the fluorine phantom, which was imaged by the RF inpulse at 60.08MHz. The imaging area along *y*-axis was similar in each case.

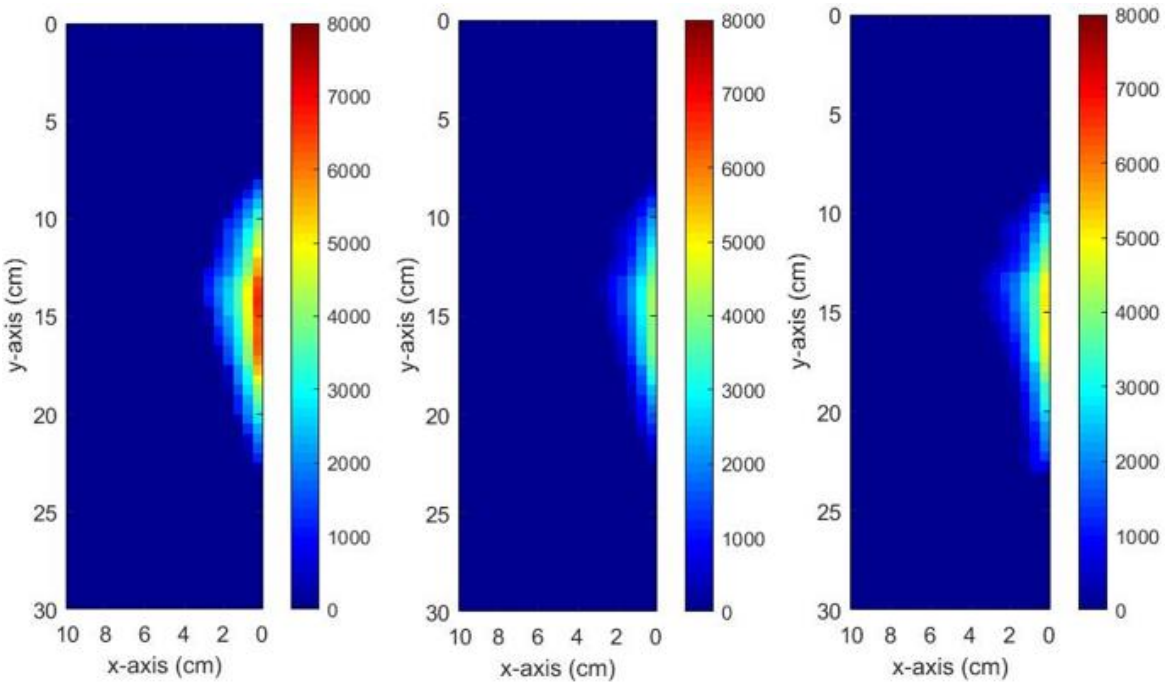

(a) (b) (c)

Fig. 5.26 Measured SNR results for proton imaging. (z=0). (a) Dual loop coil with metasurface. (b) Single loop coil tuned at 60.08MHz. (c) tuned at 63.85MHz

Fig. 5.27 gives the linear results of SNR when the MRI scanner conducted hydrogen imaging at the resonance frequency of 63.85MHz. The *x*-axis represents the distance along the cross section of the phantom, and the starting point is at the centre of the hydrogen phantom surface. It is clear that the surface coil with metasurface had the highest SNR which close to 6900. The single tuned coil with resonance frequency tuned to 63.85MHz had higher SNR (about 5200) than the single tuend coil with resonance freuqency tuned to 60.08MHz (about 4200). Then, the SNR in all cases decayed to 0, when the coordinate of *x* was close to 3.3cm, which was similar to the distance between hydrogen phantom surface and fluorine phantom surface D. From the results of hydrogen imaging, the SNR on the phantom surface was increased by 32.6% after the metasurface was added compared to the single tuned coil with resonance frequency tuned to 63.85 MHz.

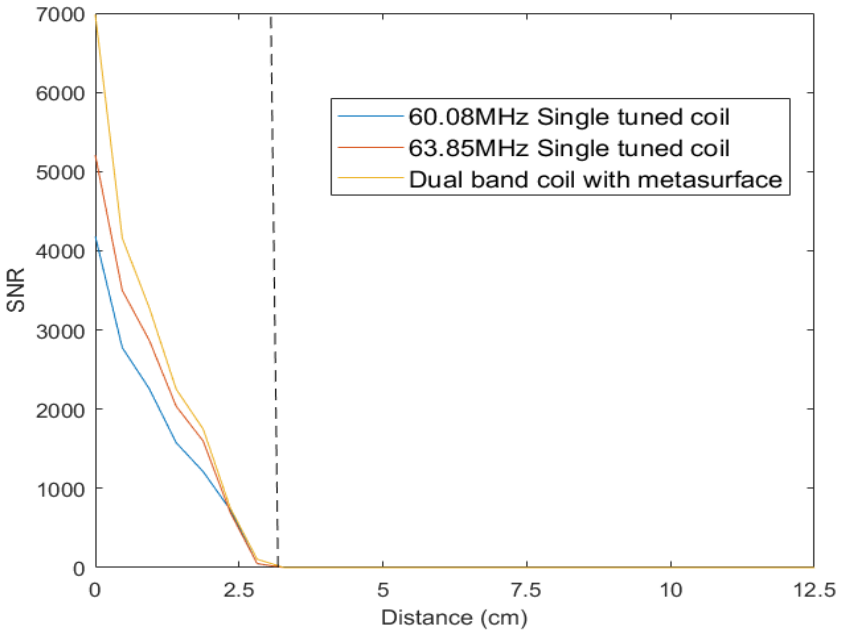

Fig. 5.27 Measured SNR results in linear form for proton imaging

Fig. 5.28 shows the measurement results of SNR on the *x*-*y*-plane with and without placing the metasurface between the coil and phantom, when the RF pulse from MRI was at 60.08MHz. In this case, only the fluorine phantom which was 3.3cm away from the hydrogen phantom surface was imaged. It is obvious that when the resonance frequency of single coil was not tuned at 60.08MHz, the imaging area and intensity of SNR were decreased as indicated by Fig. 5.28 (c). The mesurface also showed a good performance in improving the SNR without decreasing the imaging area compared to the cases in absence of metasurface.

Fig. 5.29 shows the linear results of SNR when the MRI scanner conducted fluorine imaging at resonant frequency of 60.08MHz. The SNR of each case started at 3.3cm which was the top surface of the fluorine phantom, and ended at 9.3 cm which was the back surface of the fluorine phantom. The enhancement in SNR by adding metasurface covered a long penetration depth, compared to the cases in the absence of metasurface.

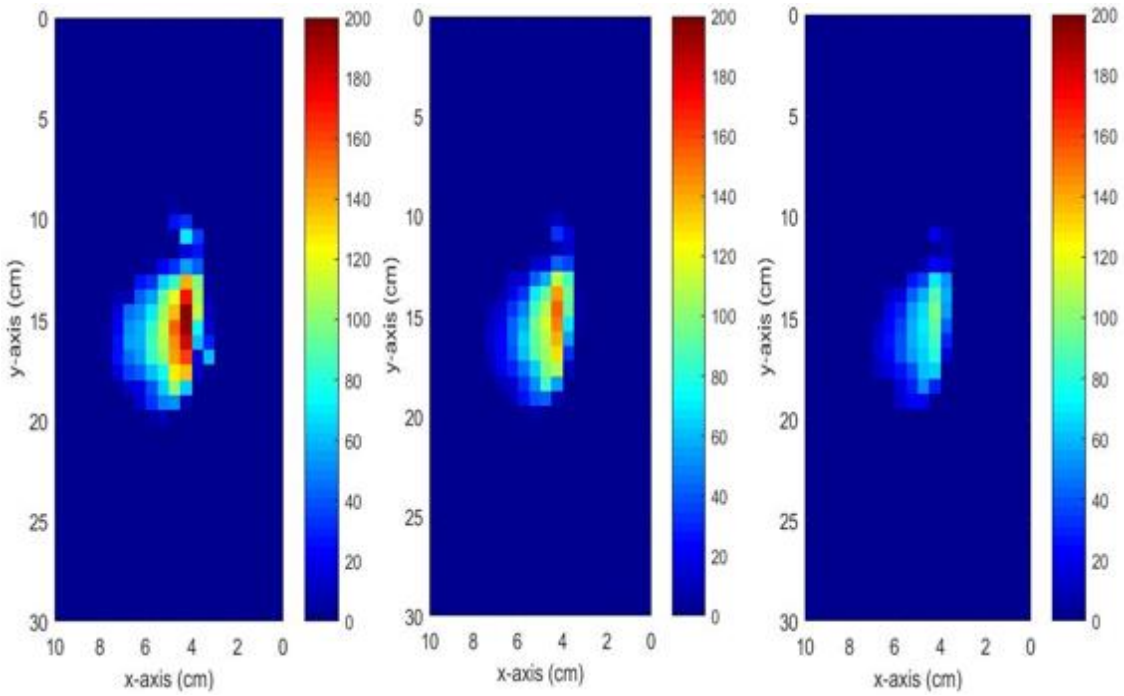

(a) (b) (c)

Fig. 5.28 Measured SNR results for fluorine imaging. (z=0). (a) Dual loop coil with metasurface. (b) Single loop coil tuned at 60.08MHz. (c) tuned at 63.85MHz

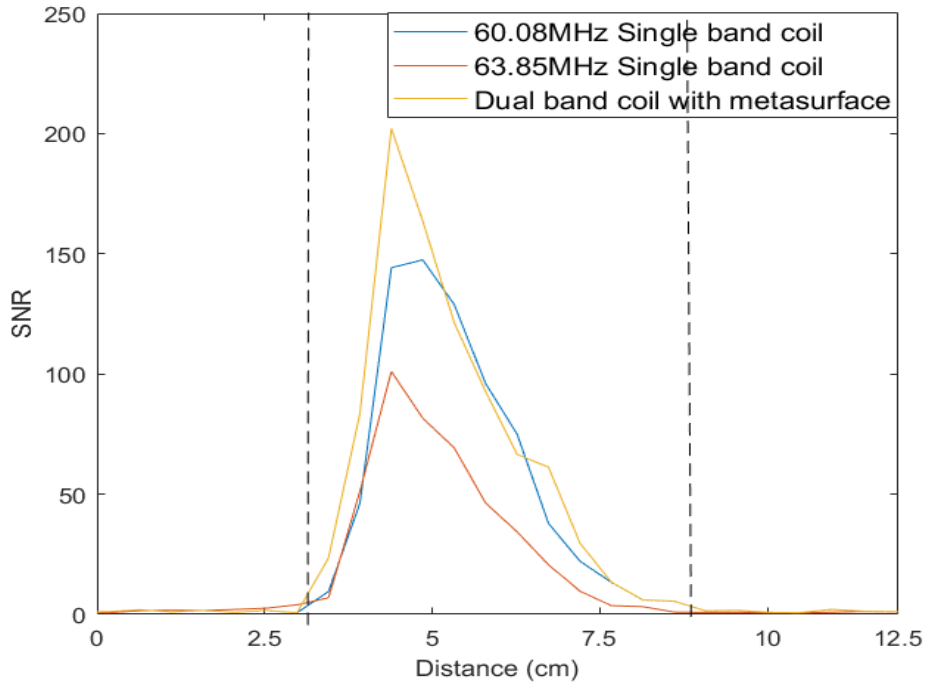

Fig. 5.29 Measured SNR results in linear form for fluorine imaging

5.4.2.3 Measured flip angle in MRI

Fig. 5.30 gives the full flip angle maps when conducting hydrogen imaging under the same transmitting power of (a) with metasurface, (b) single tuned RF coil at 60.08MHz and single tuned RF coil at 63.85MHz. There was an obvious shadow ‘circle’ in the middle of Fig. 5.30, which was the fluorine phantom. Fluorine phantom could only be imaged by the RF pulse at 60.08 MHz. There were no significant differences in the results of flip angle between the single tuned coils at different resonant frequencies, and the metasurface still showed good performance in improving the flip angle around the hydrogen phantom surface. The size of the imaged area was similar in each case.

Fig. 5.31 illustrates the results of the full flip angle maps when conducting the fluorine imaging under the same transmitting power of (a) with metasurface, (b) single tuned RF coil at 60.08MHz and (c) single tuned RF coil at 63.85MHz. In this case, the RF pulse was at 60.08MHz, and only the fluorine phantom inside the hydrogen phantom was imaged. According to the results, the metasurface showed good performance in improving the flip angle around the fluorine phantom surface, and also increased the imaged area compared to the single tuned coil. It can be seen that, in fluorine nuclei imaging, the image quality and imaged area were significantly reduced when the resonant frequency of the surface coil was not matched with the RF pulse.

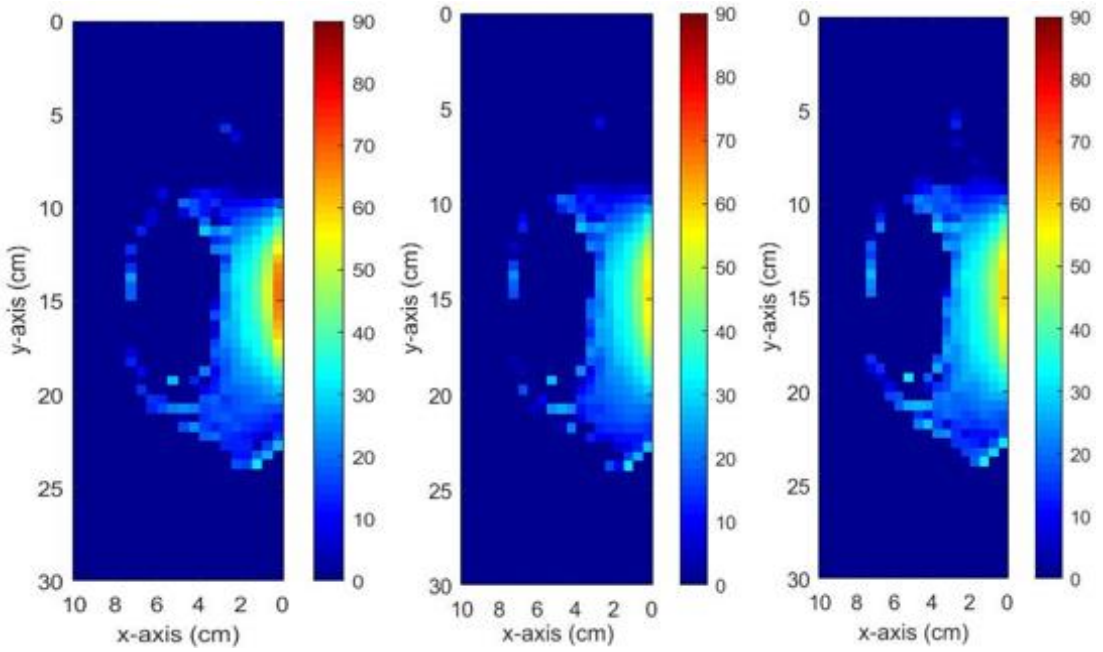

(a) (b) (c)

Fig. 5.30 Flip angle map for proton imaging. (z=0). (a) Dual loop coil with metasurface. (b) Single loop coil tuned at 60.08MHz. (c) tuned at 63.85MHz

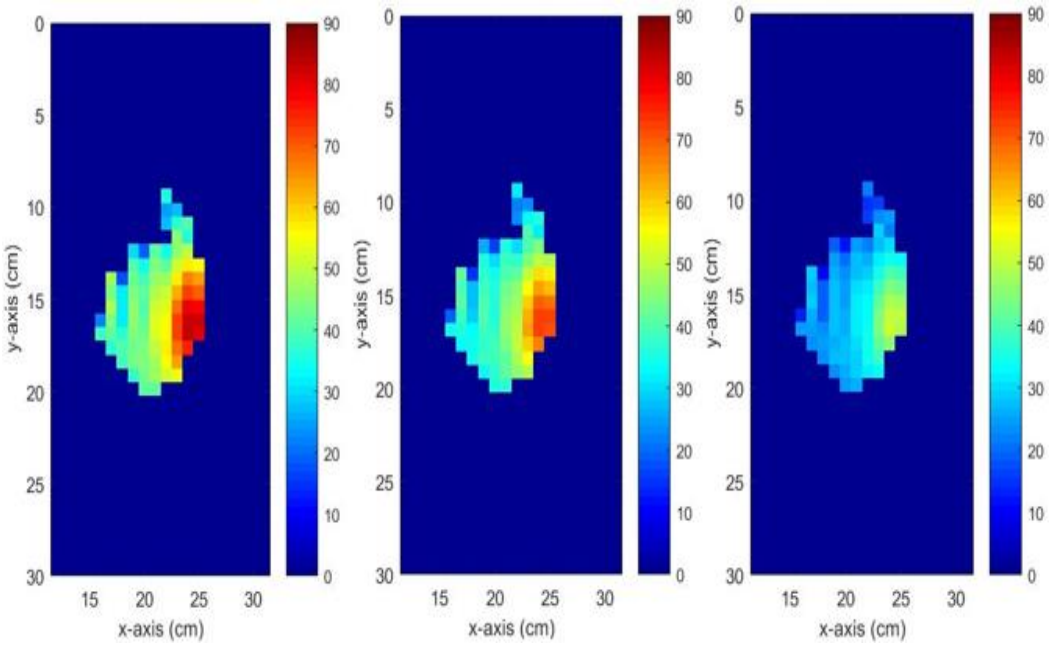

(a) (b) (c)

Fig. 5.31 Flip angle map for fluorine imaging. (z=0). (a) Dual loop coil with metasurface. (b) Single loop coil tuned at 60.08MHz. (c) tuned at 63.85MHz

5.4.2.4 Receiver sensitivity in MRI

The receiver sensitivity of the hydrogen imaging in this case is illustrated in Fig. 5.32. All of the cases had similar trend as the SNR results shown in Fig. 5.26. The dual loop coil with metasurface showed large enhancement in transmission efficiency than the single loop coils.

Fig. 5.33 also gives the receiver sensitivity of the fluorine imaging. It is clear that the receiver sensitivity got large improvement by adding the metasurface, and the effective imaging area was increased.

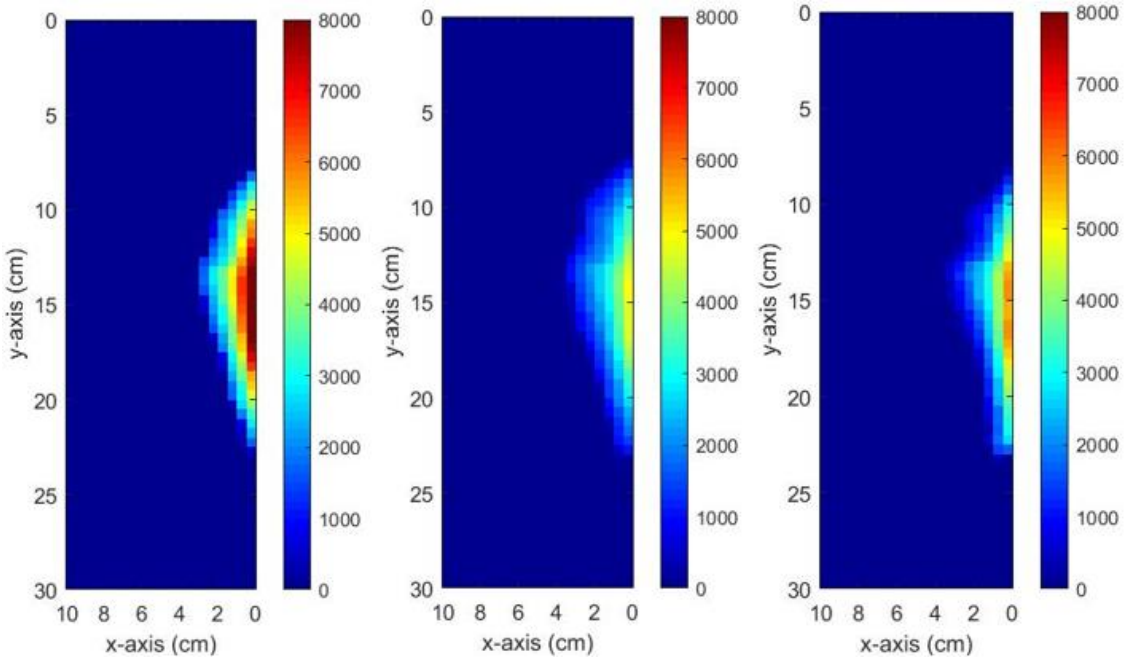

(a) (b) (c)

Fig. 5.32 Receiver sensitivity for proton imaging. (z=0). (a) Dual loop coil with metasurface. (b) Single loop coil tuned at 60.08MHz. (c) tuned at 63.85MHz

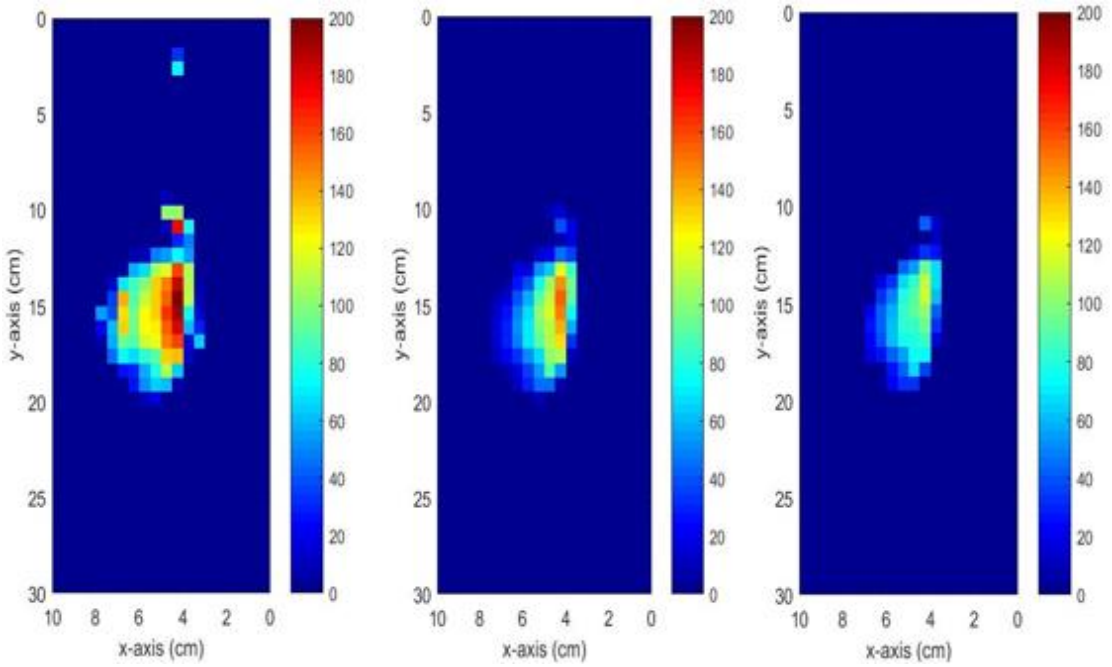

(a) (b) (c)

Fig. 5.33 Receiver sensitivity for fluorine imaging. (z=0). (a) Dual loop coil with metasurface. (b) Single loop coil tuned at 60.08MHz. (c) tuned at 63.85MHz

5.5 Summary

In this work, a novel non-periodic metasurface is proposed for generating extra band with a single RF fed dual loop surface coil, which has been demonstrated by both simulations and experiments. The surface coil used in this case was dual loop coil, but there was only one fed on the outer coil. Numerical simulations showed that the metasurface provided comparable performance at 60.08MHz for ^{19}F applications, and achieved a maximum improvement of 27% at 63.85MHz in $|B_1^+|$, because of its dual band property.

The metasurface design of l=97.1 mm, g_d =0.8 mm, w_d =1.8 mm was manufactured and tested in a 1.5T MRI scanner. Two different phantom configurations were tested in the 1.5T MRI scanner, which was ‘dual layer’ phantom and ‘embedded structure’ phantom. Firstly, the RF transceiver system was tested with the ‘dual layer’ phantom. The results from the two-port VNA system showed that improvements of 3.9dB and 5.3dB were achieved by adding the metasurface in the RF coil at 60.08MHz and 63.85MHz

respectively. The SNR results of ‘dual layer’ phantom configuration showed that the metasurface provided an increase of 9.2% on the fluorine phantom surface, and 34.1% on the hydrogen phantom surface. Then, the transceiver system was tested with the ‘embedded structure’ phantom. Experimental results showed that increases of 3.9dB and 5.4dB were achieved in receiving signals when the transceiver system was tested with ‘embedded structure’. The SNR results of ‘embedded structure’ phantom showed that the metasurface provided an increase of 37.9% on the fluorine phantom surface, and 32.7% on the hydrogen phantom surface. These enhancement in SNR cover the whole penetration depth. Compared with previous research on multi-nuclei MRI optimization, only one fed was required in this case, which avoided the losses caused by the coupling between the coils, such as trap circuit coil. Compared with the applications of metamaterials in multi-nuclei MRI, the non-periodic metasurface used in this case did not require a complex design of metasurface for focused resonance frequency. The small and flexible dimension of the metasurface resulting from its non-periodic structure is also an attractive point. From the both simulation and experimental results, the non-periodic metasurface provided even field decay inside the dielectric phantom.

Chapter 6

Conclusion

Two main independent and complete works were carried out in this thesis. One is enhancing the magnetic flux density B_1 and SNR for the ^{1}H imaging (resonance frequency is 63.85 MHz) in a 1.5 T MRI system by applying a non-periodic structure metasurface. The other is achieving the ^{19}F and ^{1}H imaging by a single RF fed, with a metasurface placed between the RF coil and the dielectric phantom. Both two achievements include numerical simulations and complete measurement results from the 1.5 T MRI scanner to prove their effectiveness. This chapter introduces the main content and key information of each chapter, and points out the difference, improvement and novelty by the comparison with existing research.

Chapter 1 provides an introduction of the research contents and defines the problems in the development of MRI systems. Thesis aims, novelty and contributions are demonstrated. The background, working principle and imaging procedures of the MRI systems are introduced to provide a clear understanding of the focused area. In this case,

the main components and their functions in MRI systems are introduced, such as RF coil. The key parameters that define the imaging quality of MRI systems have also been discussed, especially the SNR.

Chapter 2 provides the literature review is conducted on the researched field. The use of metamaterials to enhance the SNR in single band MRI systems is introduced. Approached are also provided to achieve the multi-nuclei in MRI systems.

Chapter 3 describes a method for designing a non-periodic metasurface for improving the transceiver performance for a rectangular RF surface coil to be used in MRI applications. The initial capacitance of the metasurface is estimated by the 'surface impedance' method which introduce at the beginning of thispart. Then, the initial dimension of the metasurface is estimated by using the equations discussed in this chapter, and the parameters of dimension are adjusted by comparing the B_1^+ and normalized B_1^- in each case. After adjusting the dimension of the metasurface, the positive magnetic flux density $|B_1^+|$ is improved by about 65% at phantom surface, and the normalised magnetic flux density $|B_1^-$ nor$|$ is improved by about 67% with the metasurface of w_d=1.8 mm, g_d=0.8 mm, l=80 mm' placed between the RF coil and the dielectric phantom. After that, the metasurface is manufactured by using a PCB etching technique and tested in the 1.5T MRI system. The SNR on the phantom surface is improved by 133% when the metasurface is present, and the enhancement provided by the metasurface covers the whole penetration depth. From the 2D results of SNR, flip angle and receiver sensitivity, the metasurface shows a good performance in optimizing the 1.5T MRI system without destructive effects to the field.

Compared to the previous research, the most significant novelty of this work is the non-periodic structure. As far as we know, this is the first time to use the non-periodic structure in MRI optimization. Compared with the periodic structure used in MRI systems, such as Swiss rolls, CLRs and HIS, the non-periodic structure has very flexible dimension and simple structure. The biggest problem of the periodic structure is the miniaturization of the structure, as the resonance frequency of the MRI system is always lower than 400MHz. This is also the reason why the optimization work based on metamaterials in high field strength (7T) is more extensively investigated than that in

low field strength (1.5T). The other problem is the destructive effects to the field caused by the surface current flow in the gap between each unit cell in periodic structure, which will generate extra noise and distortion during the imaging. Secondly, most of previous research increases the SNR of MRI systems by focusing the field, but this will also increase the E-field strength which defines the security of the system and is proportional to SAR. From the simulated E-field results, there is no obvious increment in E-field by using the non-periodic metasurface, as the proposed non-periodic metasurface does not optimize the system by focusing the field. From the measurement results from the 1.5T MRI scanner, the proposed metasurface shows a good performance in enhancing the SNR in terms of both strength and effective area, and the enhancement covers the whole penetration depth. This is the other improvement compared with most of previous research.

Chapter 4 proposes a method to achieve dual-band nuclei imaging by placing the non-periodic structure between the single fed RF coil and the dielectric phantom. The dual-band nuclei imaging is an extremely meaningful and valuable topic, because it could dramatically reduce the medical cost and save imaging time. At present, there are some researches on achieving multi-nuclei imaging in different ways, such as changing the RF coil structure, or adding extra resonator structure. However, there is very few researches that can achieve multi-nuclei imaging within the similar RF performance as the single band imaging, because of the extra power losses in additional circuitry or elements. The other problem is that the mutual coupling between each component limiting the focused frequency bands should be in small difference, and based on high field strength to ensure the wavelength is in controllable range. In this case, the dual band property of the non-periodic metasurface is investigated to achieve the dual band imaging for ^{19}F and ^{1}H imaging in 1.5T MRI applications, which is the first time this topic is investigated. From the simulation results, the dual band property of the metasurface is generated by the coupling between the RF coil and the metasurface. Then, the resonant frequencies of the RF transceiver system are tuned easily by the tuning capacitors on the single-fed dual loop RF coil, and adjusted by changing the dimension of the metasurface. From the simulation results, when the metasurface of

l=97.1mm, w_d=1.8mm and g_d=0.8mm is present, the normalised $|B_1^-|$ is increased by 24% on the ^{19}F phantom surface at 60.08 MHz, and 6% on the ^{1}H phantom surface at 63.85 MHz. When the metasurface of l=98mm, w_d=1.8mm and g_d=1mm is present, the normalised $|B_1^+|$ is increased by 102% on the ^{1}H phantom surface, and the same as the single loop coil on the 19F phantom surface. As discussed before, there are currently no techniques that can achieve multi-band nuclei imaging without decreasing the performance on either of resonances. So, this research is a qualitative breakthrough in the multi-nuclei imaging. The measurement results from chapter 5 show the metasurface provides an increase of 9.2% on the ^{19}F phantom surface, and 34.1% on the hydrogen phantom surface during their imaging process.

As a result, the proposed non-periodic metasurface can achieve multi-nuclei to avoid the extra power losses from the mutual coupling on the dual loop coil owing to the single RF fed on the coil; reduce the surface current loss on the metasurface and make the field be uniformly distributed in the phantom owing to its non-periodic structure; optimize the low-field-strength MRI systems with low resonance frequency, which is always limited by the size of periodic structure of the metasurface. Low cost and flexible size are non-negligible advantages compared with all periodic metasurfaces used in MRI systems.

Chapter 7

Future work

The main achievements of this thesis have been concluded in the last section,. This research shows good novelty and improvements compared with the previous research in this field. This section proposes several new areas for future work based on the findings obtained in this thesis.

Firstly, for the optimization work of single band MRI systems, a non-periodic metasurface has been proposed to enhance the SNR at 63.85MHz for 1.5T MRI systems. Compared with the metasurfac with a periodic structure, the non-periodic structure has more flexible dimension, because there is no need to tune the resonance frequency. Therefore, different nucleus with different resonant frequencies in 1.5T MRI systems can be examined, such as ^{19}F (resonant frequency at 60.08MHz) and ^{23}Na (resonant frequency at 16.9MHz). Then, the MRI systems with different field strengths also have big potentials to be enhanced by using non-periodic metasurface. From the literature review, we have known that the RF coils of MRI systems have different types, such as surface coils and volume coils. Volume coils also have many advantages, such as large imaging area and good homogeneity. However, its cylinder dimension has limited the development of most metamaterial-based optimization works, owing to the large

dimension and complex structure. It is possible to apply the non-periodic metasurfaces in four directions to optimize the volume coil, because the dimension of non-periodic metasurface is much less than the volume coil, and the large gap between each metasurface can minimize the mutual coupling between metasurfaces.

Secondly, some other valuable research directions can be considered for multi-nuclei MRI systems. During the simulation, one of the resonance frequencies is controlled by the tuning capacitors on the dual loop coil, and the other resonance frequency is controlled by tuning the tuning capacitors and the dimension of the non-periodic metasurface. This means it is not hard to control the resonance frequencies of this MRI transceiver system, so different nuclei can be considered. During the simulation, it has been found that, when the metasurface is l=100mm, w_d=2mm, g_d=0.8mm, we can achieve the resonance frequency at 48.85MHz for helium imaging in 1.5T MRI systems. Thus, the non-periodic metausrface has big potential to be used for different nuclei imaging applications, even different-field-strength MRI systems, such as 3T or 7T.

Reference

[1] B. Chance *et al.*, “Multiple controls of oxidative metabolism in living tissues as studied by phosphorus magnetic resonance,” *Proc. Natl. Acad. Sci. U. S. A.*, vol. 83, no. 24, pp. 9458–9462, 1986, doi: 10.1073/pnas.83.24.9458.

[2] G. J. Kemp, R. E. Ahmad, K. Nicolay, and J. J. Prompers, “Quantification of skeletal muscle mitochondrial function by P magnetic resonance spectroscopy techniques : a quantitative review,” pp. 107–144, 2015, doi: 10.1111/apha.12307.

[3] J. S. Leigh, “Noninvasive , nondestructive approaches to cell bioenergetics,” vol. 77, no. 12, pp. 7430–7434, 1980.

[4] R. G. Shuuman and G. I. Shulman, “Quantitation of Hepatic Glycogenolysis and Gluconeogenesis in Fasting Humans with 13C NMR,” vol. 1, no. October, 1991.

[5] R. Gruetter, G. Adriany, I. Choi, P. Henry, and H. Lei, “Localized in vivo C NMR spectroscopy of the brain,” pp. 313–338, 2003, doi: 10.1002/nbm.841.

[6] T. Q. Duong, J. J. H. Ackerman, H. S. Ying, and J. J. Neil, “Evaluation of Extra- and Intracellular Apparent Diffusion in Normal and Globally Ischemic Rat Brain via 19F NMR,” 1998.

[7] M. S. Hussain *et al.*, “Sodium Imaging Intensity Increases with Time after Human Ischemic Stroke,” pp. 55–62, 2009, doi: 10.1002/ana.21648.

[8] G. Madelin and R. R. Regatte, “Biomedical Applications of Sodium MRI In Vivo,” vol. 529, pp. 511–529, 2013, doi: 10.1002/jmri.24168.

[9] A. Hurshkainen *et al.*, "A Novel Metamaterial-Inspired RF-coil for Preclinical Dual-Nuclei MRI," *Sci. Rep.*, vol. 8, no. 1, pp. 1–13, 2018, doi: 10.1038/s41598-018-27327-y.

[10] R. Warner and S. Pittard, "Magnets," in *New Developments in NMR*, 2016.

[11] A. Webb, *Introduction to biomedical imaging*. 2002.

[12] C. Tang, M. A. Brown, and R. C. Semelka, "MRI: Basic Principles and Applications," *Radiat. Res.*, 1996, doi: 10.2307/3579182.

[13] L. P. Panych and B. Madore, "The physics of MRI safety," *Journal of Magnetic Resonance Imaging*. 2018, doi: 10.1002/jmri.25761.

[14] G. Morrow, "Progress in MRI magnets," *IEEE Trans. Appl. Supercond.*, 2000, doi: 10.1109/77.828339.

[15] T. Nakamura *et al.*, "Development of a superconducting bulk magnet for NMR and MRI," *J. Magn. Reson.*, 2015, doi: 10.1016/j.jmr.2015.07.012.

[16] J. F. Schenck, "Safety of strong, static magnetic fields," *Journal of Magnetic Resonance Imaging*. 2000, doi: 10.1002/1522-2586(200007)12:1<2::AID-JMRI2>3.0.CO;2-V.

[17] W. S. Price, "Spin dynamics: Basics of nuclear magnetic resonance, 2nd edition.," *Concepts Magn. Reson. Part A*, 2009, doi: 10.1002/cmr.a.20130.

[18] D. W. McRobbie, E. A. Moore, and M. J. Graves, *MRI from picture to proton*. 2017.

[19] B. Gruber, M. Froeling, T. Leiner, and D. W. J. Klomp, "RF coils: A practical guide for nonphysicists," *Journal of Magnetic Resonance Imaging*. 2018, doi: 10.1002/jmri.26187.

[20] J. T. Vaughan and J. R. Griffiths, *RF Coils for MRI*. 2012.

[21] M. Tincher, C. R. Meyer, R. Gupta, and D. M. Williams, "Polynomial modeling and reduction of rf body coil spatial inhomogeneity in mri," *IEEE Trans. Med. Imaging*, 1993, doi: 10.1109/42.232267.

[22] N. De Zanche, "Birdcage Volume Coil Design," in *Encyclopedia of Magnetic Resonance*, 2011.

[23] M. Vossen, W. Teeuwisse, M. Reijnierse, C. M. Collins, N. B. Smith, and A.

G. Webb, “A radiofrequency coil configuration for imaging the human vertebral column at 7 T,” *J. Magn. Reson.*, 2011, doi: 10.1016/j.jmr.2010.11.004.

[24] F. Bloch, “Nuclear induction,” *Physica*, 1951, doi: 10.1016/0031-8914(51)90068-7.

[25] E. M. Purcell, H. C. Torrey, and R. V. Pound, “Resonance absorption by nuclear magnetic moments in a solid [7],” *Physical Review*. 1946, doi: 10.1103/PhysRev.69.37.

[26] A. E. Bohte, J. R. Van Werven, S. Bipat, and J. Stoker, “The diagnostic accuracy of US, CT, MRI and 1H-MRS for the evaluation of hepatic steatosis compared with liver biopsy: A meta-analysis,” *Eur. Radiol.*, 2011, doi: 10.1007/s00330-010-1905-5.

[27] C. Westbrook, C. K. Roth, and J. Talbot, *MRI in Practice 4th*. 2011.

[28] M. Decorps, “Basic principles of NMR-imaging,” *Phys. Medica*, 1996, doi: 10.1007/978-94-009-3537-2_35.

[29] M. Jones, “Magnetic Resonance Imaging: Principles and Applications,” *Radiology*, 1987, doi: 10.1148/radiology.162.1.72.

[30] J. P. Marques, F. F. J. Simonis, and A. G. Webb, “Low-field MRI: An MR physics perspective,” *Journal of Magnetic Resonance Imaging*. 2019, doi: 10.1002/jmri.26637.

[31] W. Fong, “ Handbook of MRI Pulse Sequences ,” *Med. Phys.*, 2005, doi: 10.1118/1.1904597.

[32] J. A. A. K. K. O. M. A. L. M. I. V. U. O and R. O. B. E. R. T. P. L. O. N. S. E. Y, “Lead ECG System,” in *Bioelectromagnetism*, 1995.

[33] N. Boulant, “T1 and T2 effects during radio-frequency pulses in spoiled gradient echo sequences,” *J. Magn. Reson.*, 2009, doi: 10.1016/j.jmr.2008.12.023.

[34] L. De Rochefort, X. Maître, J. Bittoun, and E. Durand, “Velocity-selective RF pulses in MRI,” *Magn. Reson. Med.*, 2006, doi: 10.1002/mrm.20751.

[35] G. Mayer, “Resolution Enhancement in Magnetic Resonance Imaging by

Frequency Extrapolation," *Solutions*, 2008, [Online]. Available: http://scholar.google.com/scholar?hl=en&btnG=Search&q=intitle:Resolution+Enhancement+in+Magnetic+Resonance+Imaging+by+Frequency+Extrapolation+by#0.

[36] E. Carmi, S. Liu, N. Alon, A. Fiat, and D. Fiat, "Resolution enhancement in MRI," *Magn. Reson. Imaging*, 2006, doi: 10.1016/j.mri.2005.09.011.

[37] D. B. Plewes and W. Kucharczyk, "Physics of MRI: A primer," *Journal of Magnetic Resonance Imaging*. 2012, doi: 10.1002/jmri.23642.

[38] R. J. Gillies, N. Raghunand, G. S. Karczmar, and Z. M. Bhujwalla, "MRI of the tumor microenvironment," *Journal of Magnetic Resonance Imaging*. 2002, doi: 10.1002/jmri.10181.

[39] P. M. Parizel, S. Makkat, E. Van Miert, J. W. Van Goethem, L. Van den Hauwe, and A. M. De Schepper, "Intracranial hemorrhage: Principles of CT and MRI interpretation," *Eur. Radiol.*, 2001, doi: 10.1007/s003300000800.

[40] P. B. Roemer, W. A. Edelstein, C. E. Hayes, S. P. Souza, and O. M. Mueller, "The NMR phased array," *Magn. Reson. Med.*, 1990, doi: 10.1002/mrm.1910160203.

[41] D. I. Hoult, "The principle of reciprocity in signal strength calculations?A mathematical guide," *Concepts Magn. Reson.*, vol. 12, no. 4, pp. 173–187, 2000, doi: 10.1002/1099-0534(2000)12:4<173::AID-CMR1>3.0.CO;2-Q.

[42] M. V. Vaidya, C. M. Collins, D. K. Sodickson, R. Brown, G. C. Wiggins, and R. Lattanzi, "Dependence of B1- and B1+ field patterns of surface coils on the electrical properties of the sample and the MR operating frequency," *Concepts Magn. Reson. Part B Magn. Reson. Eng.*, 2016, doi: 10.1002/cmr.b.21319.

[43] Z. Wang, J. C. Lin, W. Mao, W. Liu, M. B. Smith, and C. M. Collins, "SAR and temperature: Simulations and comparison to regulatory limits for MRI," *J. Magn. Reson. Imaging*, 2007, doi: 10.1002/jmri.20977.

[44] J. M. Algarin, M. A. Lopez, M. J. Freire, and R. Marques, "Signal-to-noise ratio evaluation in resonant ring metamaterial lenses for MRI applications," *New J. Phys.*, 2011, doi: 10.1088/1367-2630/13/11/115006.

[45] D. M. Peterson, "Impedance Matching and Baluns," in *Encyclopedia of Magnetic Resonance*, 2011.

[46] C. L. Holloway, E. F. Kuester, J. A. Gordon, J. O'Hara, J. Booth, and D. R. Smith, "An overview of the theory and applications of metasurfaces: The two-dimensional equivalents of metamaterials," *IEEE Antennas Propag. Mag.*, 2012, doi: 10.1109/MAP.2012.6230714.

[47] D. S. Wang, S. W. Qu, and C. H. Chan, "Frequency selective surfaces," in *Handbook of Antenna Technologies*, 2016.

[48] R. Panwar and J. R. Lee, "Progress in frequency selective surface-based smart electromagnetic structures: A critical review," *Aerospace Science and Technology*. 2017, doi: 10.1016/j.ast.2017.03.006.

[49] R. S. Anwar, L. Mao, and H. Ning, "Frequency selective surfaces: A review," *Applied Sciences (Switzerland)*. 2018, doi: 10.3390/app8091689.

[50] N. Engheta and R. W. Ziolkowski, *Metamaterials: Physics and Engineering Explorations*. 2006.

[51] D. R. Smith, W. J. Padilla, D. C. Vier, S. C. Nemat-Nasser, and S. Schultz, "Composite medium with simultaneously negative permeability and permittivity," *Phys. Rev. Lett.*, 2000, doi: 10.1103/PhysRevLett.84.4184.

[52] J. B. Pendry, "Negative refraction makes a perfect lens," *Phys. Rev. Lett.*, 2000, doi: 10.1103/PhysRevLett.85.3966.

[53] R. Marqués, F. Martín, and M. Sorolla, *Metamaterials with Negative Parameters: Theory, Design, and Microwave Applications*. 2007.

[54] S. B. Yeap, X. Qing, and Z. N. Chen, "Metamaterial magneto inductive lens for magnetic resonance imaging," *2016 Int. Work. Antenna Technol. iWAT 2016*, pp. 138–141, 2016, doi: 10.1109/IWAT.2016.7434824.

[55] M. J. Freire, L. Jelinek, R. Marques, and M. Lapine, "On the applications of μr = - 1 metamaterial lenses for magnetic resonance imaging," *Journal of Magnetic Resonance*, vol. 203, no. 1. pp. 81–90, 2010, doi: 10.1016/j.jmr.2009.12.005.

[56] M. J. Freire, R. Marques, and L. Jelinek, "Experimental demonstration of a = 1

metamaterial lens for magnetic resonance imaging Experimental demonstration of a = − 1 metamaterial lens for magnetic," vol. 231108, no. 2008, pp. 2006–2009, 2011, doi: 10.1063/1.3043725.

[57] J. M. Algarin, F. Breuer, V. C. Behr, and M. J. Freire, "Analysis of the noise correlation in MRI coil arrays loaded with metamaterial magnetoinductive lenses," *IEEE Trans. Med. Imaging*, vol. 34, no. 5, pp. 1148–1154, 2015, doi: 10.1109/TMI.2014.2377792.

[58] C. D. Constantinides, E. Atalar, and E. McVeigh, "Signal-to-noise measurements in magnitude images from NMR phased arrays," *Annu. Int. Conf. IEEE Eng. Med. Biol. - Proc.*, vol. 1, no. C, pp. 456–459, 1997, doi: 10.1109/iembs.1997.754578.

[59] M. J. Freire, M. A. Lopez, J. M. Algarin, F. Breuer, and R. Marqués, "Image acceleration in parallel magnetic resonance imaging by means of metamaterial magnetoinductive lenses," *AIP Adv.*, vol. 2, no. 2, 2012, doi: 10.1063/1.4723675.

[60] M. C. K. Wiltshire, J. B. Pendry, I. R. Young, D. J. Larkman, D. J. Gilderdale, and J. V. Hajnal, "Microstructured magnetic materials for rf flux guides in magnetic resonance imaging," *Science (80-.).*, vol. 291, no. 5505, pp. 849–851, 2001, doi: 10.1126/science.291.5505.849.

[61] J. B. Pendry, "Negative refraction makes a perfect lens," *Phys. Rev. Lett.*, vol. 85, no. 18, pp. 3966–3969, 2000, doi: 10.1103/PhysRevLett.85.3966.

[62] M. Wiltshire, J. Hajnal, J. Pendry, D. Edwards, and C. Stevens, "Metamaterial endoscope for magnetic field transfer: near field imaging with magnetic wires," *Opt. Express*, vol. 11, no. 7, p. 709, 2003, doi: 10.1364/oe.11.000709.

[63] X. Radu, A. Lapeyronnie, and C. Craeye, "Numerical and experimental analysis and demonstration of a wire medium collimator for MRI," p. 2, 2010.

[64] D. F. Sievenpiper, L. Zhang, R. Broas, and E. Yablonovitch, "High-impedance electromagnetic surfaces with forbidden bands at radio and microwave frequencies," *Terahertz and Gigahertz Photonics*, vol. 3795, no. 11, p. 154, 1999, doi: 10.1117/12.370159.

[65] A. Vallecchi, J. R. De Luis, F. Capolino, and F. De Flaviis, “Low profile fully planar folded dipole antenna on a high impedance surface,” *IEEE Trans. Antennas Propag.*, 2012, doi: 10.1109/TAP.2011.2167912.

[66] I. Issa, K. L. Ford, M. Rao, and J. Wild, “Evaluation of High Impedance Surfaces for MRI RF coil applications - Simulations of RF field and Specific Absorption Rate,” *2016 10th Eur. Conf. Antennas Propagation, EuCAP 2016*, pp. 2–4, 2016, doi: 10.1109/EuCAP.2016.7481761.

[67] I. Issa, K. L. Ford, M. Rao, and J. Wild, “Enhancement of radio frequency magnetic field for a 1 . 5 T magnetic resonance system using a high impedance surface,” vol. 10, no. Lapc 2015, pp. 2–7, 2016, doi: 10.1049/iet-map.2016.0088.

[68] F. Yang and Y. Rahmat-Samii, *Electromagnetic band gap structures in antenna engineering*. 2008.

[69] G. Saleh, K. Solbach, and A. Rennings, “EBG structure to improve the B1 efficiency of stripline coil for 7 Tesla MRI,” *Proc. 6th Eur. Conf. Antennas Propagation, EuCAP 2012*, no. October 2016, pp. 1399–1401, 2012, doi: 10.1109/EuCAP.2012.6206267.

[70] T. A. Derzhavskaya, S. B. Glybovski, I. V. Melchakova, A. J. E. Raaijmakers, and C. A. T. Van Den Berg, “Electromagnetic bandgap metasurfaces for decoupling of elements of MRI body coil array at 7 Tesla,” *Proc. Int. Conf. Days Diffr. 2015, DD 2015*, pp. 75–80, 2015, doi: 10.1109/DD.2015.7354836.

[71] W. M. Brink, J. S. Van Den Brink, and A. G. Webb, “The effect of high-permittivity pads on specific absorption rate in radiofrequency-shimmed dual-transmit cardiovascular magnetic resonance at 3T,” *J. Cardiovasc. Magn. Reson.*, vol. 17, no. 1, pp. 1–8, 2015, doi: 10.1186/s12968-015-0188-z.

[72] Loctite *et al.*, “Dielectric Materials Chart — Eccostock,” *Tech. Reports AFML-TR-72-39 74-250*, vol. 6, no. 2, pp. 633–641, 2010, doi: 10.1002/mrm.22695.Reducing.

[73] W. M. Brink and A. G. Webb, “High permittivity pads reduce specific absorption rate, improve B 1 homogeneity, and increase contrast-to-noise ratio

for functional cardiac MRI at 3 T," *Magn. Reson. Med.*, vol. 71, no. 4, pp. 1632–1640, 2014, doi: 10.1002/mrm.24778.

[74] 2017 Shahul S,Tung A, Minhaj M, Nizamuddin J, Wenger J, Mahmood E, Mueller A,Shaefi S, Scavone B, Kociol R D, Talmor D, Rana S, "乳鼠心肌提取 HHS Public Access," *Physiol. Behav.*, vol. 176, no. 10, pp. 139–148, 2017, doi: 10.1016/j.physbeh.2017.03.040.

[75] A. P. Slobozhanyuk *et al.*, "Enhancement of Magnetic Resonance Imaging with Metasurfaces," *Adv. Mater.*, vol. 28, no. 9, pp. 1832–1838, 2016, doi: 10.1002/adma.201504270.

[76] A. V. Shchelokova *et al.*, "Tunable hybrid metasurfaces for MRI applications," *AIP Conf. Proc.*, vol. 1874, no. September, pp. 12–14, 2017, doi: 10.1063/1.4998062.

[77] R. Schmidt, A. Slobozhanyuk, P. Belov, and A. Webb, "Flexible and compact hybrid metasurfaces for enhanced ultra high field in vivo magnetic resonance imaging," *Sci. Rep.*, vol. 7, no. 1, pp. 1497–1498, 2017, doi: 10.1038/s41598-017-01932-9.

[78] R. Schmidt and A. Webb, "Improvements in RF shimming in high field MRI using high permittivity materials with low order pre-fractal geometries," *IEEE Trans. Med. Imaging*, vol. 35, no. 8, pp. 1837–1844, 2016, doi: 10.1109/TMI.2016.2531120.

[79] W. M. Brink, R. F. Remis, and A. G. Webb, "A theoretical approach based on electromagnetic scattering for analysing dielectric shimming in high-field MRI," *Magn. Reson. Med.*, vol. 75, no. 5, pp. 2185–2194, 2016, doi: 10.1002/mrm.25783.

[80] Q. X. Yang *et al.*, "RF Field Enhancement with High Dielectric Constant (HDC) Pads in a Receive Array Coil at 3.0 T," *J. Magn. Reson. Imaging*, vol. 38, no. 2, pp. 435–440, 2013, doi: 10.1002/jmri.23988.RF.

[81] B. Y. Lee, X. H. Zhu, S. Rupprecht, M. T. Lanagan, Q. X. Yang, and W. Chen, "Large improvement of RF transmission efficiency and reception sensitivity for

human in vivo 31P MRS imaging using ultrahigh dielectric constant materials at 7 T," *Magn. Reson. Imaging*, vol. 42, pp. 158–163, 2017, doi: 10.1016/j.mri.2017.07.019.

[82] L. Hu *et al.*, "A Generalized Strategy for Designing 19 F / 1 H Dual-Frequency MRI Coil for Small Animal Imaging at 4 . 7 Tesla," vol. 252, pp. 245–252, 2011, doi: 10.1002/jmri.22516.

[83] M. Alecci, S. Romanzetti, J. Kaffanke, A. Celik, H. P. Wegener, and N. J. Shah, "Practical design of a 4 Tesla double-tuned RF surface coil for interleaved 1H and 23Na MRI of rat brain," *J. Magn. Reson.*, vol. 181, no. 2, pp. 203–211, 2006, doi: 10.1016/j.jmr.2006.04.011.

[84] A. Maunder, M. Rao, F. Robb, and J. M. Wild, "Comparison of MEMS switches and PIN diodes for switched dual tuned RF coils," *Magn. Reson. Med.*, vol. 80, no. 4, pp. 1746–1753, 2018, doi: 10.1002/mrm.27156.

[85] D. Mri *et al.*, "A Novel Metamaterial-Inspired RF-coil for Preclinical," pp. 1–12, 2017.

[86] M. J. Freire, R. Marques, and L. Jelinek, "Experimental demonstration of a μ = -1 metamaterial lens for magnetic resonance imaging," no. Mm.

[87] F. Costa, A. Monorchio, and G. Manara, "An Overview of Equivalent Circuit Modeling Techniques of Frequency Selective Surfaces and Metasurfaces," no. December, 2014.

[88] I. Issa, K. L. Ford, M. Rao, and J. M. Wild, "A Magnetic Resonance Imaging Surface Coil Transceiver Employing a Metasurface for 1.5T Applications," *IEEE Trans. Med. Imaging*, vol. 39, no. 4, pp. 1085–1093, 2019, doi: 10.1109/tmi.2019.2942194.

[89] Z. Chen, K. Solbach, D. Erni, and A. Rennings, "Electromagnetic Field Analysis of a Dipole Coil Element with Surface Impedance Characterized Shielding Plate for 7-T MRI," *IEEE Trans. Microw. Theory Tech.*, vol. 64, no. 3, pp. 972–981, 2016, doi: 10.1109/TMTT.2016.2518168.

[90] Q. X. Yang, J. Wang, J. Wang, C. M. Collins, C. Wang, and M. B. Smith, "Reducing SAR and enhancing cerebral signal-to-noise ratio with high

permittivity padding at 3 T," *Magn. Reson. Med.*, 2011, doi: 10.1002/mrm.22695.

[91] J. M. Algarín, M. J. Freire, F. Breuer, and V. C. Behr, "Metamaterial magnetoinductive lens performance as a function of field strength," *J. Magn. Reson.*, 2014, doi: 10.1016/j.jmr.2014.08.006.

[92] Q. X. Yang *et al.*, "Manipulation of image intensity distribution at 7.0 T: Passive RF shimming and focusing with dielectric materials," *J. Magn. Reson. Imaging*, vol. 24, no. 1, pp. 197–202, 2006, doi: 10.1002/jmri.20603.